



City Research Online

City St George's, University of London

Citation: Qian, K., Geng, S., Liang, S., Fu, F. & Yu, J. (2022). Effects of loading regimes on the structural behavior of RC beam-column subassemblages against disproportionate collapse. *Engineering Structures*, 251(A), 113470. doi: 10.1016/j.engstruct.2021.113470

This is the accepted version of the paper.

This version of the publication may differ from the final published version. To cite this item please consult the publisher's version.

Permanent repository link: <https://openaccess.city.ac.uk/id/eprint/26942/>

Link to published version: <https://doi.org/10.1016/j.engstruct.2021.113470>

Copyright and Reuse: Copyright and Moral Rights remain with the author(s) and/or copyright holders. Copies of full items can be used for personal research or study, educational, or not-for-profit purposes without prior permission or charge, unless otherwise indicated, provided that the authors, title and full bibliographic details are credited, a hyperlink and/or URL is given for the original metadata page and the content is not changed in any way. For full details of reuse please refer to [City Research Online policy](#).

Effects of loading regimes on the structural behavior of RC beam-column sub-assemblages against disproportionate collapse

Kai Qian¹, Song-Yuan Geng¹, Shi-Lin Liang², Feng Fu³, and Jun Yu^{2*}

¹GuangXi Key Laboratory of New Energy and Building Energy Saving, Guilin University of Technology, Guilin, China, 541004.

² College of Civil and Transportation Engineering, Hohai University, Nanjing, China, 210098.

³ School of Mathematics, Computer Science and Engineering, City, University of London, U.K.

Abstract:

The majority of previous quasi-static tests on disproportionate collapse simulated the column removal through applying concentrated load/displacement on the top of the removed column until failure. However, uniformly distributed service load always exists on the frames. Therefore, to reflect the actual load condition more accurately, uniformly distributed load should be applied along the beams first. Then, the temporary support is gradually removed to simulate the process of column removal. By this way, the beams may undergo only a small deflection as the dynamic effect is neglected. Thus, a subsequent concentrated loading process is employed to evaluate the behavior of the beams at the ultimate stage, which may be reached if the dynamic effect is considered. Such a loading process is named sequential loading regime. To evaluate the effects of loading regimes on the behavior of reinforced concrete (RC) frames under a middle column removal scenario, two series of half-scale RC beam-column sub-assemblages were tested in this study. It is found that the conventional concentrated loading regime could accurately estimate the yield strength and the compressive arch action capacity of the RC beam-column sub-assemblages, but it may over-estimate the catenary action (CA) capacity and the deformation capacity. Moreover, although the concentrated loading regime is convenient and able to demonstrate the load transfer mechanisms of the sub-assemblages against disproportionate collapse, it may mistakenly identify the locations of critical sections. Furthermore, based on the failure

* Corresponding author. E-mail address: yujun@hhu.edu.cn

26 modes and local strain gauge results, analytical models were proposed for predicting the CA capacity
27 of the tested specimens under two loading regimes. Results suggest that the analytical models could
1
28 predict the CA capacity well.

3
4
5
29 **Keywords:** Loading regimes; Disproportionate collapse; Reinforced concrete; Load transfer
6
7
30 mechanisms

9
10
11
12
13
14
15
16
17
18
19
20
21
22
23
24
25
26
27
28
29
30
31
32
33
34
35
36
37
38
39
40
41
42
43
44
45
46
47
48
49
50
51
52
53
54
55
56
57
58
59
60
61
62
63
64
65

32 1. Introduction

33 Disproportionate collapse is defined as the spread of an initial local failure from element to
34 element, which eventually results in the collapse of an entire structure or a disproportionately large part
35 of it [1]. After the terrorist attack of Murrah Federal Building in 1995 and Twin Towers of World Trade
36 Center in 2001, disproportionate collapse of buildings due to intentional or accidental events attracted
37 great attention in the structural engineering community. Design guidelines [2-3] were developed for
38 preventing disproportionate collapse, in which indirect and direct design methods were proposed [4-
39 5]. For the indirect method, the capacity of buildings against disproportionate collapse is improved by
40 the implicit requirement of their redundancy, ductility, continuity, and integrity. For example, ACI
41 318-14 [6] requires the continuity of steel reinforcing bars in concrete members. For the direct method,
42 the specific local resistance method and alternate load path method were proposed. Since the specific
43 local resistance method is implemented with an assumed initial threat, such as an accurate estimate of
44 the weight and standoff distance of explosives, it is not commonly used in practical design. Conversely,
45 the alternate load path method is threat-independent and more popular in practice. .

46 The alternate load path method focuses on the ability of the remaining building to redistribute the
47 loads after the removal of one or several vertical elements (columns or walls). Several in-situ tests [7-
48 8] were conducted to investigate the structural behavior against disproportionate collapse. Specifically,
49 Sasani et al. [7] carried out an in-situ dynamic test on a 10-story RC frame before dismantling. The
50 target column was explosively removed, but it was not completely destroyed. As a result, only elastic
51 response of the frame was recorded. Similarly, Sheffield et al. [8] conducted in-situ dynamic tests on
52 a full-scale four-story RC frame, which was loaded with fixed concrete blocks on the floor to represent
53 the specified dead and live load and then tested by explosively removing a column in sequence. The
54 peak displacement of 236 mm (0.03 rad) was measured after suddenly removing an exterior column,
55 and the residual displacement of 968 mm (0.11 rad) was recorded after removing another adjacent
56 interior column. The afore-mentioned in-situ dynamic tests indicated that the structural members in
57 upper floors above the removed column could work together to redistribute the axial load, which was
58 initially resisted by the removed column. The simple analysis suggested that each story just needed to

59 redistribute the vertical load from its own story, provided that beams and slabs in each story had similar
60 geometrical and material properties as well as reinforcement detailing. Accordingly, single-floor
61 substructures can be equivalently used to study the behavior of multi-story frames.

62 Compared with quasi-static tests, dynamic tests are more complex and the result of a single
63 dynamic test is unable to evaluate the load-carrying capacity of a specimen. Thus, quasi-static tests are
64 preferred. However, it must be answered whether quasi-static tests can be equivalently used to
65 investigate the behavior of the frames to resist disproportionate collapse.

66 Fig.1 shows loading regimes for disproportionate collapse studies. As shown in Fig. 1(a), the
67 uniformly distributed load is applied along the beams first in a dynamic test. Then, the temporary
68 support is quickly knocked down to simulate sudden column removal. Although this method can mimic
69 the actual loading scenario, only a few studies [9-12] adopted this loading regime because such a
70 dynamic test is not convenient to demonstrate the structural behavior of the specimen against
71 disproportionate collapse from small to large deformation. In comparison, the concentrated loading
72 (CL) regime is more popular in experimental and numerical studies [13-39]. As shown in Fig. 1(b), in
73 the CL regime, the column is removed first, and then a concentrated load is applied on the top of the
74 removed column. The CL method is able to demonstrate the structural behavior of the specimen against
75 disproportionate collapse, but it ignores the effect of the uniformly distributed service load on the
76 buildings. Thus, the failure mode may be mistakenly identified. To overcome such defects of the CL
77 regime, sequential loading (SL) regime was proposed [40]. As shown in Fig. 1(c), in the SL regime,
78 the uniformly distributed load is applied along the beams first, and then the temporary support is
79 gradually removed to simulate the process of column removal in a quasi-static way. If the specimen
80 can achieve a new balance after the complete removal of the support, a subsequent CL is employed to
81 evaluate the ultimate behavior of the specimen. Although the SL regime has an inherent defect, it has
82 advantages over the commonly used CL regime because it is closer to the actual loading scenario.

83 As test results are affected by the adopted loading regime, and thus, in this paper it is endeavored
84 to evaluate the effects of loading regimes on the structural behavior of RC frames against

85 disproportionate collapse. Accordingly, a quasi-static experimental program was conducted on two
86 series of specimens, each of which were tested under CL or SL regimes, respectively.

1 37 **2. Experimental program**

3 4 5 88 2.1. Test specimens

6
7
8 89 Two series of half-scale beam-column sub-assemblages were tested under CL or SL regime,
9
10 90 respectively. Each series had three specimens with identical sectional dimensions and reinforcing
11
12 91 details but different span-to-depth ratios. For example, CL/SL-13, CL/SL-11, and CL/SL-8 denote the
13
14
15 92 specimens in CL- and SL-series and the span-to-depth ratio of 13, 11, and 8, respectively.

16
17 93 The specimens were extracted from a prototype building, which was an eight-story frame and
18
19
20 94 non-seismically designed in accordance with ACI 314-14 [6]. The span lengths of the prototype
21
22 95 building in longitudinal and transverse directions were both 7,000 mm. The designed dead load (DL)
23
24
25 96 and live load (LL) were 3.0 kPa and 2.5 kPa, respectively. As shown in Fig. 2, each specimen consisted
26
27 97 of a double-span beam, a middle column stub, and two side columns. The size of the half-scale beams
28
29
30 98 and middle column was 250 mm ×150 mm and 250 mm×250 mm, respectively. As suggested by
31
32
33 99 previous studies [14, 18], the side columns were enlarged to 400 mm ×400 mm for applying fixed
34
35 100 boundary conditions. The reinforcement detailing of the beams and columns is shown in Fig. 2(d).
36
37
38 101 Curtailment of beam longitudinal reinforcement complied with non-seismical design and detailing.
39
40 102 T12 and R6 were used for beam longitudinal and transverse rebars, respectively. T16 was utilized for
41
42 103 column longitudinal reinforcement. Note that T16 and T12 represented deformed rebars with a
43
44 104 diameter of 16 mm and 12 mm, respectively, while R6 represented plain rebars with a diameter of 6
45
46
47 105 mm.

48
49 106 Six specimens were cast with the same batch of concrete, of which the designated compressive
50
51
52 107 strength was all 30 MPa. On the day of the test, the measured concrete cylinder compressive strength
53
54 108 of CL-13, SL-13, CL-11, SL-11, CL-8, and SL-8 was 30.5, 30.1, 31.1, 32.5, 31.7, and 31.9 MPa,
55
56 109 respectively. Table 2 lists the properties of rebar.

110 2.2 Loading regimes and instrumentation

111 The test setup for the CL regime is shown in Fig. 3. Similar to Yu and Tan's work [17], the
112 enlarged side columns were supported by two horizontal pin-pin restraints and a bottom pin support.
113 To ensure statically-determinate of the test setup, a series of rollers were installed beneath the bottom
114 pin support to release horizontal constraints from the ground. During the test, the middle column
115 supported onto the ground was removed first. Then, a hydraulic jack installed above the removed
116 column was used for loading with displacement control at the rate of 0.5 mm/s. Moreover, a specially
117 fabricated steel assembly was placed below the hydraulic jack to prevent out-of-plane failure of the
118 sub-assemblages.

119 As shown in Fig. 3(b), to measure the horizontal reaction forces and bending moments, a
120 tension/compression load cell was installed in each horizontal pin-pin restraint. For monitoring the
121 vertical load redistribution, a load cell was installed beneath each pin support and above the upper
122 hydraulic jack. Seven linear variable displacement transducers (LVDTs) were installed along the
123 beams to record the deformation shape of the beams. Two LVDTs were installed to measure the lateral
124 movement of the side columns and to evaluate the stiffness of horizontal constraints at the side
125 columns. The data logger used in the current study was DH 3816N. The sampling frequency was 5 Hz.
126 All the measurement instruments were produced by Jiangsu Donghua Testing Technology Company.

127 As shown in Fig. 4, the test setup for the SL regime was almost the same as that of the CL regime
128 except loading approach. In the SL regime, a hydraulic jack was installed beneath the middle column
129 stub to simulate the ground middle column. After that, six steel weights with a total weight of 6,000
130 kg were hung below the beams. The amount of the steel weight was determined in accordance with the
131 loading requirement of DoD [3], i.e., $1.2DL+0.5LL$ for the specimen with a clear span of 3250 mm
132 (SL-13). Theoretically, the axial force in the removed column of SL-13 was 29.4 kN (6000
133 $\text{kg} \times 1/2 \times 0.0098 \text{ kN/kg} = 29.4 \text{ kN}$). However, the measured axial load was only 23.5 kN due to the gaps
134 in the lower jack. To make the measured axial load as close as possible to the theoretical one, the
135 amount of each steel weight was adjusted through trial and error. Eventually, the steel weights near the
136 middle column were determined to be 1200 kg, while the others were 900 kg. To facilitate comparing

137 results, the specimens with a clear span of 2750 mm (SL-11) and 2000 mm (SL-8) were also tested
138 with an initial hanging weight of 6000 kg. After applying the weights, the stroke of the bottom jack
139 began to retract gradually to simulate removing the ground middle column. If the specimens failed to
140 collapse when the initial axial force in the bottom jack dropped to zero, a concentrated load was applied
141 with the upper jack to demonstrate the ultimate behavior of the specimens. Besides the layout of the
142 instrumentation for CL-series specimens, a load cell was installed beneath the bottom jack to measure
143 its axial reaction for SL-series specimens.

144 3. Test results

145 3.1. Global response

146 CL-13 & SL-13: The key test results are listed in Table 3. Fig. 5 and Fig. 6 illustrate the load-
147 displacement curves and the crack pattern development of the specimens, respectively. The first crack
148 of CL-13 was observed at the beam ends near the middle column (BENM) at a middle column
149 displacement (MCD) of 11 mm. Increasing the MCD to 45 mm, the longitudinal reinforcement at
150 BENM yielded, corresponding to the yield strength (YS) of 33 kN. Based on structural analysis, the
151 nominal YS of CL-13 is 30 kN, which is about 90 % of the test one. Further increasing the MCD to
152 108 mm, the first peak strength (FPS) due to compressive arch action (CAA) was measured to be 43
153 kN. As shown in Fig. 6(a), slight concrete crushing occurred at the compressive zone of the BENM.
154 With increasing the MCD, concrete at the beam end near the side column (BENS) was crushed. The
155 load resistance kept decreasing until the MCD of 300 mm, which was about 0.09 times the clear span
156 length of the beam. After that, the structural resistance re-ascended. At a MCD of 476 mm, the first
157 rebar fracture occurred at the BENM, resulting in a sudden drop of structural resistance. However, the
158 load resistance still kept increasing after the fracture of several rebars in the BENM. When the MCD
159 arrived at 731 mm, the test was stopped as the stroke capacity of the jack was reached. The ultimate
160 strength (US) attributed to the mobilization of catenary action (CA) was 81+ kN. Fig. 7 shows the
161 failure mode of CL-13. It is seen that the bottom rebars at BENM were fractured while the top rebars

162 at BENS were still intact. Cracks penetrating through the beam sections were parallelly distributed
163 along the beams, indicating the development of the axial tension at the large deformation stage.

164 For SL-13, as shown in Fig. 5(a), negative axial force was initially measured, which represented
165 the releasing of axial compression of the bottom hydraulic jack. As mentioned in Section 2.2, the steel
166 weight of 6000 kg was hung below the beams before the test for SL-series specimens. Theoretically,
167 the initial axial force of the bottom jack should be -29.4 kN, while the measured one was only -28 kN
168 as the middle column had a vertical movement of 0.6 mm after hanging the weights. When the axial
169 force was reduced to -10 kN, the first crack was observed at the BENS. When the axial force was
170 reduced to 0 kN, i.e., the complete retraction of the bottom jack, the MCD was only 38 mm with no
171 yield of reinforcement. To investigate the US of the specimen, the additional load was applied onto the
172 middle column stub with the upper jack.

173 To simplify the comparison, the starting point of the load-displacement curve of SL-13 was shifted
174 from (0.6, -28) to the origin (0, 0) of the coordinate system, as shown in Fig. 5(a). Accordingly, the
175 values presented for SL-series specimens were based on the shifted curve. For SL-13, the YS of 31 kN
176 was measured at a MCD of 43 mm, close to the one of CL-13. However, the first yield of SL-13 and
177 CL-13 occurred at the longitudinal reinforcement of the BENS and the BENM, respectively. The FPS
178 of SL-13 was 39 kN, about 91% of that of CL-13. The structural resistance of SL-13 began to re-ascend
179 after a MCD of 330 mm, which was almost the same as CL-13. The first rebar fracture of SL-13
180 occurred at the BENS at a MCD of 551 mm, which was later than that of CL-13. Moreover, the
181 successive fracture of two rebars made the structural resistance of SL-13 drop from 63 kN to 28 kN.
182 SL-13 completely lost its resistance at an ultimate MCD of 629 mm, only 86% of that of CL-13. The
183 US of SL-13 was 63 kN, about 78 % of that of CL-13. Fig. 6(b) and Fig. 8 show the crack pattern
184 development and the failure mode of SL-13, respectively. Different from CL-13, no rebar at the BENM
185 of SL-13 was fractured, and instead, severe concrete crushing and rebar fracture were observed at the
186 BENS. In summary, compared with CL-13, the critical section of SL-13 was changed from the BENM
187 to the BENS due to the initial bending moment induced by the hanging weights.

188 CL-11 & SL-11: Fig. 5(b) compares the load-displacement curves of CL-11 and SL-11. The YS
189 and the FPS of CL-11 were 37 kN and 52 kN, respectively. At a MCD of 288 mm, the load resistance
190 of CL-11 started to re-ascend. The first rebar fracture occurred at the BENM at a MCD of 410 mm,
191 resulting in the sudden drop of load resistance from 52 kN to 33 kN. Then, the load resistance kept
192 increasing and reached a US of 94 kN at a MCD of 712 mm. The YS and FPS of SL-11 were 36 kN
193 and 49 kN, respectively. After reaching the FPS, the load resistance began to decrease due to concrete
194 crushing at the BENS, and re-ascend at a MCD of 281 mm. The load resistance kept increasing until
195 the rebar fracture at the BENS at a MCD of 593 mm, leading to the drop of load resistance from 85 kN
196 to 27 kN. After that, the load resistance slightly increased and the eventual load resistance was 58 kN.
197 Figs. 9 and 10 illustrate the failure mode of CL-11 and SL-11, respectively. Similar to CL-13, rebar
198 fracture occurred at the BENM of CL-11 but with more severe concrete crushing. In comparison, the
199 severe local failure of SL-11 occurred at the BENS.

200 CL-8 & SL-8: Fig. 5(c) compares the load-displacement curves of CL-8 and SL-8. The YS of CL-
201 8 and SL-8 were 53 kN and 54 kN, respectively. The FPS of CL-8 and SL-8 were 77 kN and 74 kN,
202 respectively. Before the first rebar fracture, the load-displacement curves were similar. The first rebar
203 fracture of CL-8 and SL-8 occurred at the BENM and BENS at the MCDs of 330 mm and 357 mm,
204 respectively. Thereafter, CL-8 developed load resistance much faster than SL-8. Eventually, the US of
205 CL-8 and SL-8 was 88 kN and 63 kN, respectively. Fig. 11 shows that severe local damage including
206 rebar fracture and concrete crushing and spalling occurred at one of the BENMs of CL-8. As shown
207 in Fig. 12, for SL-8, the damage of the BENS was more severe than that of the BENM. It was
208 worthwhile to point out that the steel weights touched each other at the large deformation stage due to
209 limited space. As a result, partial gravity of the steel weights at the mid-span was transferred to the
210 BENM, resulting in severe damage in the right-side BENM.

211 3.2. Horizontal reaction forces

212 Fig. 13 compares the horizontal reaction force-displacement curves of CL-series and SL-series
213 specimens. As shown in Fig. 13(a), for CL-13 and SL-13, compressive reaction force was measured

214 initially, indicating the development of CAA in the beams. The maximum compressive reaction forces
215 of -153 kN and -154 kN were measured for CL-13 and SL-13, respectively. Therefore, consistent with
216 the vertical load response, the loading regime had little effect on the development of the CAA. The
217 mobilization of tensile reaction forces corresponded to the CA stage, and the maximum tensile reaction
218 forces of CL-13 and SL-13 were 148 kN and 111 kN, respectively. Similarly, as shown in Figs. 13(b
219 and c), the maximum compressive reaction forces of CL-11, SL-11, CL-8, and SL-8 were -178 kN, -
220 167 kN, -202 kN, and -224 kN, respectively. The maximum tensile reaction forces of CL-11, SL-11,
221 CL-8, and SL-8 were 154 kN, 167 kN, 147 kN, and 110 kN, respectively. In general, the loading regime
222 had little effect on the development of the horizontal reaction forces, but it significantly affected the
223 CA, as shown in Fig. 5.

224 3.3. Beam deflection shape

225 Fig. 14 shows the deflection shape of the beams at various stages. Before rebar fracture, the beams
226 deformed in a double-curvature shape. However, as shown in Fig. 14(a), for CL-13, after rebar fracture
227 at the BENM, the single-span beam deformed like a cantilever beam. Thus, the chord rotation, defined
228 as the ratio of the MCD to the beam clear span according to DoD [3], was larger than the local rotation
229 at the BENS. As shown in Fig. 14(b), after rebar fractured at the BENS of SL-13, the deflection shape
230 of the beams was close to that of simply-supported beams. Thus, the chord rotation was smaller than
231 the local rotation at BENS. Similar observations were found in the other specimens.

232 3.4. Strain gauge readings

233 As shown in Fig. 15, the first yield of rebars at the BENS and BENM of CL-13 occurred at the
234 MCDs of 59 mm and 45 mm, respectively. The bottom rebars at the BENS of CL-13 initially suffered
235 compression and transformed to tension after a MCD of 440 mm. Moreover, the bottom rebars at the
236 BENS of CL-13 yielded at the end of the test. Similarly, the top rebars at the BENM of CL-13 was
237 initially in compression and converted to tension at a MCD of 280 mm. At a MCD of 501 mm, the top
238 rebars at the BENM yielded, confirming that the continuous top rebars contributed to the development
239 of CA for CL-series specimens.

240 As shown in Fig. 16, for SL-13, the first yield of the rebars at the BENS and BENM was recorded
241 at the MCDs of 43 mm and 120 mm, respectively. Similar to CL-13, the bottom rebars at the BENS of
242 SL-13 finally developed tension and reached yielding, but the top rebars at the BENM failed to yield.
243 As shown in Figs. 17 to 20, similar results were measured in the other specimens.

244 4. Analysis and discussions

245 4.1. Effects of span-to-depth ratio and loading regimes

246 Because the nature of the loading regime is to simulate the load redistribution process of the axial
247 force of the removed column, the ratio of load resistance to the designed axial force of the removed
248 column can directly reflect the risk of progressive collapse. The ratio is given in the bracket behind the
249 load resistance in this Section. The designed axial forces of the removed column in the specimens with
250 the span-to-depth ratio of 13, 11, and 8 were 29.4 kN, 21.6 kN, and 12.2 kN, respectively. As listed in
251 Table 3, the YS of CL-13, CL-11, CL-8, SL-13, SL-11, and SL-8 was 33 kN (1.12), 37 kN (1.71), 53
252 kN (4.34), 31 kN (1.05), 36 kN (1.67), and 54 kN (4.43), respectively. Thus, decreasing the span-to-
253 depth ratio from 13 to 8 increased the YS of CL/SL-series specimens by 61 % and 71 %, respectively.
254 Moreover, when the span-to-depth ratio was decreased from 13 to 8, the FPS increased by 79 % and
255 90 % for CL/ SL-series specimens, respectively. However, the effects of the span-to-depth ratio on the
256 US of the specimens were not clear. For CL-13, CL-11, and CL-8, the US was 81+ kN (2.76+), 94 kN
257 (4.35), and 88 kN (7.21), respectively. For SL-13, SL-11, and SL-8, the US was 63 kN (2.14), 85 kN
258 (3.94), and 63 kN (5.16), respectively. The CL-series specimens developed greater US than the SL-
259 series specimens. This suggested that the structural capacity due to CA depended on the area of
260 continuous reinforcement and the rotation capacity of beam-column connections. As shown in Figs.
261 16, 18, and 20, the tensile strain of the beam bottom rebars at the BENS was relatively small when the
262 US of SL-series specimens was attained. Thus, the US can be attributed to the CA developed mainly
263 in the beam top rebars at the BENS (3T12). In comparison, the US of CL-series specimens was attained
264 when the beam top rebars at the BENM (3T12) were fractured. Therefore, the area of continuous
265 reinforcement that was mobilized to develop the US was identical for the CL/ SL-series specimens.

266 However, the rotational capacity of CL-13 (0.23 rad), CL-11 (0.26 rad) and CL-8 (0.28 rad) were
267 greater than that of SL-13 (0.17 rad), SL-11 (0.22 rad) and SL-8 (0.18 rad), respectively. As a result,
268 the CL-series specimens could develop greater US than the SL-series specimens. In general, from the
269 perspective of resistance/demand ratio, decreasing the span-to-depth ratio is able to reduce the
270 progressive collapse risk.

271 Experimental results show that the loading regimes have little effect on YS and FPS but have
272 significant effects on the deformation capacity and the US. Based on the failure mode, the CL regime
273 may conclude that the bottom rebars at the BENM fracture first. However, in reality, due to the existing
274 distributed loads, the top rebars at the BENS fracture first. As a result, the analytical model for CA
275 derived based on the CL regime may be inaccurate.

276 4.2. Effects of early rebar fracture on catenary action

277 The mobilization of the CA relies on the tension developed in the beam rebars. Similar to Yu and
278 Tan's discussion [26], as shown in Fig. 21(a), the angle between the tension in the beam and the horizon
279 is chord rotation φ before rebar fracture, whereas the angle changes to β after rebar fracture, as shown
280 in Figs. 21(b) and (c). It is evident that the angle β is smaller than the chord rotation φ for a given
281 displacement. Thus, the rebar fracture not only reduces the area of the beam rebars that can develop
282 tension but also decreases the vertical projection of the tension to resist disproportionate collapse.
283 However, the rebar fracture releases the rotation of the beam section, resulting in a greater rotation
284 capacity of the beam end. The increased rotation capacity allows further development of the CA. Fig.
285 5 demonstrates that the CL-series specimens can develop greater CA capacity at the large deformation
286 stage even if early rebar fracture occurred. In comparison, the SL-series specimens achieved their CA
287 capacity at the first rebar fracture because the area of bottom beam rebars was smaller than that of the
288 top rebars.

290 To more deeply understand the structural behavior of RC beam-column sub-assemblages under
 291 different loading regimes, an analytical investigation is performed to illustrate the load transfer
 292 mechanisms at different beam sections, similar to the work of Yu and Tan [18]. The internal forces
 293 transferred from the selected beam sections to the adjacent beam sections are illustrated in Fig. 22, the
 294 total vertical component of the internal force (P) at the selected beam sections is composed of vertical
 295 components of the shear force (V) and the axial force (N). According to the force equilibrium along
 296 the vertical direction, P transferred from the selected beam sections to the adjacent beam sections are
 297 determined by Eq. (1).

$$P = 2(N \sin \theta + V \cos \theta) \quad (1)$$

298 where θ is the local rotation of the selected beam sections. At the BENM, θ can be approximately
 299 determined as $\theta = \arctan(4(D_l - D_{3l/4})/l)$; $D_{3l/4}$ is the vertical displacement measured at the position
 300 with $3l/4$ from the side column; D_l is the MCD; l is the beam span. At the BENS, θ can be
 301 approximately determined as $\theta = \arctan(4D_{l/4}/l)$, and $D_{l/4}$ is the vertical displacement measured at
 302 the position with $l/4$ from the side column.

303 As illustrated in Fig. 22, based on the force equilibrium along the beam axis and vertical direction,
 304 Eqs. (2) and (3) are obtained as follow

$$N = F_L \sin \theta + (H_t + H_b) \cos \theta \quad (2)$$

$$F_L = V \cos \theta + N \sin \theta \quad (3)$$

305 where F_L is the measured vertical reaction beneath the side column; H_t and H_b are the measured
 306 horizontal reaction force of the top and bottom horizontal pin-pin restraint, respectively.

307 Thus, for CL-series specimens, N and V of the selected sections are calculated by Eqs. (4) and
 308 (5), respectively.

$$N_{CL} = (F_L \tan \theta + H_t + H_b) \cos \theta \quad (4)$$

$$V_{CL} = (F_L - N_{CL} \sin \theta) / \cos \theta \quad (5)$$

Similarly, for SL-series specimens, N and V are calculated by Eqs. (6) and (7), respectively.

$$N_{SL} = ((F_L - G) \tan \theta + H_t + H_b) \cos \theta \quad (6)$$

$$V_{SL} = (F_L - G - N_{SL} \sin \theta) / \cos \theta \quad (7)$$

where G is the gravity load of the hanging weight between the selected section and the side column.

For CL-series specimens, according to the locations of reactions as shown in Fig. 22, the bending moment at BENM (M^M) and BENS (M^S) are calculated by Eqs. (8) and (9), respectively.

$$M_{CL}^M = F_L (l + 0.2) - H_t (D_l + 0.35) + H_b (D_l - 0.35) \quad (8)$$

$$M_{CL}^S = 0.2F_L - 0.35H_t + 0.35H_b \quad (9)$$

Similarly, the M^M and M^S of SL-series specimens are determined by Eqs. (10) and (11), respectively.

$$M_{SL}^M = F_L (l + 0.2) - H_t (D_l + 0.35) + H_b (D_l - 0.35) - 0.75G_{l/4}l - 0.5G_{l/2}l - 0.25G_{3l/4}l \quad (10)$$

$$M_{SL}^S = 0.2F_L - 0.35H_t + 0.35H_b \quad (11)$$

The variations of the transferred vertical load from the selected sections (i.e., BENM and BENS) of the specimens are shown in Figs. 23 to 28, respectively. It is found that the axial force made a negative contribution at the small deformation stage due to the second-order effect, whereas it made a positive contribution at the large deformation stage. As shown in Fig. 23(a), at the BENM of CL-13, the shear force contribution decreased quickly after the CAA stage. As a result, the vertical component

332 of the axial force dominated the vertical load transfer at the large deformation stage. By contrast, at the
333 BENS of CL-13, the vertical projection of the shear force still kept increasing at the large deformation
334 stage since no rebar fractured there, as shown in Fig. 23(b), even though such contribution was smaller
335 than that from the axial force.

336 Fig. 24 shows that the hanging weights induced initial shear force at the selected sections of SL-
337 13. As illustrated in Fig. 24(a), the shear force contribution at the BENM kept almost constant during
338 the loading history until failure. However, as shown in Fig. 24(b), the shear force contribution at the
339 BENS began to decrease with the increase of the vertical displacement at the large deformation stage.
340 Moreover, at the CAA stage, the contribution of both shear and axial force of the BENS was much
341 greater than that of the BENM, indicating that the material strength of the BENS was used more
342 sufficiently than that of BENM. As shown in Figs. 25 to 28, similar results were found for the other
343 specimens. Therefore, loading regimes might draw different conclusions regarding the load transfer
344 mechanisms at different beam ends.

345 Fig. 29 illustrates the variation of bending moment at the beam ends. As shown in Fig. 29(a), the
346 bending moment at the beam ends of CL-13 decreased quickly after the stage of CAA. In comparison,
347 as shown in Fig. 29(b), the decline of bending moment for SL-13 was much milder. This is because
348 the material properties of the beams can be more sufficiently mobilized under the SL. However, as
349 shown in Figs. 29(c-f), such phenomenon became marginal with decreasing the span-to-depth ratio. As
350 illustrated in Fig. 30, the nature of CAA increasing the flexural resistance was the fact that bending
351 moment capacity of the beam sections was enhanced by considerable axial compression developed in
352 the beams through $M-N$ interaction. Moreover, the measured $M-N$ diagram agreed well with the
353 theoretical ones determined by Xtract [41].

354 4.4. Analytical model to evaluate CA capacity

355 Analytical models are proposed herein to evaluate the US of CL-series and SL-series specimens.
356 The US of SL-series specimens is attained at the first fracture of the beam top rebars at BENS. As
357 shown in Figs. 16, 18, and 20, since the strain of beam bottom rebars was relatively small at the fracture

358 of the top rebars, only top rebars were considered to provide the US. Therefore, for SL-series specimens,
359 the US is determined by Eq. (12).

$$360 \quad P_{CA} = 2f_u A_{st} \sin \varphi \quad (12)$$

361 where f_u and A_{st} are the ultimate strength and the area of top rebars, respectively; φ is the chord
362 rotation of the beam, as shown in Fig. 31(a).

363 For CL-series frames, as the bottom rebar at BENM fractured soon after the onset of CA. Thus,
364 similar to SL-series specimens, only beam top rebars were considered to provide the US. However, as
365 the bottom rebar fractured earlier, it is assumed that the direction of tensile force is along the line
366 between the top rebar at BENM and the middle of the section at BENS. As shown in Fig. 31(b), the
367 rotation α is determined as the angle between the action line of the tensile force and the horizontal
368 line. Therefore, the US of CL-series specimens is given by

$$369 \quad P_{CA} = 2f_u A_{st} \sin \alpha \quad (13)$$

370 As shown in Fig. 5, the results from the proposed CA models agreed well with the measured ones.
371 Therefore, the proposed models can be used for evaluating the US of CL/SL-series specimens. It should
372 be noted that practical design will benefit from an allowed rotation of the beams to develop CA.
373 However, the deformation capacity of the beams can not be determined in this study due to the limited
374 number of specimens. As the rotation capacity is affected by material properties of concrete and steel
375 reinforcement, geometric properties of beam sections and reinforcement detailing, etc., more tests
376 should be conducted to fill this gap. Although the proposed models can not be used for design directly,
377 the methods are reasonable to predict CA capacity with given rotations of the beams and the area of
378 contributing rebars. Thus, the methodology herein can be implemented for design with further study,
379 in particular, quantifying the allowed rotation capacity of the beam segments.

380 5. Conclusions

381 Based on experimental and analytical results, the conclusions are drawn as below:

- 382 1. Experimental results demonstrated that the simplified concentrated loading (CL) regime may
383 mistakenly identify the failure mode of reinforced concrete (RC) beam-column sub-assemblages

384 under a middle column removal scenario. For the specimens tested with the CL regime, the first
385 rebar fracture occurred at the bottom rebar near the middle column. For the specimens subjected
386 to sequential loading (SL) regime, the first rebar fracture occurred at the top rebar near the side
387 column.

- 388 2. The tests with the CL regime could accurately predict the yield strength and the first peak strength
389 (or termed as compressive arch action capacity) of the specimens. However, the CL regime may
390 significantly over-estimate the deformation capacity and ultimate strength (or catenary action
391 capacity) of the specimens, resulting in unsafe design in practice.
- 392 3. The span-to-depth ratio significantly affected the yield strength, first peak strength, ultimate
393 strength, and ultimate deformation capacity of the specimens. However, the span-to-depth ratio
394 may not greatly change the chord rotation capacity of the beams.
- 395 4. As the material properties of the beam can be used more sufficiently, the decrease of flexural action
396 capacity in SL-series specimens was milder than that in CL-series specimens. The catenary action
397 capacity of CL/SL-series specimens was controlled by the beam top rebars. Due to different failure
398 modes, catenary action models were separately proposed for CL/SL-series specimens with
399 reasonable accuracy.

400 **Future work**

401 Upon the test results, the limitation of the current study and future research needed are highlighted.
402 The effects of the loading regime on seismically designed specimens should be evaluated in the future
403 as the conclusions of non-seismically designed specimens may not be suitable for seismically designed
404 ones. The effects of parameters that are not involved in this study on the deformation capacity of RC
405 specimens subjected to the SL regime should be investigated. The reliability of the proposed models
406 should be further validated by more tests. Furthermore, the effects of boundary conditions need to be
407 quantified by numerical studies.

408 **Acknowledgements**

409 The authors gratefully acknowledge the financial support provided by the National Natural
410 Science Foundation of China (Nos. 52022024, 51778153).

411 **References**

- 412 [1] American Society of Civil Engineers (ASCE). Minimum design loads for buildings and other
413 structures, ASCE 7-10. Reston, VA: American Society of Civil Engineers; 2010.
414 [2] General Services Administration (GSA). Progressive collapse analysis and design guidelines for
415 new federal office buildings and major modernization projects, Washington, DC; 2009.
416 [3] Department of Defense (DoD). Design of building to resist progressive collapse. Unified facility
417 criteria, UFC 4-023-03, Washington, DC; 2009.
418 [4] Fu F. Structural analysis and design to prevent disproportionate collapse. CRC Press; 2016.
419 [5] Fu F. Design and analysis of tall and complex structures. Elsevier; 2018.
420 [6] ACI Committee 318, Building Code Requirements for Structural Concrete (ACI 318-14) and
421 Commentary (318R-14). American Concrete Institute, Farmington Hills, MI, 433 pp; 2014.
422 [7] Sasani M, Bazan M, Sagioglu S. Experimental and analytical progressive collapse evaluation of
423 actual reinforced concrete structure. ACI Struct J 2007; 104(6):731–9.
424 [8] Sheffield C, Audrey K, Hoon VNP. An instrumented full-scale building disproportionate collapse
425 test. Proceedings of 14th international symposium on interaction of the effects of munitions with
426 structures 2011. Seattle, Washington; 2011.
427 [9] Yu J, Rinder T, Stolz A, Tan KH, Riedel W. Dynamic progressive collapse of an RC assemblage
428 induced by contact detonation. J Struct Eng 2014; 140(6):04014014.
429 [10] Qian K, Li B. Dynamic performance of RC beam-column substructures under the scenario of the
430 loss of a corner column—Experimental results. Eng Struct 2012; 42:154-67.
431 [11] Peng ZH, Orton SL, Liu JR, Tian Y. Experimental study of dynamic disproportionate collapse in
432 flat-plate buildings subjected to exterior column removal. J Struct Eng 2017; 143(9): 04017125.
433 [12] Qian K, Liang SL, Xiong XY, Fu F, Fang Q. Quasi-static and dynamic behavior of precast concrete
434 frames with high performance dry connections subjected to loss of a penultimate column scenario.
435 Eng Struct 2020; 205:110115.
436 [13] Yi WJ, He QF, Xiao Y, Kunnath SK. Experimental study on disproportionate collapse-resistant
437 behavior of reinforced concrete frame structures. ACI Struct J 2008; 105(4): 433-439.

- 438 [14] Su YP, Tian Y, Song XS. Progressive collapse resistance of axially-restrained frame beams. ACI
439 Struct J 2009; 106(5):600–7.
- 440 [15] FarhangVesali N, Valipour H, Samali B, Foster S. Development of arching action in
441 longitudinally-restrained reinforced concrete beams. Construction and Building Materials 2013;
442 47: 7-19.
- 443 [16] Qian K, Li B. Performance of three-dimensional reinforced concrete beam-column substructures
444 under loss of a corner column scenario. J Struct Eng 2013; 139(4):584-94.
- 445 [17] Yu J, Tan KH. Experimental and numerical investigation on progressive collapse resistance of
446 reinforced concrete beam-column sub-assemblages. Eng Struct 2013; 55: 90–106.
- 447 [18] Yu J, Tan KH. Structural behavior of reinforced concrete beam-column sub-assemblages under a
448 middle column removal scenario. J Struct Eng 2013; 139(2):233-50.
- 449 [19] Lew HS, Main JA, Robert SD, Sadek F. Performance of steel moment connections under a column
450 removal scenario. I: Experiments. J Struct Eng 2013; 139(1): 98-107.
- 451 [20] Lew HS, Bao YH, Pujol S, Sozen MA. Experimental study of reinforced concrete assemblies under
452 column removal scenario. ACI Struct J 2014; 111(4): 881-892.
- 453 [21] Qian K, Li B, Ma JX. Load-carrying mechanism to resist disproportionate collapse of RC
454 buildings. J Struct Eng 2015; 141(2): 04014107.
- 455 [22] Wang W, Fang CF, Qin X, Chen YY, Li L. Performance of practical beam-to-SHS column
456 connections against progressive collapse. Eng Struct 2016; 106: 332–347.
- 457 [23] Ren PQ, Li Y, Lu XZ, Guan H, Zhou YL. Experimental investigation of progressive collapse
458 resistance of one-way reinforced concrete beam-slab substructures under a middle-column-
459 removal scenario. Eng Struct 2016; 118: 28–40.
- 460 [24] Lu XZ, Lin KQ, Li Y, Guan H, Ren PQ, Zhou YL. Experimental investigation of RC beam-slab
461 substructures against disproportionate collapse subject to an edge-column removal scenario. Eng
462 Struct 2017; 149: 91-103.
- 463 [25] Qian K, Li B. Effects of masonry infill wall on the performance of RC frames to resist
464 disproportionate collapse. J Struct Eng 2017; 143(9): 04017118.

- 465 [26] Yu J, Tan KH. Structural behavior of reinforced concrete frames subjected to progressive collapse.
466 ACI Struct J 2017; 114(1): 63-74.
- 467 [27] Wang F, Yang J, Nyunn S, Azim I. Effect of concrete infill walls on the progressive collapse
468 performance of precast concrete framed substructures. Journal of Building Engineering 2020; in
469 press.
- 470 [28] Weng YH, Qian K, Fu F, Fang Q. Numerical investigation on load redistribution capacity of flat
471 slab substructures to resist progressive collapse. Journal of Building Engineering 2020; 29:
472 101109.
- 473 [29] Theodor Krauthammer T, Koha YH. Exploring numerical approaches for pre-test progressive
474 collapse assessment of RC frame structures. Engineering Structures 2019; 201: 109776.
- 475 [30] Yu J, Luo L, Li Y. Numerical study of progressive collapse resistance of RC beam-slab
476 substructures under perimeter column removal scenarios. Eng Struct 2018; 159: 14–27.
- 477 [31] Pham AT, Tan KH, Yu J. Numerical investigations on static and dynamic responses of reinforced
478 concrete sub-assemblages under progressive collapse. Eng Struct 2017; 149: 2–20.
- 479 [32] Liu M. A new dynamic increase factor for nonlinear static alternate path analysis of building
480 frames against progressive collapse. Engineering Structures 2013; 48: 666–673.
- 481 [33] Pham AT, Lim NS, Tan KH. Investigations of tensile membrane action in beam-slab systems under
482 progressive collapse subject to different loading configurations and boundary conditions.
483 Engineering Structures 2017;150: 520–536.
- 484 [34] Ferraioli M. A modal pushdown procedure for progressive collapse analysis of steel frame
485 structures. Journal of Constructional Steel Research 2019; 156: 227–241.
- 486 [35] Ding L, Coile RV, Botte W, Caspee R. Quantification of model uncertainties of the energy-based
487 method for dynamic column removal scenarios. Engineering Structures 2021; 237: 112057.
- 488 [36] Brunesi E, Parisi F. Progressive collapse fragility models of European reinforced concrete framed
489 buildings based on pushdown analysis. Engineering Structures 2017; 152: 579–596.

- 490 [37] Qian K, Weng YH, Fu F, Deng XF. Numerical evaluation of the reliability of using single-story
491 substructures to study progressive collapse behaviour of multi-story RC frames. Journal of
492 Building Engineering 2021; 33: 101636.
- 493 [38] Qian K, Liang SL, Fu F, Li Y. Progressive collapse resistance of emulative precast concrete frames
494 with various reinforcing details. Journal of Structural Engineering 2021; 147(8): 04021107.
- 495 [39] Deng XF, Liang SL, Fu F, Qian K. Effects of high-strength concrete on progressive collapse
496 resistance of reinforced concrete frame. ASCE Journal of Structural Engineering 2020; 146(6):
497 04020078.
- 498 [40] Qian K, Li B. Investigation into resilience of precast concrete floors against progressive collapse.
499 ACI Structural Journal 2019; 116(2):171-182.
- 500 [41] Chadwell CA, Imbsen R. Xtract-Cross Section Analysis software for Structural and Earthquake
501 Engineering.

Table 1-Specimen properties

Test ID	Beam clear span (mm)	Beam longitudinal reinforcement				Loading regime
		A-A section		B-B section		
		Top	Bottom	Top	Bottom	
CL-13	3250	3T12	2T12	2T12	2T12	Concentrated loading
SL-13	3250	3T12	2T12	2T12	2T12	Sequential loading
CL-11	2750	3T12	2T12	2T12	2T12	Concentrated loading
SL-11	2750	3T12	2T12	2T12	2T12	Sequential loading
CL-8	2000	3T12	2T12	2T12	2T12	Concentrated loading
SL-8	2000	3T12	2T12	2T12	2T12	Sequential loading

Table 2-Material properties of reinforcements

Items	Nominal diameter (mm)	Yield strength (MPa)	Ultimate strength (MPa)	Elongation (%)
Longitudinal rebar	T12	438	577	16.6
Transverse links	R6	348	486	25.4

Note: R6 represents plain bar with diameter of 6 mm; T12 represents deformed rebar with diameter of 12 mm.

Table 3-Test results

Test ID	Critical displacements (mm)			Critical loads (kN)			MHCF (kN)	MHTF (kN)	UR (rad)	Lateral stiffness (kN/m)
	YS	FPS	US	YS	FPS	US				
CL-13	45	108	731	33	43	81+	-153	148	0.23	1.0×10^5
SL-13-Shift	43	100	550	31	39	63	-154	111	0.17	
CL-11	36	90	712	37	52	94	-178	154	0.26	
SL-11-Shift	35	90	593	36	49	85	-167	167	0.22	
CL-8	25	79	551	53	77	88	-202	147	0.28	
SL-8-Shift	23	80	357	54	74	63	-224	110	0.18	

Note: YS means yield strength; FPS represents first peak strength; US represents ultimate strength; MHCF means maximum horizontal compressive force; MHTF means maximum horizontal tensile force; and UR indicates ultimate rotation.

List of Figures

Fig. 1. Loading regimes for disproportionate collapse studies: (a) dynamic loading regime; (b) concentrated loading regime; (c) sequential loading regime

Fig. 2. Dimension and reinforcement details of Specimens: (a) CL-13/SL-13; (b) CL-11/SL-11; (c) CL-8/SL-8; (d) cross-section (Note: Unit in mm)

Fig. 3. Test setup for the concentrated loading regime: (a) picture; (b) schematic diagram

Fig. 4. Test setup for the sequential loading regime: (a) picture; (b) schematic diagram

Fig. 5. Comparison of load-displacement curves: (a) CL-13&SL-13; (b) CL-11&SL-11; (c) CL-8&SL-8

Fig. 6. Crack pattern development: (a) CL-13; (b) SL-13; (c) CL-11; (d) SL-11; (e) CL-8; (f) SL-8

Fig. 7. Failure mode and crack pattern of Specimen CL-13

Fig. 8. Failure mode and crack pattern of Specimen SL-13

Fig. 9. Failure mode and crack pattern of Specimen CL-11

Fig. 10. Failure mode and crack pattern of Specimen SL-11

Fig. 11. Failure mode and crack pattern of Specimen CL-8

Fig. 12. Failure mode and crack pattern of Specimen SL-8

Fig. 13. Comparison of horizontal reaction force-displacement curves: (a) CL-13&SL-13; (b) CL-11&SL-11; (c) CL-8&SL-8

Fig. 14. Deflection shape of the beams at various stages: (a) CL-13; (b) SL-13; (c) CL-11; (d) SL-11; (e) CL-8; (f) SL-8

Fig. 15. Strain gauge results of CL-13: (a) close to side column; (b) close to middle column

Fig. 16. Strain gauge results of SL-13: (a) close to side column; (b) close to middle column

Fig. 17. Strain gauge results of CL-11: (a) close to side column; (b) close to middle column

Fig. 18. Strain gauge results of SL-11: (a) close to side column; (b) close to middle column

Fig. 19. Strain gauge results of CL-8: (a) close to side column; (b) close to middle column

Fig. 20. Strain gauge results of SL-8: (a) close to side column; (b) close to middle column

Fig. 21. Effect of early rebar fracture on catenary action: (a) before rebar fracture; (b) fracture of beam bottom rebar at BENM; (c) fracture of beam top rebar at BENS

Fig. 22. Determination of load transfer mechanism at selected beam section: (a) CL-series; (b) SL-series

Fig. 23. Load transfer mechanisms at different beam sections of CL-13: (a) BENM; (b) BENS

Fig. 24. Load transfer mechanisms at different beam sections of SL-13: (a) BENM; (b) BENS

Fig. 25. Load transfer mechanisms at different beam sections of CL-11: (a) BENM; (b) BENS

Fig. 26. Load transfer mechanisms at different beam sections of SL-11: (a) BENM; (b) BENS

Fig. 27. Load transfer mechanisms at different beam sections of CL-8: (a) BENM; (b) BENS

Fig. 28. Load transfer mechanisms at different beam sections of SL-8: (a) BENM; (b) BENS

Fig. 29. Relationship of bending moment v.s. deflection at different cross-sections: (a) CL-13; (b) SL-13; (c) CL-11; (d) SL-11; (e) CL-8; (f) SL-8

Fig. 30. M-N diagram at BENM: (a) CL-13; (b) SL-13; (c) CL-11; (d) SL-11; (e) CL-8; (f) SL-8

Fig. 31. Definition of the rotation of φ and α for SL-series and CL-series specimens: (a) φ for SL-series; (b) α for CL-series

1
2
3
4
5
6
7
8
9
10
11
12
13
14
15
16
17
18
19
20
21
22
23
24
25
26
27
28
29
30
31
32
33
34
35
36
37
38
39
40
41
42
43
44
45
46
47
48
49
50
51
52
53
54
55
56
57
58
59
60
61
62
63
64
65

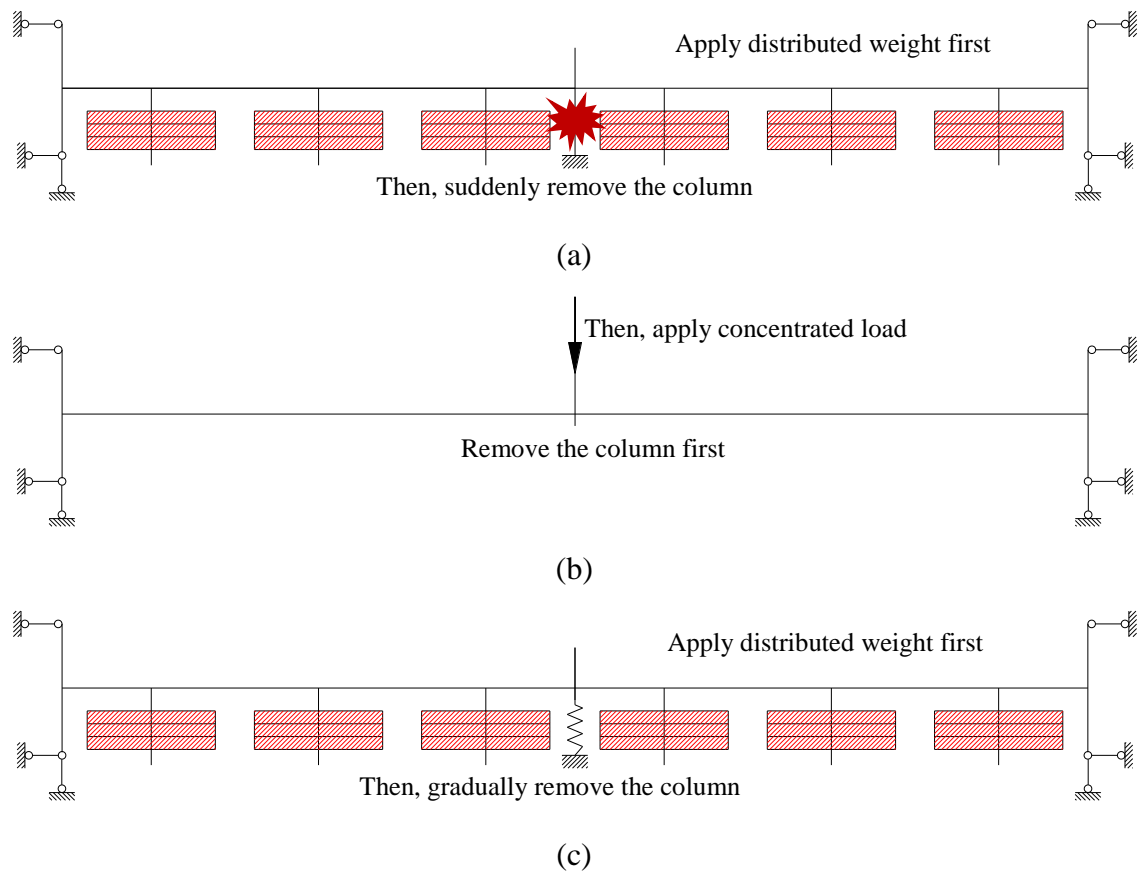
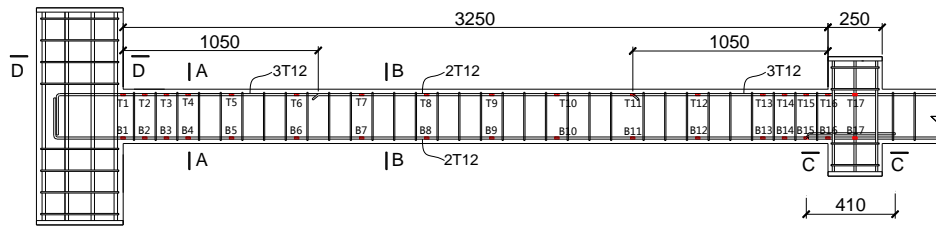
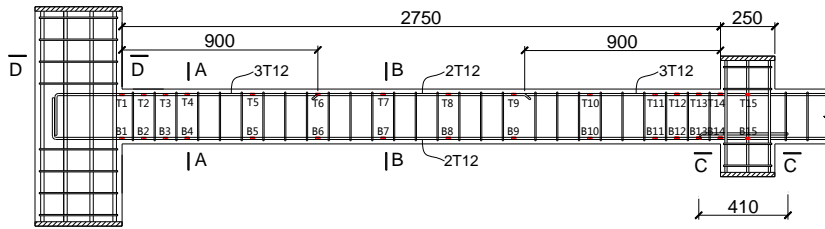


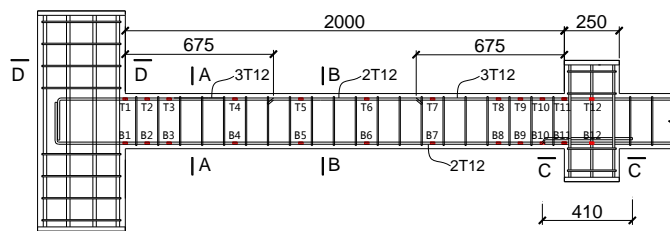
Fig. 1. Loading regimes for disproportionate collapse studies: (a) dynamic loading regime; (b) concentrated loading regime; (c) sequential loading regime



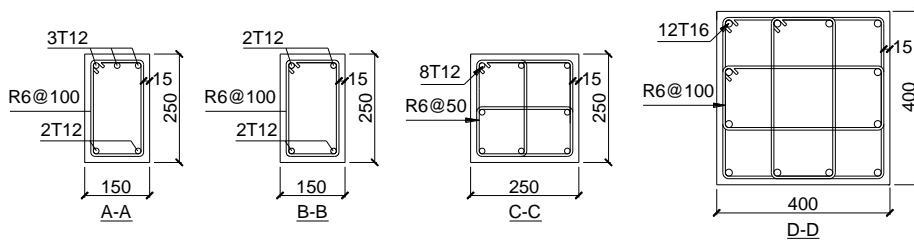
(a)



(b)

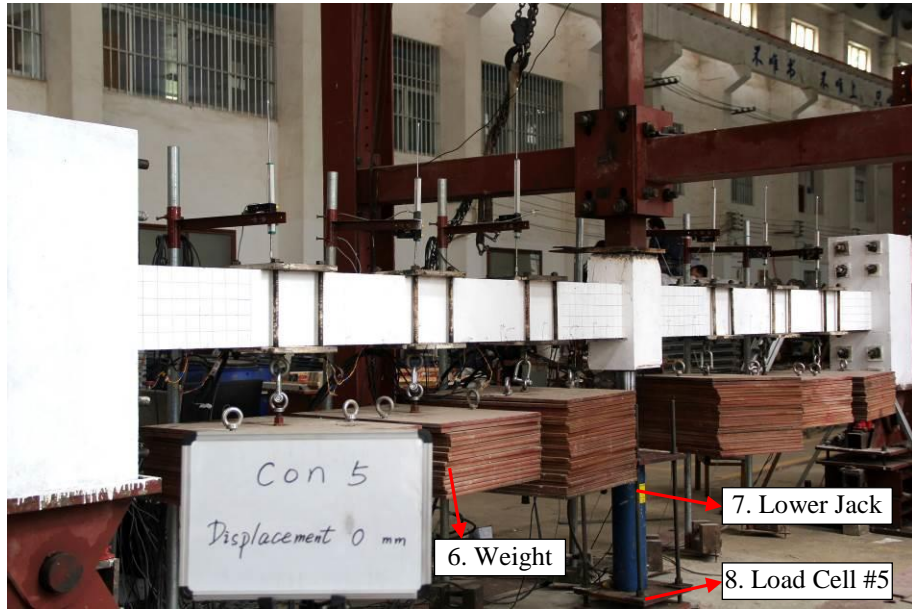


(c)

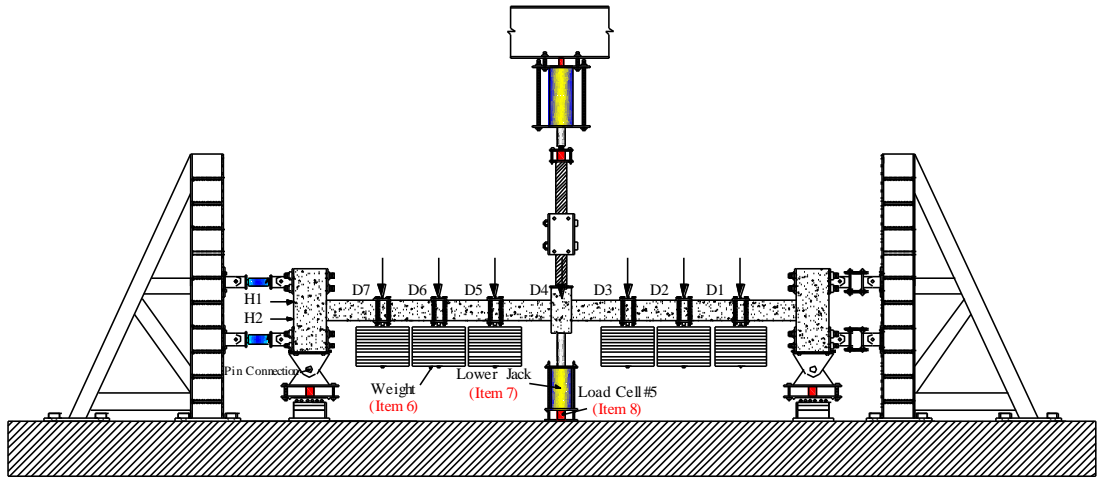


(d)

Fig. 2. Dimension and reinforcement detailing of specimens: (a) CL/SL-13-13; (b) CL/SL-11; (c) CL/SL-8; (d) cross-section (Unit: mm)



(a)



(b)

Fig. 4. Test setup for the sequential loading regime: (a) picture; (b) schematic diagram

1
2
3
4
5
6
7
8
9
10
11
12
13
14
15
16
17
18
19
20
21
22
23
24
25
26
27
28
29
30
31
32
33
34
35
36
37
38
39
40
41
42
43
44
45
46
47
48
49
50
51
52
53
54
55
56
57
58
59
60
61
62
63
64
65

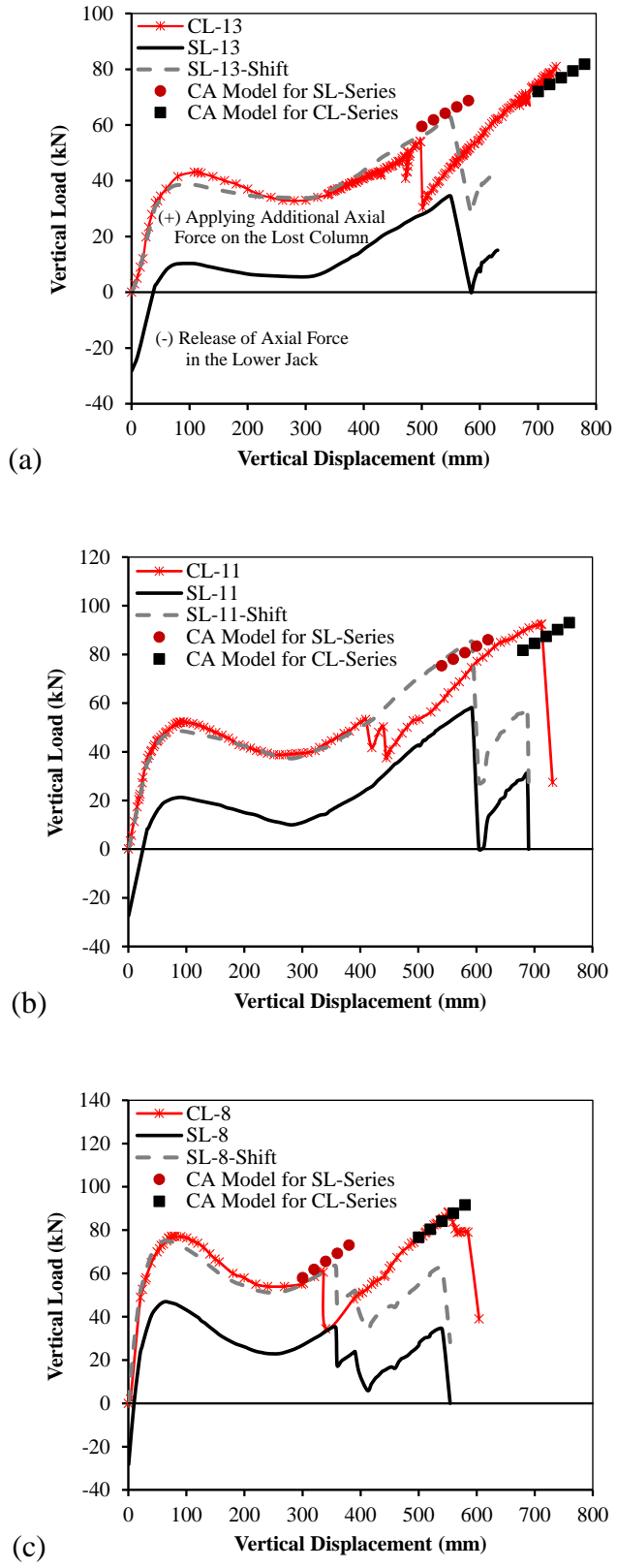
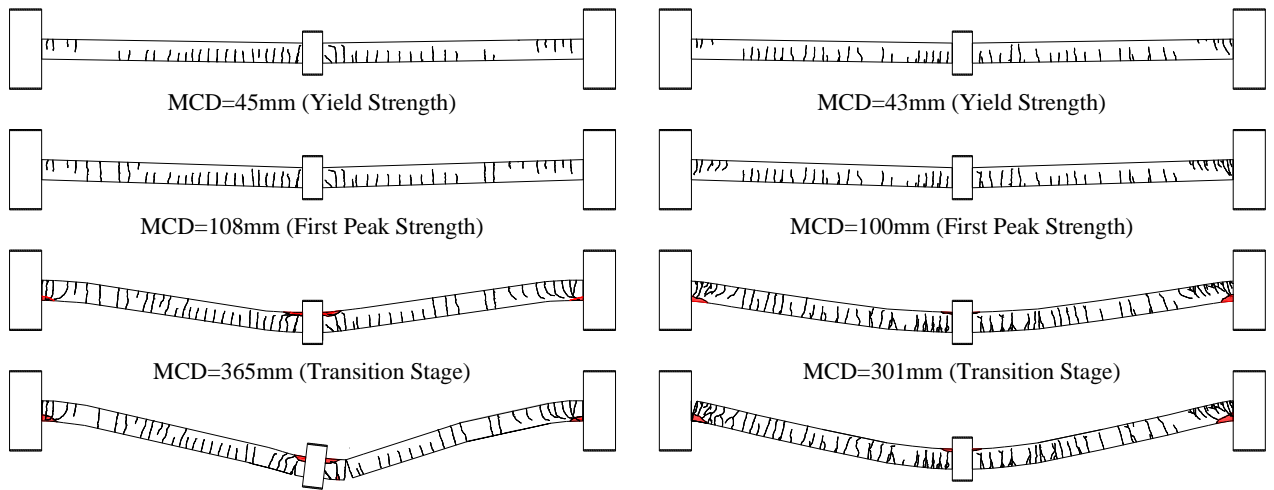
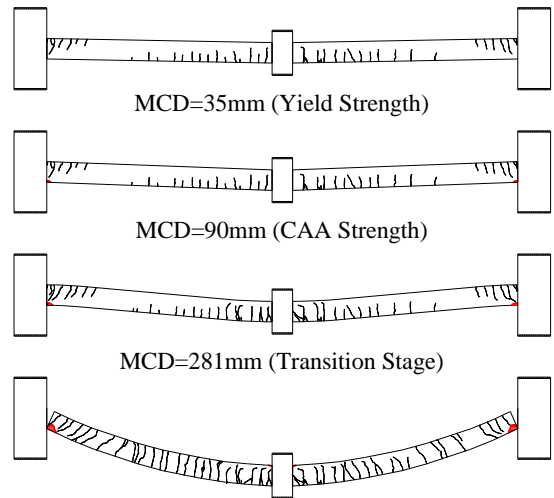
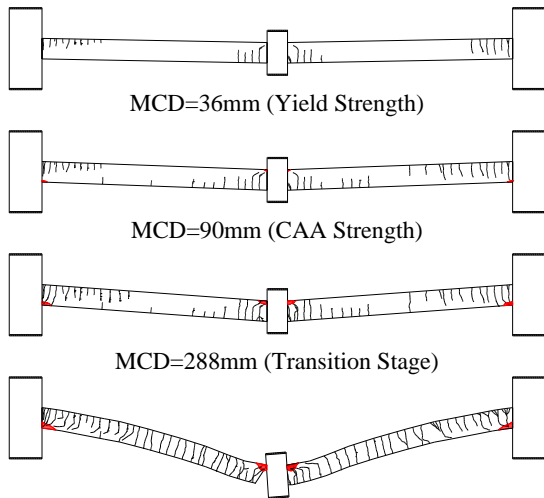


Fig. 5. Comparison of load-displacement curves: (a) CL-13&SL-13; (b) CL-11&SL-11; (c) CL-8&SL-8



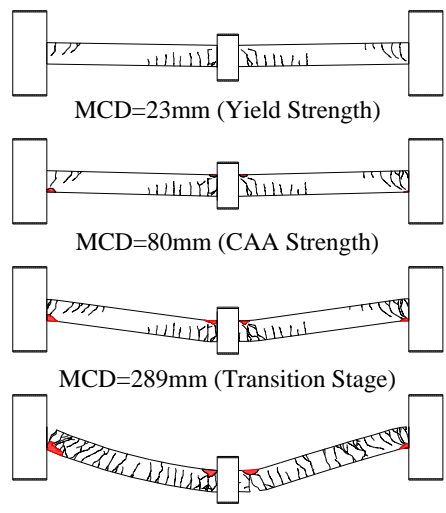
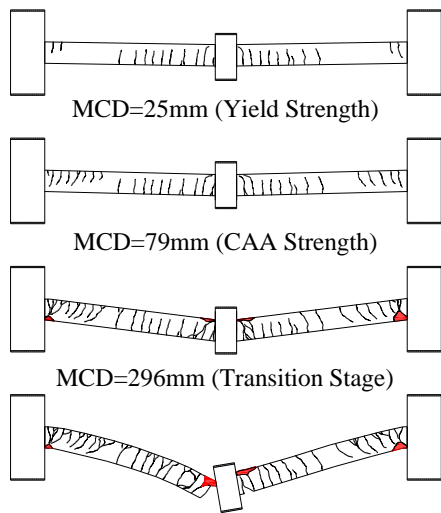
(a)

(b)



(c)

(d)



(e)

(f)

Fig. 6. Crack pattern development: (a) CL-13; (b) SL-13; (c) CL-11; (d) SL-11; (e) CL-8; (f)

SL-8

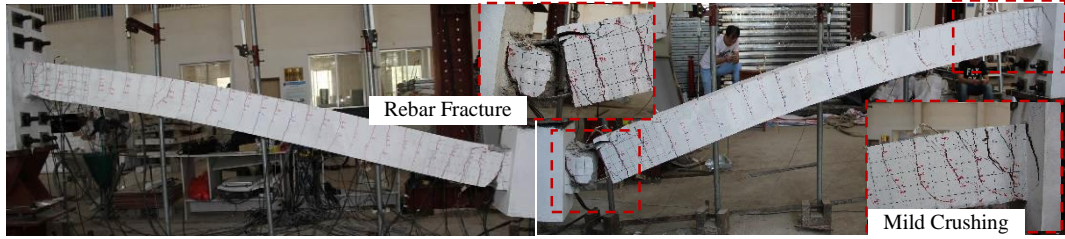


Fig. 7. Failure mode of specimen CL-13



Fig. 8. Failure mode and crack pattern of specimen SL-13

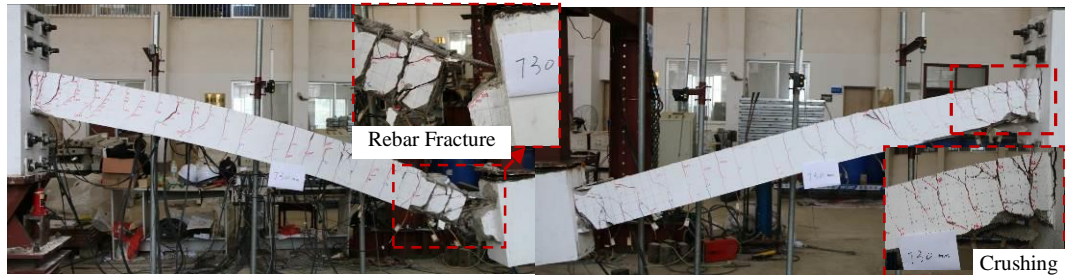


Fig. 9. Failure mode and crack pattern of specimen CL-11



Fig. 10. Failure mode and crack pattern of specimen SL-11

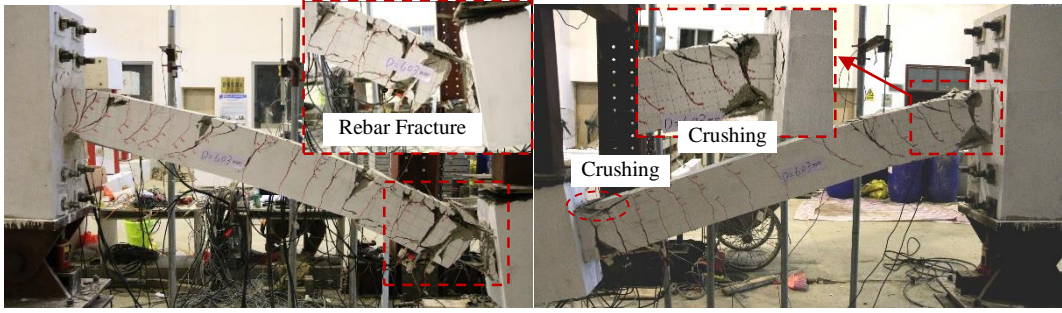


Fig. 11. Failure mode and crack pattern of specimen CL-8

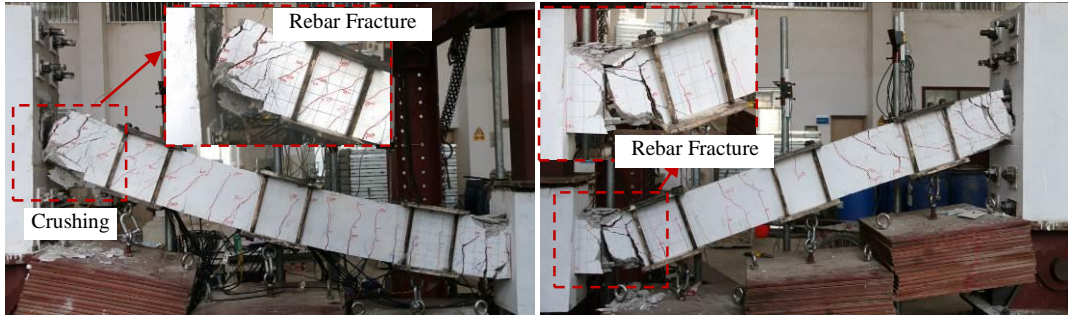


Fig. 12. Failure mode and crack pattern of specimen SL-8

1
2
3
4
5
6
7
8
9
10
11
12
13
14
15
16
17
18
19
20
21
22
23
24
25
26
27
28
29
30
31
32
33
34
35
36
37
38
39
40
41
42
43
44
45
46
47
48
49
50
51
52
53
54
55
56
57
58
59
60
61
62
63
64
65

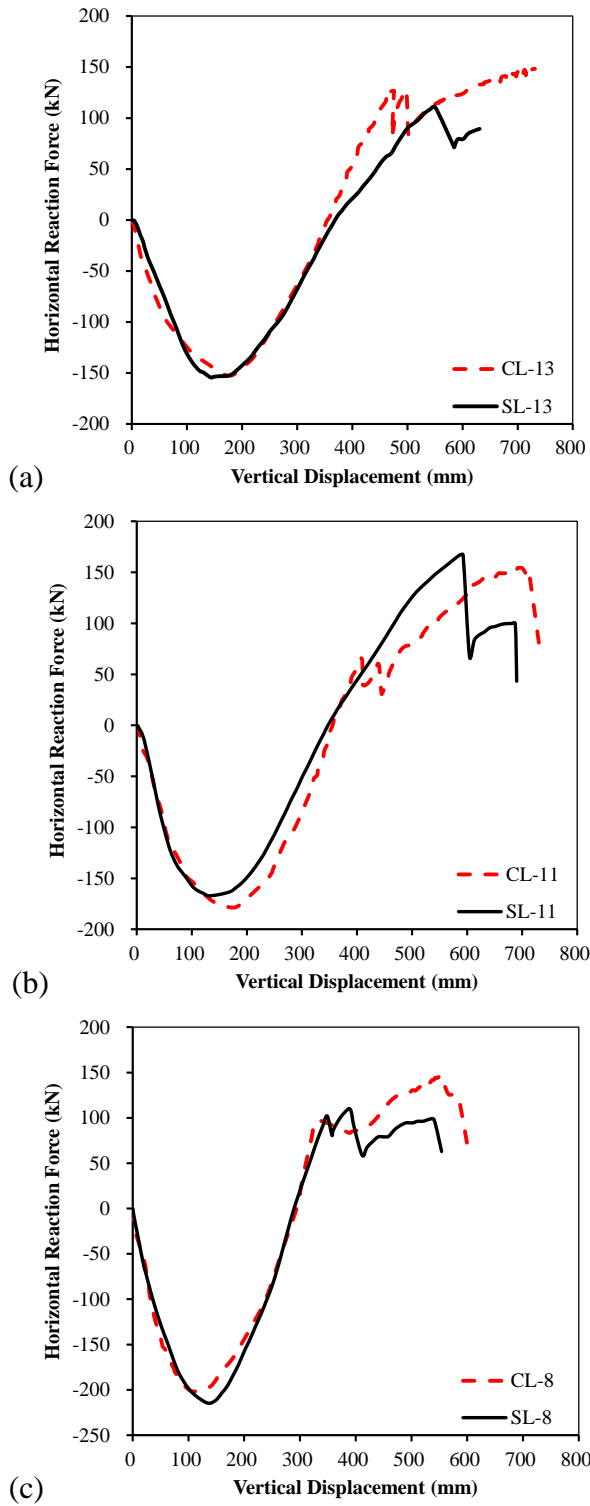


Fig. 13. Comparison of horizontal reaction force-displacement curves: (a) CL-13&SL-13; (b) CL-11&SL-11; (c) CL-8&SL-8

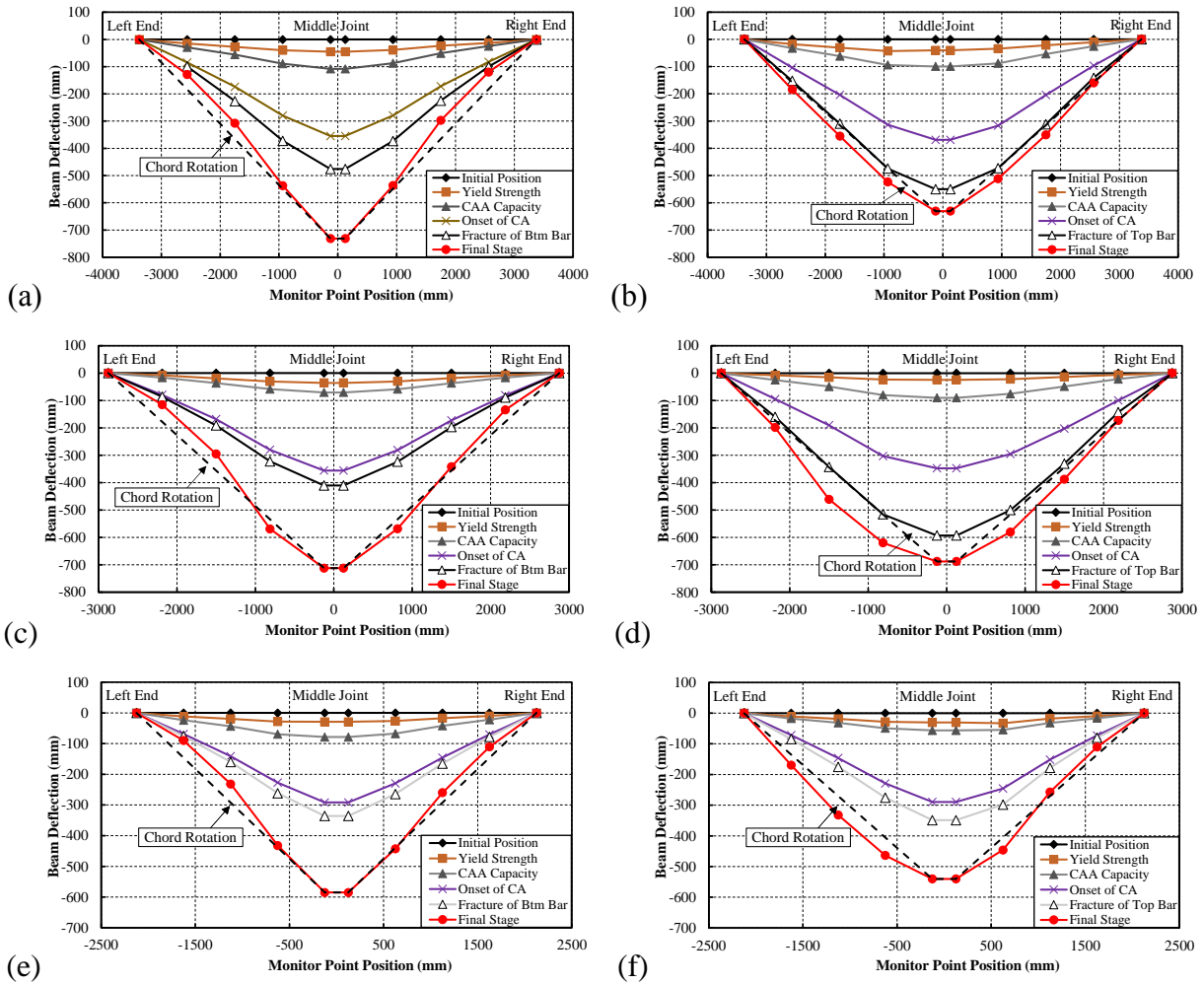


Fig. 14. Deflection shape of the beams at various stages: (a) CL-13; (b) SL-13; (c) CL-11; (d) SL-11; (e) CL-8; (f) SL-8

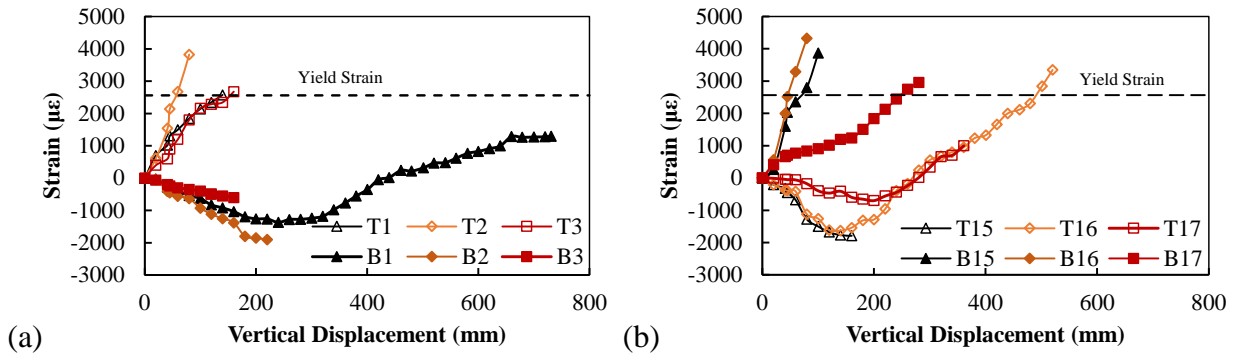


Fig. 15. Strain gauge results of CL-13: (a) close to side column; (b) close to middle column

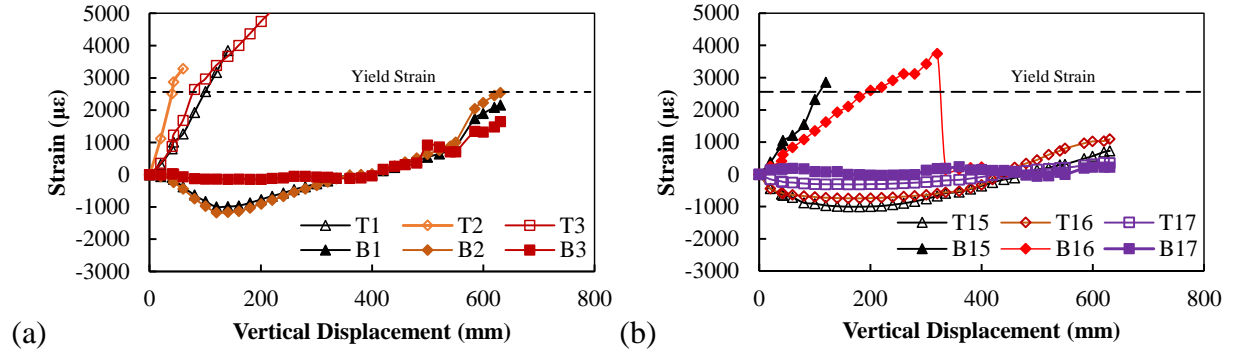


Fig. 16. Strain gauge results of SL-13: (a) close to side column; (b) close to middle column

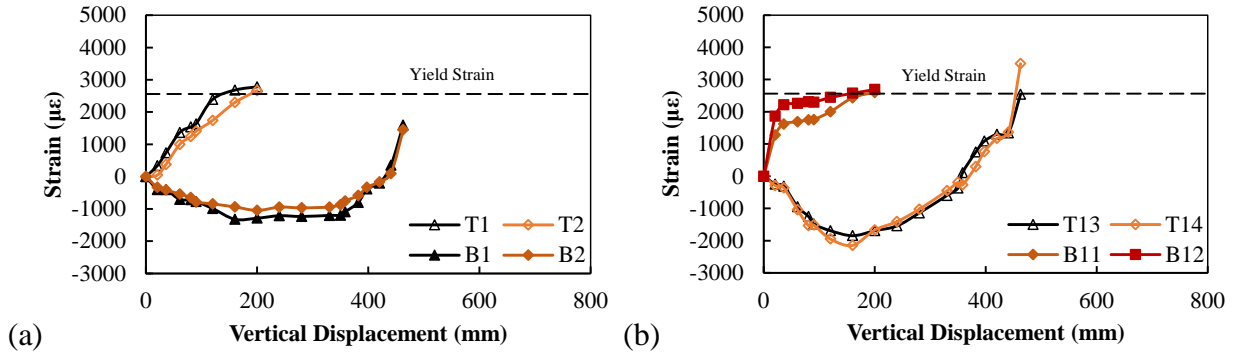


Fig. 17. Strain gauge results of CL-11: (a) close to side column; (b) close to middle column

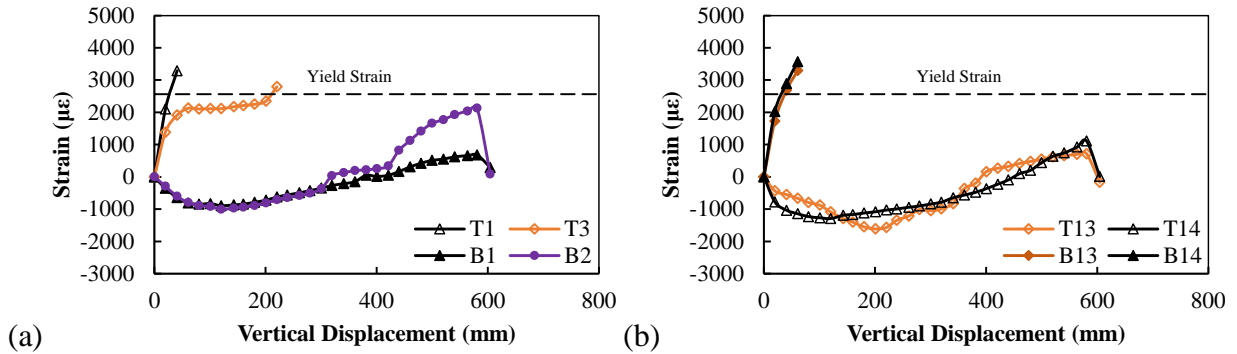


Fig. 18. Strain gauge results of SL-11: (a) close to side column; (b) close to middle column

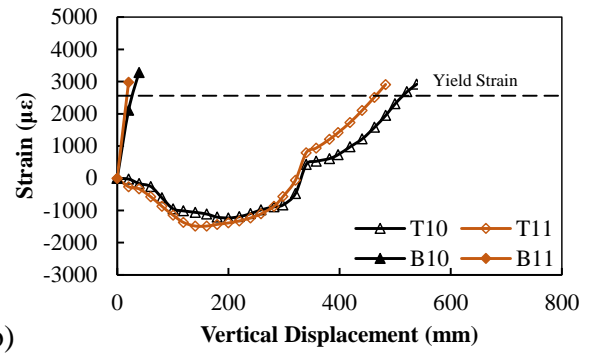
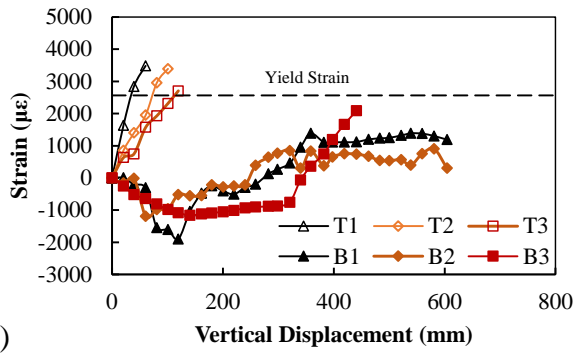


Fig. 19. Strain gauge results of CL-8: (a) close to side column; (b) close to middle column

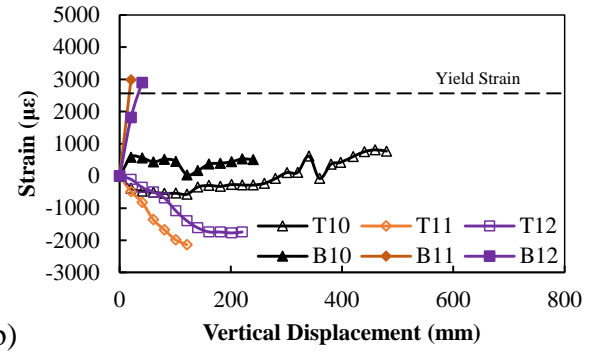
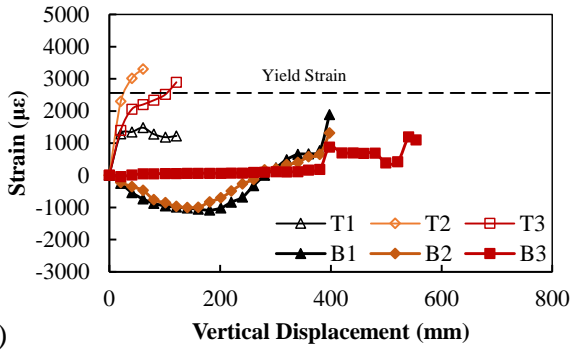


Fig. 20. Strain gauge results of SL-8: (a) close to side column; (b) close to middle column

1
2
3
4
5
6
7
8
9
10
11
12
13
14
15
16
17
18
19
20
21
22
23
24
25
26
27
28
29
30
31
32
33
34
35
36
37
38
39
40
41
42
43
44
45
46
47
48
49
50
51
52
53
54
55
56
57
58
59
60
61
62
63
64
65

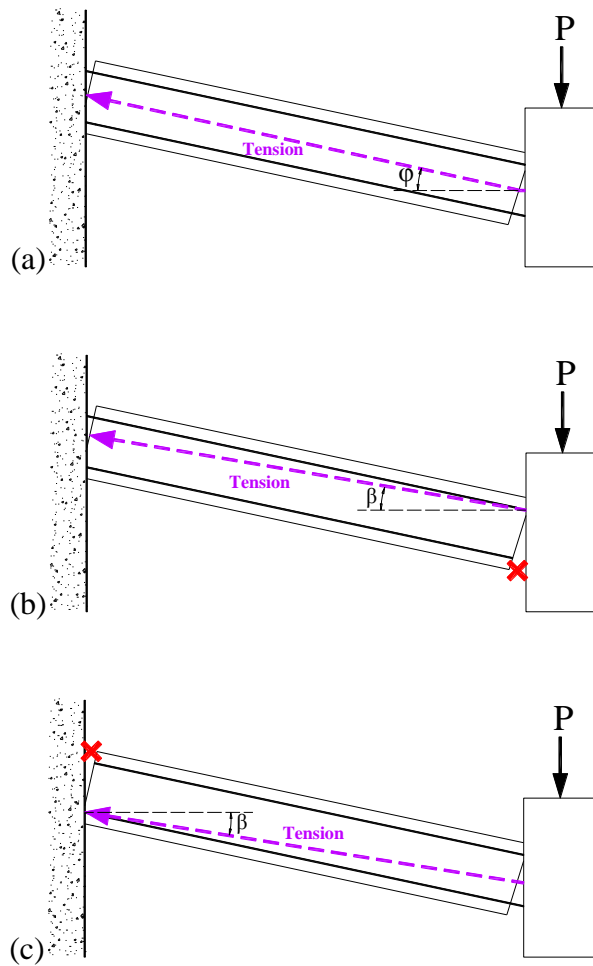


Fig. 21. Effect of early rebar fracture on catenary action: (a) before rebar fracture; (b) fracture of beam bottom rebar at BENM; (c) fracture of beam top rebar at BENS

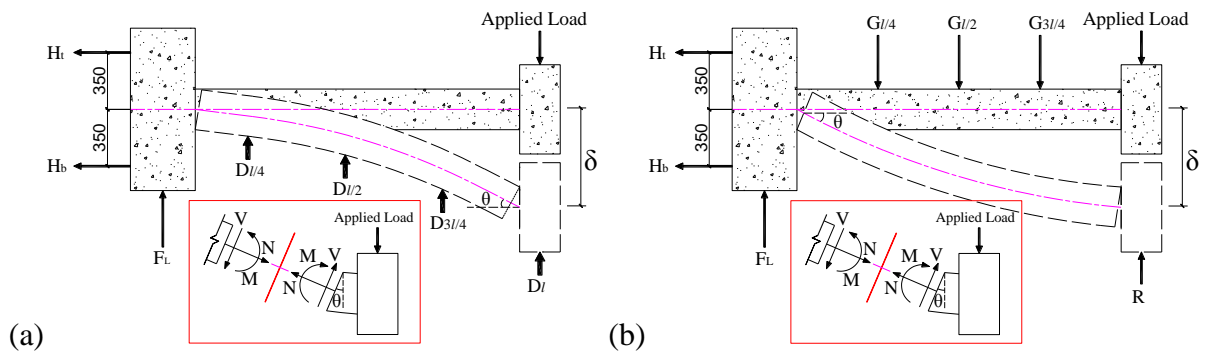


Fig. 22. Determination of load transfer mechanisms at selected beam section: (a) CL-series; (b) SL-series

1
2
3
4
5
6
7
8
9
10
11
12
13
14
15
16
17
18
19
20
21
22
23
24
25
26
27
28
29
30
31
32
33
34
35
36
37
38
39
40
41
42
43
44
45
46
47
48
49
50
51
52
53
54
55
56
57
58
59
60
61
62
63
64
65

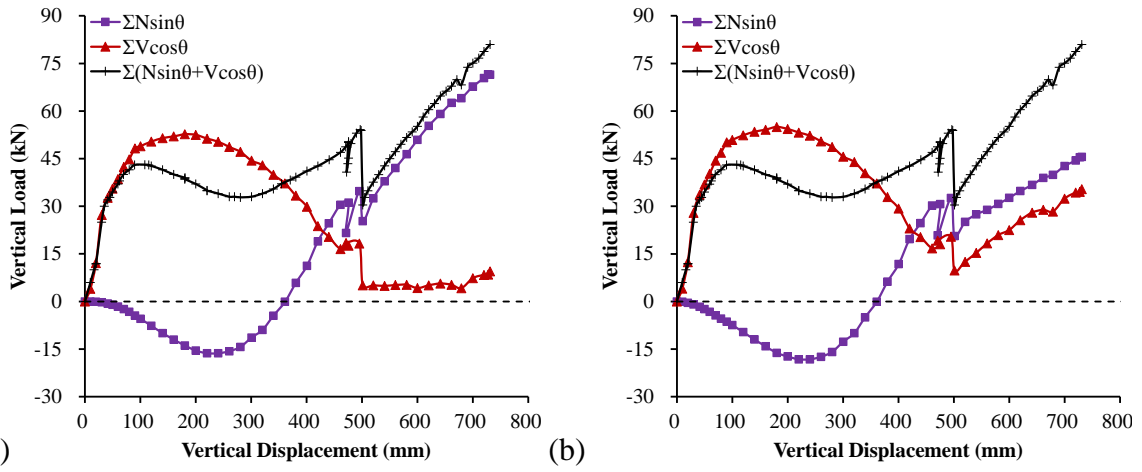


Fig. 23. Load transfer mechanisms at different beam sections of CL-13: (a) BENM; (b) BENS

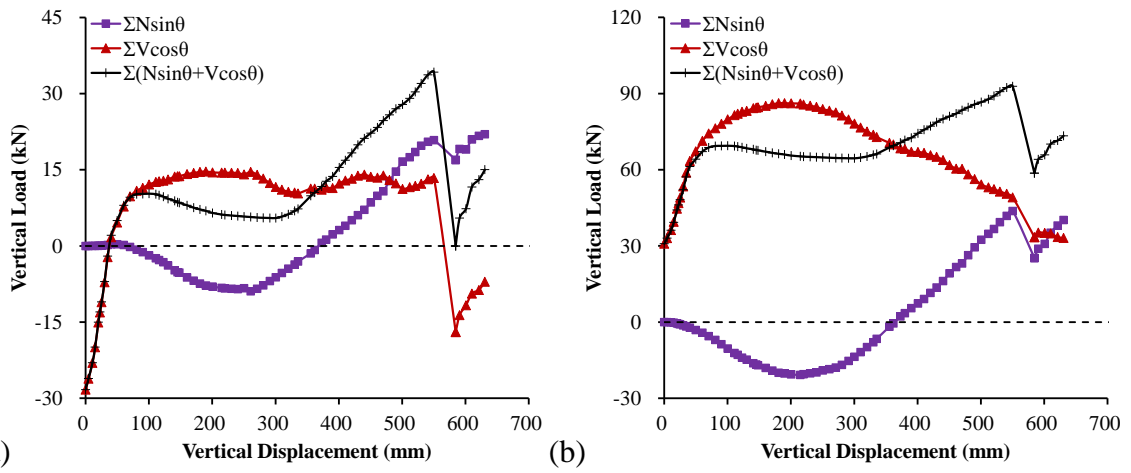


Fig. 24. Load transfer mechanisms at different beam sections of SL-13: (a) BENM; (b) BENS

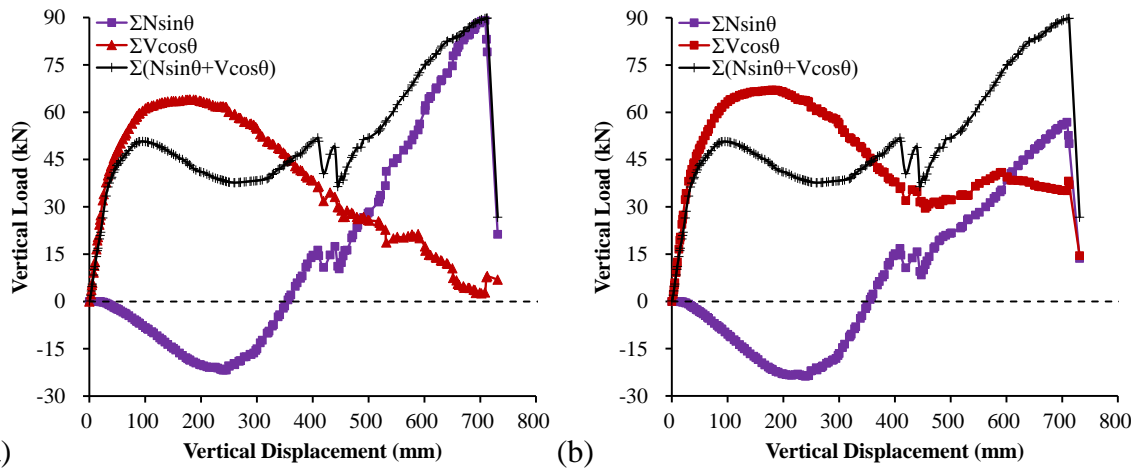


Fig. 25. Load transfer mechanisms at different beam sections of CL-11: (a) BENM; (b) BENS

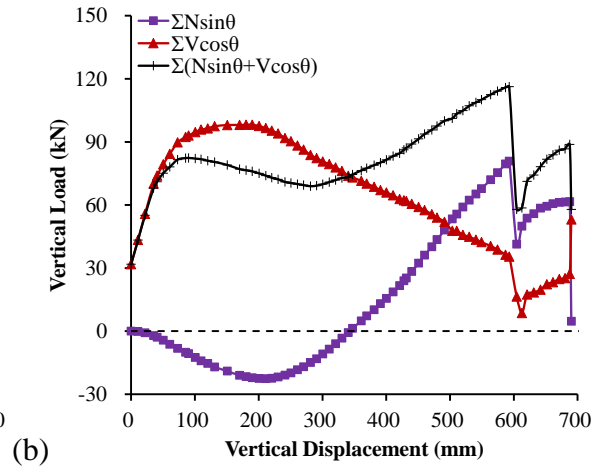
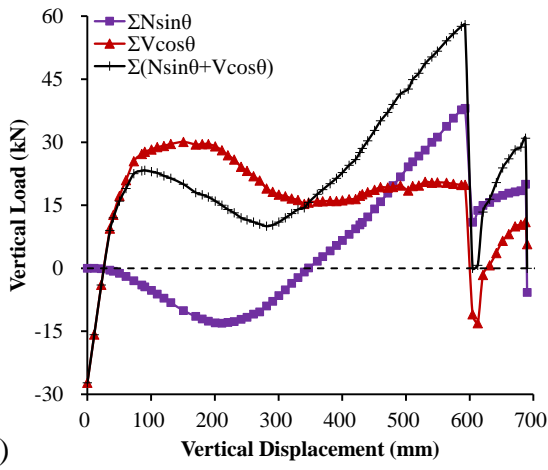


Fig. 26. Load transfer mechanisms at different beam sections of SL-11: (a) BENM; (b) BENS

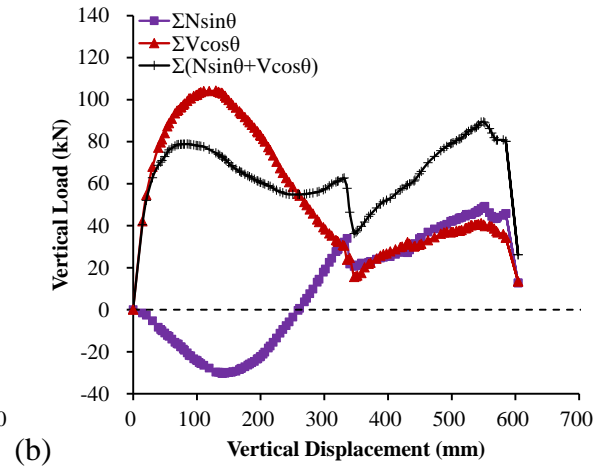
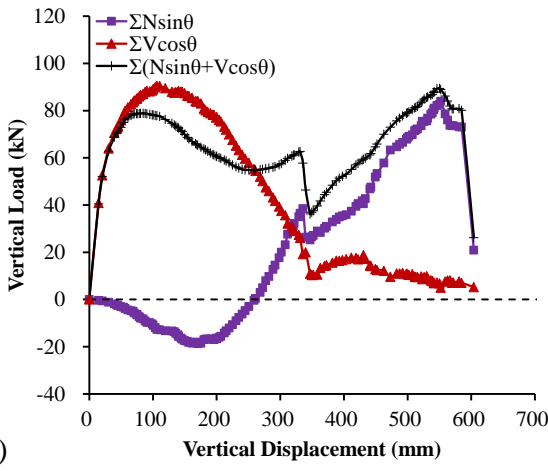


Fig. 27. Load transfer mechanisms at different beam sections of CL-8: (a) BENM; (b) BENS

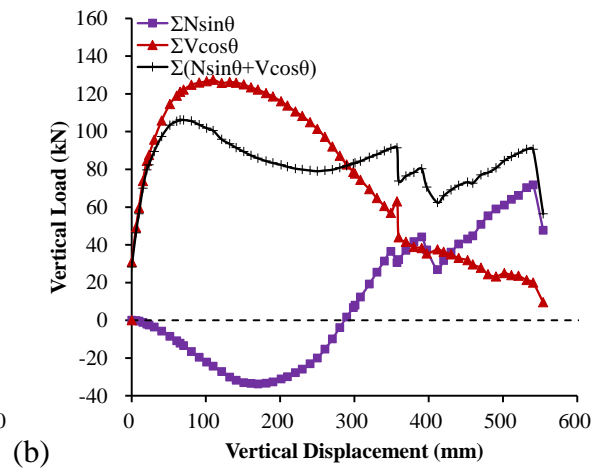
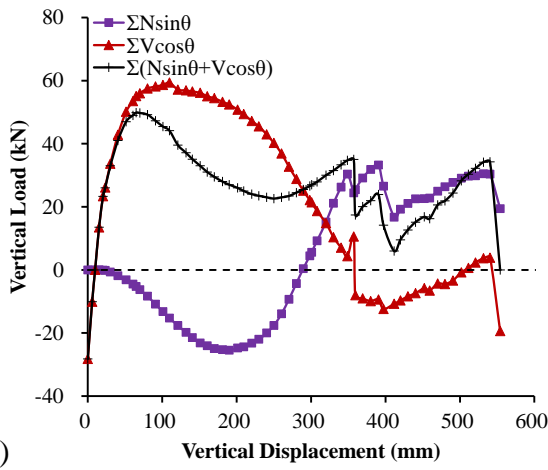


Fig. 28. Load transfer mechanisms at different beam sections of SL-8: (a) BENM; (b) BENS

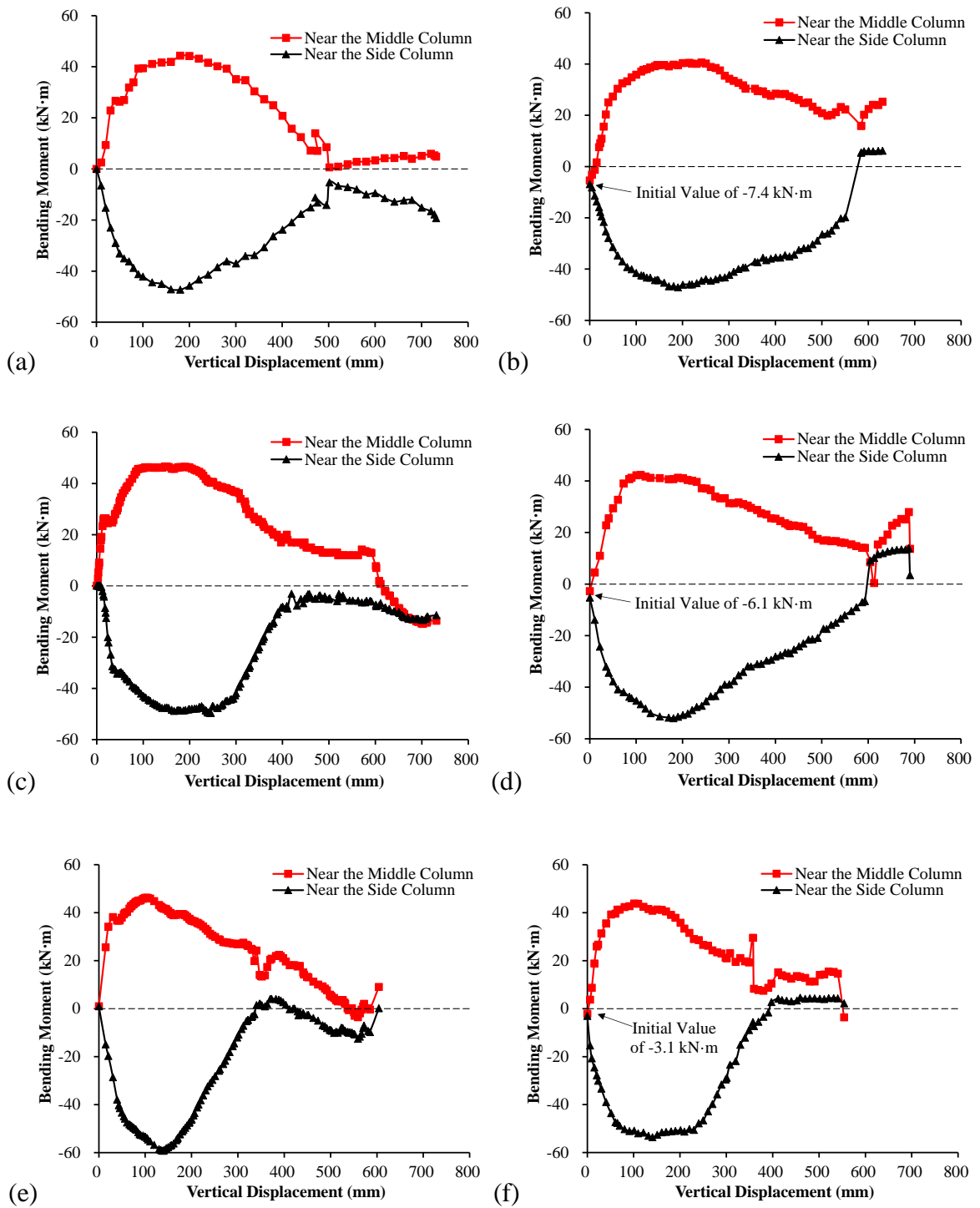


Fig. 29. Relationship of bending moment vs. deflection at different cross-sections: (a) CL-13; (b) SL-13; (c) CL-11; (d) SL-11; (e) CL-8; (f) SL-8

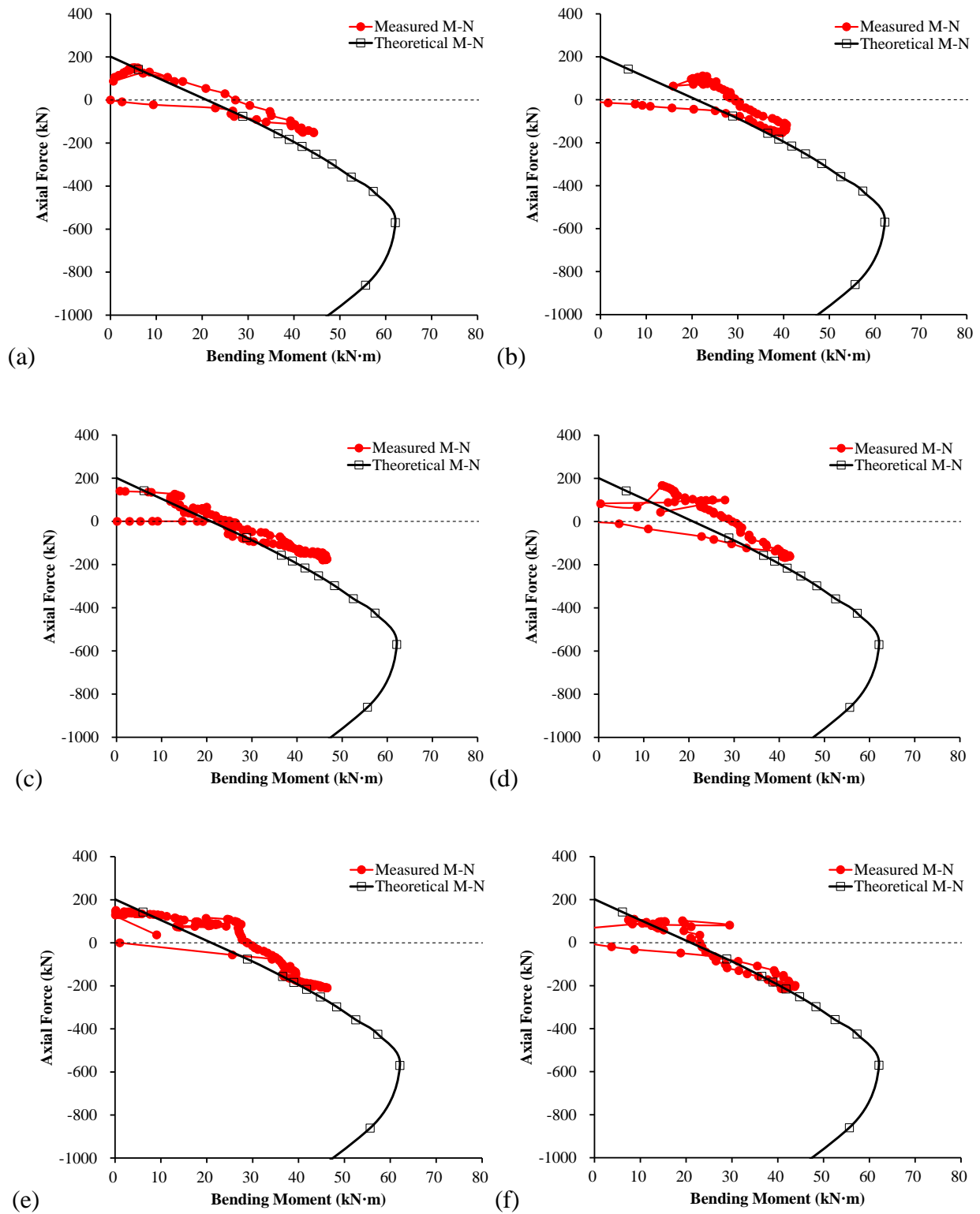


Fig. 30. *M-N* diagram at BENM: (a) CL-13; (b) SL-13; (c) CL-11; (d) SL-11; (e) CL-8; (f) SL-8

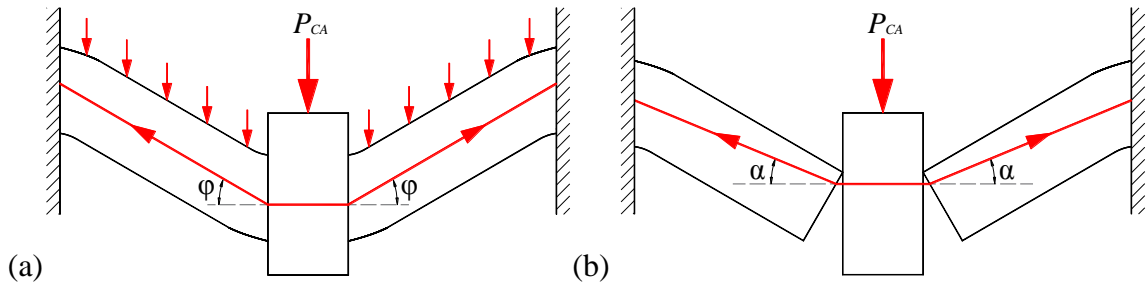


Fig. 31. Definition of the rotation of φ and α for SL-series and CL-series specimens: (a) φ for SL-

1
2
3
4
5
6
7
8
9
10
11
12
13
14
15
16
17
18
19
20
21
22
23
24
25
26
27
28
29
30
31
32
33
34
35
36
37
38
39
40
41
42
43
44
45
46
47
48
49
50
51
52
53
54
55
56
57
58
59
60
61
62
63
64
65

Effects of loading regimes on **the** structural behavior of RC beam-column sub-assemblages against disproportionate collapse

Kai Qian¹, Song-Yuan Geng¹, Shi-Lin Liang², Feng Fu³, and Jun Yu^{2*}

¹GuangXi Key Laboratory of New Energy and Building Energy Saving, Guilin University of Technology, Guilin, China, 541004.

² College of Civil and Transportation Engineering, Hohai University, Nanjing, China, 210098.

³ School of Mathematics, Computer Science and Engineering, City, University of London, U.K.

Abstract:

The majority of previous quasi-static tests on disproportionate collapse simulated the column removal through applying concentrated load/displacement on the top of the removed column until failure.

However, uniformly distributed service load always exists on the frames. Therefore, to reflect the actual load condition more accurately, uniformly distributed load should be applied along the beams first.

Then, the temporary support is gradually removed to simulate the process of column removal. By this

way, the beams may undergo only a small deflection as the dynamic effect is neglected. Thus, a

subsequent concentrated loading process is employed to evaluate the behavior of the beams at the

ultimate stage, which may be reached if the dynamic effect is considered. Such a loading process is

named sequential loading regime. To evaluate the effects of loading regimes on the behavior of

reinforced concrete (RC) frames under a middle column removal scenario, two series of half-scale RC

beam-column sub-assemblages were tested in this study. It is found that the conventional concentrated

loading regime could accurately estimate the yield strength and the compressive arch action capacity

of the RC beam-column sub-assemblages, but it may over-estimate the catenary action (CA) capacity

and the deformation capacity. Moreover, although the concentrated loading regime is convenient and

able to demonstrate the load transfer mechanisms of the sub-assemblages against disproportionate

collapse, it may mistakenly identify the locations of critical sections. Furthermore, based on the failure

* Corresponding author. E-mail address: yujun@hhu.edu.cn

26 modes and local strain gauge results, analytical models were proposed for predicting the CA capacity
27 of the tested specimens under two loading regimes. Results suggest that the analytical models could
1
28 predict the CA capacity well.

3
4
5
29 **Keywords:** Loading regimes; Disproportionate collapse; Reinforced concrete; Load transfer
6
7
30 mechanisms

9
10
11
12
13
14
15
16
17
18
19
20
21
22
23
24
25
26
27
28
29
30
31
32
33
34
35
36
37
38
39
40
41
42
43
44
45
46
47
48
49
50
51
52
53
54
55
56
57
58
59
60
61
62
63
64
65

32 1. Introduction

33 Disproportionate collapse is defined as the spread of an initial local failure from element to
34 element, which eventually results in the collapse of an entire structure or a disproportionately large part
35 of it [1]. After the terrorist attack of Murrah Federal Building in 1995 and Twin Towers of World Trade
36 Center in 2001, disproportionate collapse of buildings due to intentional or accidental events attracted
37 great attention in the structural engineering community. Design guidelines [2-3] were developed for
38 preventing disproportionate collapse, in which indirect and direct design methods were proposed [4-
39 5]. For the indirect method, the capacity of buildings against disproportionate collapse is improved by
40 the implicit requirement of their redundancy, ductility, continuity, and integrity. For example, ACI
41 318-14 [6] requires the continuity of steel reinforcing bars in concrete members. For the direct method,
42 the specific local resistance method and alternate load path method were proposed. Since the specific
43 local resistance method is implemented with an assumed initial threat, such as an accurate estimate of
44 the weight and standoff distance of explosives, it is not commonly used in practical design. Conversely,
45 the alternate load path method is threat-independent and more popular in practice. .

46 The alternate load path method focuses on the ability of the remaining building to redistribute the
47 loads after the removal of one or several vertical elements (columns or walls). Several in-situ tests [7-
48 8] were conducted to investigate the structural behavior against disproportionate collapse. Specifically,
49 Sasani et al. [7] carried out an in-situ dynamic test on a 10-story RC frame before dismantling. The
50 target column was explosively removed, but it was not completely destroyed. As a result, only elastic
51 response of the frame was recorded. Similarly, Sheffield et al. [8] conducted in-situ dynamic tests on
52 a full-scale four-story RC frame, which was loaded with fixed concrete blocks on the floor to represent
53 the specified dead and live load and then tested by explosively removing a column in sequence. The
54 peak displacement of 236 mm (0.03 rad) was measured after suddenly removing an exterior column,
55 and the residual displacement of 968 mm (0.11 rad) was recorded after removing another adjacent
56 interior column. The afore-mentioned in-situ dynamic tests indicated that the structural members in
57 upper floors above the removed column could work together to redistribute the axial load, which was
58 initially resisted by the removed column. The simple analysis suggested that each story just needed to

59 redistribute the vertical load from its own story, provided that beams and slabs in each story had similar
60 geometrical and material properties as well as reinforcement detailing. Accordingly, single-floor
61 substructures can be equivalently used to study the behavior of multi-story frames.

62 Compared with quasi-static tests, dynamic tests are more complex and the result of a single
63 dynamic test is unable to evaluate the load-carrying capacity of a specimen. Thus, quasi-static tests are
64 preferred. However, it must be answered whether quasi-static tests can be equivalently used to
65 investigate the behavior of the frames to resist disproportionate collapse.

66 Fig.1 shows loading regimes for disproportionate collapse studies. As shown in Fig. 1(a), the
67 uniformly distributed load is applied along the beams first in a dynamic test. Then, the temporary
68 support is quickly knocked down to simulate sudden column removal. Although this method can mimic
69 the actual loading scenario, only a few studies [9-12] adopted this loading regime because such a
70 dynamic test is not convenient to demonstrate the structural behavior of the specimen against
71 disproportionate collapse from small to large deformation. In comparison, the concentrated loading
72 (CL) regime is more popular in experimental and numerical studies [13-39]. As shown in Fig. 1(b), in
73 the CL regime, the column is removed first, and then a concentrated load is applied on the top of the
74 removed column. The CL method is able to demonstrate the structural behavior of the specimen against
75 disproportionate collapse, but it ignores the effect of the uniformly distributed service load on the
76 buildings. Thus, the failure mode may be mistakenly identified. To overcome such defects of the CL
77 regime, sequential loading (SL) regime was proposed [40]. As shown in Fig. 1(c), in the SL regime,
78 the uniformly distributed load is applied along the beams first, and then the temporary support is
79 gradually removed to simulate the process of column removal in a quasi-static way. If the specimen
80 can achieve a new balance after the complete removal of the support, a subsequent CL is employed to
81 evaluate the ultimate behavior of the specimen. Although the SL regime has an inherent defect, it has
82 advantages over the commonly used CL regime because it is closer to the actual loading scenario.

83 As test results are affected by the adopted loading regime, and thus, in this paper it is endeavored
84 to evaluate the effects of loading regimes on the structural behavior of RC frames against

85 disproportionate collapse. Accordingly, a quasi-static experimental program was conducted on two
86 series of specimens, each of which were tested under CL or SL regimes, respectively.

1 37 **2. Experimental program**

3 88 2.1. Test specimens

4
5
6
7
8 89 Two series of half-scale beam-column sub-assemblages were tested under CL or SL regime,
9
10 90 respectively. Each series had three specimens with identical sectional dimensions and reinforcing
11
12 91 details but different span-to-depth ratios. For example, CL/SL-13, CL/SL-11, and CL/SL-8 denote the
13
14 92 specimens in CL- and SL-series and the span-to-depth ratio of 13, 11, and 8, respectively.

15
16
17 93 The specimens were extracted from a prototype building, which was an eight-story frame and
18
19 94 non-seismically designed in accordance with ACI 314-14 [6]. The span lengths of the prototype
20
21 95 building in longitudinal and transverse directions were both 7,000 mm. The designed dead load (DL)
22
23 96 and live load (LL) were 3.0 kPa and 2.5 kPa, respectively. As shown in Fig. 2, each specimen consisted
24
25 97 of a double-span beam, a middle column stub, and two side columns. The size of the half-scale beams
26
27 98 and middle column was 250 mm ×150 mm and 250 mm×250 mm, respectively. As suggested by
28
29 99 previous studies [14, 18], the side columns were enlarged to 400 mm ×400 mm for applying fixed
30
31 100 boundary conditions. The reinforcement detailing of the beams and columns is shown in Fig. 2(d).
32
33 101 Curtailment of beam longitudinal reinforcement complied with non-seismical design and detailing.
34
35 102 T12 and R6 were used for beam longitudinal and transverse rebars, respectively. T16 was utilized for
36
37 103 column longitudinal reinforcement. Note that T16 and T12 represented deformed rebars with a
38
39 104 diameter of 16 mm and 12 mm, respectively, while R6 represented plain rebars with a diameter of 6
40
41 105 mm.

42
43
44 106 Six specimens were cast with the same batch of concrete, of which the designated compressive
45
46 107 strength was all 30 MPa. On the day of the test, the measured concrete cylinder compressive strength
47
48 108 of CL-13, SL-13, CL-11, SL-11, CL-8, and SL-8 was 30.5, 30.1, 31.1, 32.5, 31.7, and 31.9 MPa,
49
50 109 respectively. Table 2 lists the properties of rebar.

110 2.2 Loading regimes and instrumentation

111 The test setup for the CL regime is shown in Fig. 3. Similar to Yu and Tan's work [17], the
122 enlarged side columns were supported by two horizontal pin-pin restraints and a bottom pin support.
123 To ensure statically-determinate of the test setup, a series of rollers were installed beneath the bottom
124 pin support to release horizontal constraints from the ground. During the test, the middle column
125 supported onto the ground was removed first. Then, a hydraulic jack installed above the removed
126 column was used for loading with displacement control at the rate of 0.5 mm/s. Moreover, a specially
127 fabricated steel assembly was placed below the hydraulic jack to prevent out-of-plane failure of the
128 sub-assemblages.

129 As shown in Fig. 3(b), to measure the horizontal reaction forces and bending moments, a
130 tension/compression load cell was installed in each horizontal pin-pin restraint. For monitoring the
131 vertical load redistribution, a load cell was installed beneath each pin support and above the upper
132 hydraulic jack. Seven linear variable displacement transducers (LVDTs) were installed along the
133 beams to record the deformation shape of the beams. Two LVDTs were installed to measure the lateral
134 movement of the side columns and to evaluate the stiffness of horizontal constraints at the side
135 columns. The data logger used in the current study was DH 3816N. The sampling frequency was 5 Hz.
136 All the measurement instruments were produced by Jiangsu Donghua Testing Technology Company.

137 **As shown in Fig. 4, the test setup for the SL regime was almost** the same as that of the CL regime
138 except loading approach. In the SL regime, a hydraulic jack was installed beneath the middle column
139 stub to simulate the ground middle column. After that, six steel weights with a total weight of 6,000
140 kg were hung below the beams. The amount of the steel weight was determined in accordance with the
141 loading requirement of DoD [3], i.e., 1.2DL+0.5LL **for the specimen with a clear span of 3250 mm**
142 **(SL-13). Theoretically, the axial force in the removed column of SL-13** was 29.4 kN (6000
143 kg \times 1/2 \times 0.0098 kN/kg=29.4 kN). However, the measured axial load was only 23.5 kN due to the gaps
144 in the lower jack. To make the measured axial load as close as possible to the theoretical one, the
145 amount of each steel weight was adjusted through trial and error. Eventually, the steel weights near the
146 middle column were determined to be 1200 kg, while the others were 900 kg. To facilitate comparing

137 results, the specimens with a clear span of 2750 mm (SL-11) and 2000 mm (SL-8) were also tested
138 with an initial hanging weight of 6000 kg. After applying the weights, the stroke of the bottom jack
139 began to retract gradually to simulate removing the ground middle column. If the specimens failed to
140 collapse when the initial axial force in the bottom jack dropped to zero, a concentrated load was applied
141 with the upper jack to demonstrate the ultimate behavior of the specimens. Besides the layout of the
142 instrumentation for CL-series specimens, a load cell was installed beneath the bottom jack to measure
143 its axial reaction for SL-series specimens.

144 3. Test results

145 3.1. Global response

146 CL-13 & SL-13: The key test results are listed in Table 3. Fig. 5 and Fig. 6 illustrate the load-
147 displacement curves and the crack pattern development of the specimens, respectively. The first crack
148 of CL-13 was observed at the beam ends near the middle column (BENM) at a middle column
149 displacement (MCD) of 11 mm. Increasing the MCD to 45 mm, the longitudinal reinforcement at
150 BENM **yielded**, corresponding to the yield strength (YS) of 33 kN. Based on structural analysis, the
151 nominal YS of CL-13 is 30 kN, which is about 90 % of the test one. Further increasing the MCD to
152 108 mm, the first peak strength (FPS) due to compressive arch action (CAA) was measured to be 43
153 kN. As shown in Fig. 6(a), slight concrete crushing occurred at the compressive zone of the BENM.
154 With increasing the MCD, concrete at the beam end near the side column (BENS) **was crushed**. The
155 load resistance kept decreasing until the MCD of 300 mm, which was about 0.09 times the clear span
156 length of the beam. After that, the structural resistance re-ascended. At a MCD of 476 mm, the first
157 rebar fracture occurred at the BENM, resulting in a sudden drop of structural resistance. However, the
158 load resistance still kept increasing after the fracture of several rebars in the BENM. When the MCD
159 arrived at 731 mm, the test was stopped as the stroke capacity of the jack was reached. The ultimate
160 strength (US) attributed **to** the mobilization of catenary action (CA) was 81+ kN. Fig. 7 shows the
161 failure mode of CL-13. It is seen that the bottom rebars at BENM were fractured while the top rebars

162 at BENS were still intact. Cracks penetrating through the beam sections were parallelly distributed
163 along the beams, indicating the development of the axial tension at the large deformation stage.

164 For SL-13, as shown in Fig. 5(a), negative axial force was initially measured, which represented
165 the releasing of axial compression of the bottom hydraulic jack. As mentioned in Section 2.2, the steel
166 weight of 6000 kg was hung below the beams before the test for SL-series specimens. Theoretically,
167 the initial axial force of the bottom jack should be -29.4 kN, while the measured one was only -28 kN
168 as the middle column had a vertical movement of 0.6 mm after hanging the weights. When the axial
169 force was reduced to -10 kN, the first crack was observed at the BENS. When the axial force was
170 reduced to 0 kN, i.e., the complete retraction of the bottom jack, the MCD was only 38 mm with no
171 yield of reinforcement. To investigate the US of the specimen, the additional load was applied onto the
172 middle column stub with the upper jack.

173 To simplify the comparison, the starting point of the load-displacement curve of SL-13 was shifted
174 from (0.6, -28) to the origin (0, 0) of the coordinate system, as shown in Fig. 5(a). Accordingly, the
175 values presented for SL-series specimens were based on the shifted curve. For SL-13, the YS of 31 kN
176 was measured at a MCD of 43 mm, close to the one of CL-13. However, the first yield of SL-13 and
177 CL-13 occurred at the longitudinal reinforcement of the BENS and the BENM, respectively. The FPS
178 of SL-13 was 39 kN, about 91% of that of CL-13. The structural resistance of SL-13 began to re-ascend
179 after a MCD of 330 mm, which was almost the same as CL-13. The first rebar fracture of SL-13
180 occurred at the BENS at a MCD of 551 mm, which was later than that of CL-13. Moreover, the
181 successive fracture of two rebars made the structural resistance of SL-13 drop from 63 kN to 28 kN.
182 SL-13 completely lost its resistance at an ultimate MCD of 629 mm, only 86% of that of CL-13. The
183 US of SL-13 was 63 kN, about 78 % of that of CL-13. Fig. 6(b) and Fig. 8 show the crack pattern
184 development and the failure mode of SL-13, respectively. Different from CL-13, no rebar at the BENM
185 of SL-13 was fractured, and instead, severe concrete crushing and rebar fracture were observed at the
186 BENS. In summary, compared with CL-13, the critical section of SL-13 was changed from the BENM
187 to the BENS due to the initial bending moment induced by the hanging weights.

188 CL-11 & SL-11: Fig. 5(b) compares the load-displacement curves of CL-11 and SL-11. The YS
189 and the FPS of CL-11 were 37 kN and 52 kN, respectively. At a MCD of 288 mm, the load resistance
190 of CL-11 started to re-ascend. The first rebar fracture occurred at the BENM at a MCD of 410 mm,
191 resulting in the sudden drop of load resistance from 52 kN to 33 kN. Then, the load resistance kept
192 increasing and reached a US of 94 kN at a MCD of 712 mm. **The YS and FPS of SL-11 were 36 kN**
193 **and 49 kN, respectively.** After reaching the FPS, the load resistance began to decrease due to concrete
194 crushing at the BENS, and re-ascend at a MCD of 281 mm. The load resistance kept increasing until
195 the rebar fracture at the BENS at a MCD of 593 mm, leading to the drop of load resistance from 85 kN
196 to 27 kN. After that, the load resistance slightly increased and the eventual load resistance was 58 kN.
197 Figs. 9 and 10 illustrate the failure mode of CL-11 and SL-11, respectively. Similar to CL-13, rebar
198 fracture occurred at the BENM of CL-11 but with more severe concrete crushing. In comparison, the
199 severe local failure of SL-11 occurred at the BENS.

200 CL-8 & SL-8: Fig. 5(c) compares the load-displacement curves of CL-8 and SL-8. The YS of CL-
201 8 and SL-8 were 53 kN and 54 kN, respectively. The FPS of CL-8 and SL-8 were 77 kN and 74 kN,
202 respectively. Before the first rebar fracture, the load-displacement curves were similar. **The first rebar**
203 **fracture of CL-8 and SL-8 occurred at the BENM and BENS at the MCDs of 330 mm and 357 mm,**
204 **respectively.** Thereafter, CL-8 developed load resistance much faster than SL-8. Eventually, the US of
205 CL-8 and SL-8 was 88 kN and 63 kN, respectively. Fig. 11 shows that severe local damage including
206 rebar fracture and concrete crushing and spalling occurred at one of the BENMs of CL-8. As shown
207 in Fig. 12, for SL-8, the damage of the BENS was more severe than that of the BENM. It was
208 worthwhile to point out that the steel weights touched each other at the large deformation stage due to
209 limited space. As a result, partial gravity of the steel weights at the mid-span was transferred to the
210 BENM, resulting in severe damage in the right-side BENM.

211 3.2. Horizontal reaction forces

212 Fig. 13 compares the horizontal reaction force-displacement curves of CL-series and SL-series
213 specimens. As shown in Fig. 13(a), for CL-13 and SL-13, compressive reaction force was measured

214 **initially**, indicating the development of CAA in the beams. The maximum compressive reaction forces
215 of -153 kN and -154 kN were measured for CL-13 and SL-13, respectively. Therefore, consistent with
216 the vertical load response, the loading regime had little effect on the development of the CAA. The
217 mobilization of tensile reaction forces corresponded to the CA stage, and the maximum tensile reaction
218 forces of CL-13 and SL-13 were 148 kN and 111 kN, respectively. Similarly, as shown in Figs. 13(b
219 and c), the maximum compressive reaction forces of CL-11, SL-11, CL-8, and SL-8 were -178 kN, -
220 167 kN, -202 kN, and -224 kN, respectively. The maximum tensile reaction forces of CL-11, SL-11,
221 CL-8, and SL-8 were 154 kN, 167 kN, 147 kN, and 110 kN, respectively. In general, the loading regime
222 had little effect on the development of the horizontal reaction forces, but it significantly affected the
223 CA, as shown in Fig. 5.

224 3.3. Beam deflection shape

225 Fig. 14 shows the deflection shape of the beams at various stages. Before rebar fracture, the beams
226 deformed in a double-curvature shape. However, as shown in Fig. 14(a), for CL-13, after rebar fracture
227 at the BENM, the single-span beam deformed like a cantilever beam. Thus, the chord rotation, defined
228 as the ratio of the MCD to the beam clear span according to DoD [3], was larger than the local rotation
229 at the BENS. As shown in Fig. 14(b), after rebar fractured at the BENS of SL-13, the deflection shape
230 of the beams was close to that of simply-supported beams. Thus, the chord rotation was smaller than
231 the local rotation at BENS. Similar observations were found in the other specimens.

232 3.4. Strain gauge readings

233 As shown in Fig. 15, **the first yield of rebars at the BENS and BENM of CL-13 occurred at the**
234 **MCDs of 59 mm and 45 mm, respectively.** The bottom rebars at the BENS of CL-13 initially suffered
235 compression and transformed to tension after a MCD of 440 mm. Moreover, the bottom rebars at the
236 BENS of CL-13 yielded at the end of the test. Similarly, the top rebars at the BENM of CL-13 was
237 initially in compression and converted to tension at a MCD of 280 mm. At a MCD of 501 mm, the top
238 rebars at the BENM **yielded**, confirming that the continuous top rebars **contributed** to the development
239 of CA for CL-series specimens.

240 As shown in Fig. 16, for SL-13, the first yield of the rebars at the BENS and BENM was recorded
241 at the MCDs of 43 mm and 120 mm, respectively. Similar to CL-13, the bottom rebars at the BENS of
242 SL-13 finally developed tension and reached yielding, but the top rebars at the BENM failed to yield.
243 As shown in Figs. 17 to 20, similar results were measured in the other specimens.

244 4. Analysis and discussions

245 4.1. Effects of span-to-depth ratio and loading regimes

246 Because the nature of the loading regime is to simulate the load redistribution process of the axial
247 force of the removed column, the ratio of load resistance to the designed axial force of the removed
248 column can directly reflect the risk of progressive collapse. The ratio is given in the bracket behind the
249 load resistance in this Section. The designed axial forces of the removed column in the specimens with
250 the span-to-depth ratio of 13, 11, and 8 were 29.4 kN, 21.6 kN, and 12.2 kN, respectively. As listed in
251 Table 3, the YS of CL-13, CL-11, CL-8, SL-13, SL-11, and SL-8 was 33 kN (1.12), 37 kN (1.71), 53
252 kN (4.34), 31 kN (1.05), 36 kN (1.67), and 54 kN (4.43), respectively. Thus, decreasing the span-to-
253 depth ratio from 13 to 8 increased the YS of CL/SL-series specimens by 61 % and 71 %, respectively.
254 Moreover, when the span-to-depth ratio was decreased from 13 to 8, the FPS increased by 79 % and
255 90 % for CL/ SL-series specimens, respectively. However, the effects of the span-to-depth ratio on the
256 US of the specimens were not clear. For CL-13, CL-11, and CL-8, the US was 81+ kN (2.76+), 94 kN
257 (4.35), and 88 kN (7.21), respectively. For SL-13, SL-11, and SL-8, the US was 63 kN (2.14), 85 kN
258 (3.94), and 63 kN (5.16), respectively. The CL-series specimens developed greater US than the SL-
259 series specimens. This suggested that the structural capacity due to CA depended on the area of
260 continuous reinforcement and the rotation capacity of beam-column connections. As shown in Figs.
261 16, 18, and 20, the tensile strain of the beam bottom rebars at the BENS was relatively small when the
262 US of SL-series specimens was attained. Thus, the US can be attributed to the CA developed mainly
263 in the beam top rebars at the BENS (3T12). In comparison, the US of CL-series specimens was attained
264 when the beam top rebars at the BENM (3T12) were fractured. Therefore, the area of continuous
265 reinforcement that was mobilized to develop the US was identical for the CL/ SL-series specimens.

266 However, the rotational capacity of CL-13 (0.23 rad), CL-11 (0.26 rad) and CL-8 (0.28 rad) were
267 greater than that of SL-13 (0.17 rad), SL-11 (0.22 rad) and SL-8 (0.18 rad), respectively. As a result,
268 the CL-series specimens could develop greater US than the SL-series specimens. In general, from the
269 perspective of resistance/demand ratio, decreasing the span-to-depth ratio is able to reduce the
270 progressive collapse risk.

271 Experimental results show that the loading regimes have little effect on YS and FPS but have
272 significant effects on the deformation capacity and the US. Based on the failure mode, the CL regime
273 may conclude that the bottom rebars at the BENM fracture first. However, in reality, due to the existing
274 distributed loads, the top rebars at the BENS fracture first. As a result, the analytical model for CA
275 derived based on the CL regime may be inaccurate.

276 4.2. Effects of early rebar fracture on catenary action

277 The mobilization of the CA relies on the tension developed in the beam rebars. Similar to Yu and
278 Tan's discussion [26], as shown in Fig. 21(a), the angle between the tension in the beam and the horizon
279 is chord rotation φ before rebar fracture, whereas the angle changes to β after rebar fracture, as shown
280 in Figs. 21(b) and (c). It is evident that the angle β is smaller than the chord rotation φ for a given
281 displacement. Thus, the rebar fracture not only reduces the area of the beam rebars that can develop
282 tension but also decreases the vertical projection of the tension to resist disproportionate collapse.
283 However, the rebar fracture releases the rotation of the beam section, resulting in a greater rotation
284 capacity of the beam end. The increased rotation capacity allows further development of the CA. Fig.
285 5 demonstrates that the CL-series specimens can develop greater CA capacity at the large deformation
286 stage even if early rebar fracture occurred. In comparison, the SL-series specimens achieved their CA
287 capacity at the first rebar fracture because the area of bottom beam rebars was smaller than that of the
288 top rebars.

290 To more deeply understand the structural behavior of RC beam-column sub-assemblages under
 1
 291 **different** loading regimes, an analytical investigation is performed to illustrate the load transfer
 3
 4
 292 mechanisms at different beam sections, similar to the work of Yu and Tan [18]. The internal forces
 6
 293 transferred from the selected beam sections to the adjacent beam sections are illustrated in Fig. 22, the
 8
 9
 294 total vertical component of the internal force (P) at the selected beam sections is composed of vertical
 11
 12
 295 components of the shear force (V) and the axial force (N). According to the force equilibrium along
 13
 14
 296 the vertical direction, P transferred from the selected beam sections to the adjacent beam sections are
 16
 17
 297 determined by Eq. (1).

$$298 \quad P = 2(N \sin \theta + V \cos \theta) \quad (1)$$

22
 23
 24
 299 where θ is the local rotation of the selected beam sections. At the BENM, θ can be approximately
 26
 27
 300 determined as $\theta = \arctan(4(D_l - D_{3l/4})/l)$; $D_{3l/4}$ is the vertical displacement measured at the position
 28
 29
 301 with $3l/4$ from the side column; D_l is the MCD; l is the beam span. At the BENS, θ can be
 31
 32
 302 approximately determined as $\theta = \arctan(4D_{l/4}/l)$, and $D_{l/4}$ is the vertical displacement measured at
 34
 35
 303 the position with $l/4$ from the side column.

37
 38
 304 As illustrated in Fig. 22, based on the force equilibrium along the beam axis and vertical direction,
 39
 40
 405 Eqs. (2) and (3) are obtained as follow

$$41 \quad N = F_L \sin \theta + (H_t + H_b) \cos \theta \quad (2)$$

$$42 \quad F_L = V \cos \theta + N \sin \theta \quad (3)$$

43
 44
 45
 46
 47
 307 where F_L is the measured vertical reaction beneath the side column; H_t and H_b are the measured
 48
 49
 50
 51
 308 horizontal reaction force of the top and bottom horizontal pin-pin restraint, respectively.

52
 53
 54
 55
 56
 310 Thus, for CL-series specimens, N and V of the selected sections are calculated by Eqs. (4) and
 57
 58
 591 (5), respectively.

312
$$N_{CL} = (F_L \tan \theta + H_t + H_b) \cos \theta \quad (4)$$

313
$$V_{CL} = (F_L - N_{CL} \sin \theta) / \cos \theta \quad (5)$$

314 Similarly, for SL-series specimens, N and V are calculated by Eqs. (6) and (7), respectively.

315
$$N_{SL} = ((F_L - G) \tan \theta + H_t + H_b) \cos \theta \quad (6)$$

316
$$V_{SL} = (F_L - G - N_{SL} \sin \theta) / \cos \theta \quad (7)$$

317 where G is the gravity load of the hanging weight between the selected section and the side
318 column.

319 For CL-series specimens, according to the locations of reactions as shown in Fig. 22, the bending
320 moment at BENM (M^M) and BENS (M^S) are calculated by Eqs. (8) and (9), respectively.

321
$$M_{CL}^M = F_L (l + 0.2) - H_t (D_l + 0.35) + H_b (D_l - 0.35) \quad (8)$$

322
$$M_{CL}^S = 0.2F_L - 0.35H_t + 0.35H_b \quad (9)$$

323 Similarly, the M^M and M^S of SL-series specimens are determined by Eqs. (10) and (11),
324 respectively.

325
$$M_{SL}^M = F_L (l + 0.2) - H_t (D_l + 0.35) + H_b (D_l - 0.35) - 0.75G_{l/4}l - 0.5G_{l/2}l - 0.25G_{3l/4}l \quad (10)$$

326
$$M_{SL}^S = 0.2F_L - 0.35H_t + 0.35H_b \quad (11)$$

327 The variations of the transferred vertical load from the selected sections (i.e., BENM and BENS)
328 of the specimens are shown in Figs. 23 to 28, respectively. **It is found that the axial force made a
329 negative contribution at the small deformation stage due to the second-order effect**, whereas it made a
330 positive contribution at the large deformation stage. As shown in Fig. 23(a), at the BENM of CL-13,
331 the shear force contribution decreased quickly after the CAA stage. As a result, the vertical component

332 of the axial force dominated the vertical load transfer at the large deformation stage. By contrast, at the
333 BENS of CL-13, the vertical projection of the shear force still kept increasing at the large deformation
334 stage since no rebar fractured there, as shown in Fig. 23(b), even though such contribution was smaller
335 than that from the axial force.

336 Fig. 24 shows that **the hanging weights induced initial shear force at the selected sections of SL-**
337 **13.** As illustrated in Fig. 24(a), the shear force contribution at the BENM kept almost constant during
338 the loading history until failure. However, as shown in Fig. 24(b), the shear force contribution at the
339 BENS began to decrease with the increase of the vertical displacement at the large deformation stage.
340 Moreover, at the CAA stage, the contribution of both shear and axial force of the BENS was much
341 greater than that of the BENM, indicating that the material strength of the BENS was used more
342 sufficiently than that of BENM. As shown in Figs. 25 to 28, similar results were found for the other
343 specimens. Therefore, loading regimes might draw different conclusions regarding the load transfer
344 mechanisms at different beam ends.

345 Fig. 29 illustrates the variation of bending moment at the beam ends. As shown in Fig. 29(a), the
346 bending moment at the beam ends of CL-13 decreased quickly after the stage of CAA. In comparison,
347 as shown in Fig. 29(b), the **decline** of bending moment for SL-13 was much milder. This is because
348 the material properties of the beams **can be more sufficiently mobilized under the SL.** However, as
349 shown in Figs. 29(c-f), such phenomenon became marginal with decreasing the span-to-depth ratio. As
350 illustrated in Fig. 30, the nature of CAA increasing the flexural resistance was the fact that bending
351 moment capacity of the beam sections was enhanced by considerable axial compression developed in
352 the beams through *M-N* interaction. Moreover, the measured *M-N* diagram agreed well with the
353 theoretical ones determined by Xtract [41].

354 4.4. Analytical model to evaluate CA capacity

355 Analytical models are proposed herein to evaluate the US of CL-series and SL-series specimens.
356 The US of SL-series specimens is attained at the first fracture of the beam top rebars at BENS. **As**
357 **shown in Figs. 16, 18, and 20, since the strain of beam bottom rebars was relatively small at the fracture**

358 of the top rebars, only top rebars were considered to provide the US. Therefore, for SL-series specimens,
359 the US is determined by Eq. (12).

$$360 \quad P_{CA} = 2f_u A_{st} \sin \varphi \quad (12)$$

361 where f_u and A_{st} are the ultimate strength and the area of top rebars, respectively; φ is the chord
362 rotation of the beam, as shown in Fig. 31(a).

363 For CL-series frames, as the bottom rebar at BENM fractured soon after the onset of CA. Thus,
364 similar to SL-series specimens, only beam top rebars were considered to provide the US. However, as
365 the bottom rebar fractured earlier, it is assumed that the direction of tensile force is along the line
366 between the top rebar at BENM and the middle of the section at BENS. As shown in Fig. 31(b), the
367 rotation α is determined as the angle between the action line of the tensile force and the horizontal
368 line. Therefore, the US of CL-series specimens is given by

$$369 \quad P_{CA} = 2f_u A_{st} \sin \alpha \quad (13)$$

370 As shown in Fig. 5, the results from the proposed CA models agreed well with the measured ones.
371 Therefore, the proposed models can be used for evaluating the US of CL/SL-series specimens. It should
372 be noted that practical design will benefit from an allowed rotation of the beams to develop CA.
373 However, the deformation capacity of the beams can not be determined in this study due to the limited
374 number of specimens. As the rotation capacity is affected by material properties of concrete and steel
375 reinforcement, geometric properties of beam sections and reinforcement detailing, etc., more tests
376 should be conducted to fill this gap. Although the proposed models can not be used for design directly,
377 the methods are reasonable to predict CA capacity with given rotations of the beams and the area of
378 contributing rebars. Thus, the methodology herein can be implemented for design with further study,
379 in particular, quantifying the allowed rotation capacity of the beam segments.

380 5. Conclusions

381 Based on experimental and analytical results, the conclusions are drawn as below:

- 382 1. Experimental results demonstrated that the simplified concentrated loading (CL) regime may
383 mistakenly identify the failure mode of reinforced concrete (RC) beam-column sub-assemblages

384 **under a middle column removal scenario.** For the specimens tested with the CL regime, the first
385 rebar fracture occurred at the bottom rebar near the middle column. For the specimens subjected
386 to sequential loading (SL) regime, the first rebar fracture occurred at the top rebar near the side
387 column.

388 2. The tests with the CL regime could accurately predict the yield strength and the first peak strength
389 (or termed as compressive arch action capacity) of **the specimens**. However, the CL regime may
390 significantly over-estimate the deformation capacity and ultimate strength (or catenary action
391 capacity) of **the specimens**, resulting in unsafe design in practice.

392 3. The span-to-depth ratio significantly affected the yield strength, first peak strength, ultimate
393 strength, and ultimate deformation capacity **of the specimens**. However, the span-to-depth ratio
394 may not greatly change the chord rotation capacity **of the beams**.

395 4. As the material properties of the beam can be used more sufficiently, the decrease of flexural action
396 capacity in SL-series specimens was milder than that in CL-series specimens. The catenary action
397 capacity of CL/SL-series specimens was controlled by the beam top rebars. Due to different failure
398 modes, catenary action models were separately proposed for CL/SL-series specimens with
399 reasonable accuracy.

400 **Future work**

401 Upon the test results, the limitation of the current study and future research needed are highlighted.
402 The effects of the loading regime on seismically designed specimens should be evaluated in the future
403 as the conclusions of non-seismically designed specimens may not be suitable for seismically designed
404 ones. The effects of parameters that are not involved in this study on the deformation capacity of RC
405 specimens subjected to the SL regime should be investigated. The reliability of the proposed models
406 should be further validated by more tests. Furthermore, the effects of boundary conditions need to be
407 quantified by numerical studies.

408 **Acknowledgements**

409 The authors gratefully acknowledge the financial support provided by the National Natural
410 Science Foundation of China (Nos. 52022024, 51778153).

411 **References**

- 412 [1] American Society of Civil Engineers (ASCE). Minimum design loads for buildings and other
413 structures, ASCE 7-10. Reston, VA: American Society of Civil Engineers; 2010.
414 [2] General Services Administration (GSA). Progressive collapse analysis and design guidelines for
415 new federal office buildings and major modernization projects, Washington, DC; 2009.
416 [3] Department of Defense (DoD). Design of building to resist progressive collapse. Unified facility
417 criteria, UFC 4-023-03, Washington, DC; 2009.
418 [4] Fu F. Structural analysis and design to prevent disproportionate collapse. CRC Press; 2016.
419 [5] Fu F. Design and analysis of tall and complex structures. Elsevier; 2018.
420 [6] ACI Committee 318, Building Code Requirements for Structural Concrete (ACI 318-14) and
421 Commentary (318R-14). American Concrete Institute, Farmington Hills, MI, 433 pp; 2014.
422 [7] Sasani M, Bazan M, Sagioglu S. Experimental and analytical progressive collapse evaluation of
423 actual reinforced concrete structure. ACI Struct J 2007; 104(6):731–9.
424 [8] Sheffield C, Audrey K, Hoon VNP. An instrumented full-scale building disproportionate collapse
425 test. Proceedings of 14th international symposium on interaction of the effects of munitions with
426 structures 2011. Seattle, Washington; 2011.
427 [9] Yu J, Rinder T, Stolz A, Tan KH, Riedel W. Dynamic progressive collapse of an RC assemblage
428 induced by contact detonation. J Struct Eng 2014; 140(6):04014014.
429 [10] Qian K, Li B. Dynamic performance of RC beam-column substructures under the scenario of the
430 loss of a corner column—Experimental results. Eng Struct 2012; 42:154-67.
431 [11] Peng ZH, Orton SL, Liu JR, Tian Y. Experimental study of dynamic disproportionate collapse in
432 flat-plate buildings subjected to exterior column removal. J Struct Eng 2017; 143(9): 04017125.
433 [12] Qian K, Liang SL, Xiong XY, Fu F, Fang Q. Quasi-static and dynamic behavior of precast concrete
434 frames with high performance dry connections subjected to loss of a penultimate column scenario.
435 Eng Struct 2020; 205:110115.
436 [13] Yi WJ, He QF, Xiao Y, Kunnath SK. Experimental study on disproportionate collapse-resistant
437 behavior of reinforced concrete frame structures. ACI Struct J 2008; 105(4): 433-439.

- 438 [14] Su YP, Tian Y, Song XS. Progressive collapse resistance of axially-restrained frame beams. ACI
439 Struct J 2009; 106(5):600–7.
- 440 [15] FarhangVesali N, Valipour H, Samali B, Foster S. Development of arching action in
441 longitudinally-restrained reinforced concrete beams. Construction and Building Materials 2013;
442 47: 7-19.
- 443 [16] Qian K, Li B. Performance of three-dimensional reinforced concrete beam-column substructures
444 under loss of a corner column scenario. J Struct Eng 2013; 139(4):584-94.
- 445 [17] Yu J, Tan KH. Experimental and numerical investigation on progressive collapse resistance of
446 reinforced concrete beam-column sub-assemblages. Eng Struct 2013; 55: 90–106.
- 447 [18] Yu J, Tan KH. Structural behavior of reinforced concrete beam-column sub-assemblages under a
448 middle column removal scenario. J Struct Eng 2013; 139(2):233-50.
- 449 [19] Lew HS, Main JA, Robert SD, Sadek F. Performance of steel moment connections under a column
450 removal scenario. I: Experiments. J Struct Eng 2013; 139(1): 98-107.
- 451 [20] Lew HS, Bao YH, Pujol S, Sozen MA. Experimental study of reinforced concrete assemblies under
452 column removal scenario. ACI Struct J 2014; 111(4): 881-892.
- 453 [21] Qian K, Li B, Ma JX. Load-carrying mechanism to resist disproportionate collapse of RC
454 buildings. J Struct Eng 2015; 141(2): 04014107.
- 455 [22] Wang W, Fang CF, Qin X, Chen YY, Li L. Performance of practical beam-to-SHS column
456 connections against progressive collapse. Eng Struct 2016; 106: 332–347.
- 457 [23] Ren PQ, Li Y, Lu XZ, Guan H, Zhou YL. Experimental investigation of progressive collapse
458 resistance of one-way reinforced concrete beam-slab substructures under a middle-column-
459 removal scenario. Eng Struct 2016; 118: 28–40.
- 460 [24] Lu XZ, Lin KQ, Li Y, Guan H, Ren PQ, Zhou YL. Experimental investigation of RC beam-slab
461 substructures against disproportionate collapse subject to an edge-column removal scenario. Eng
462 Struct 2017; 149: 91-103.
- 463 [25] Qian K, Li B. Effects of masonry infill wall on the performance of RC frames to resist
464 disproportionate collapse. J Struct Eng 2017; 143(9): 04017118.

- 465 [26] Yu J, Tan KH. Structural behavior of reinforced concrete frames subjected to progressive collapse.
466 ACI Struct J 2017; 114(1): 63-74.
- 467 [27] Wang F, Yang J, Nyunn S, Azim I. Effect of concrete infill walls on the progressive collapse
468 performance of precast concrete framed substructures. Journal of Building Engineering 2020; in
469 press.
- 470 [28] Weng YH, Qian K, Fu F, Fang Q. Numerical investigation on load redistribution capacity of flat
471 slab substructures to resist progressive collapse. Journal of Building Engineering 2020; 29:
472 101109.
- 473 [29] Theodor Krauthammer T, Koha YH. Exploring numerical approaches for pre-test progressive
474 collapse assessment of RC frame structures. Engineering Structures 2019; 201: 109776.
- 475 [30] Yu J, Luo L, Li Y. Numerical study of progressive collapse resistance of RC beam-slab
476 substructures under perimeter column removal scenarios. Eng Struct 2018; 159: 14–27.
- 477 [31] Pham AT, Tan KH, Yu J. Numerical investigations on static and dynamic responses of reinforced
478 concrete sub-assemblages under progressive collapse. Eng Struct 2017; 149: 2–20.
- 479 [32] Liu M. A new dynamic increase factor for nonlinear static alternate path analysis of building
480 frames against progressive collapse. Engineering Structures 2013; 48: 666–673.
- 481 [33] Pham AT, Lim NS, Tan KH. Investigations of tensile membrane action in beam-slab systems under
482 progressive collapse subject to different loading configurations and boundary conditions.
483 Engineering Structures 2017;150: 520–536.
- 484 [34] Ferraioli M. A modal pushdown procedure for progressive collapse analysis of steel frame
485 structures. Journal of Constructional Steel Research 2019; 156: 227–241.
- 486 [35] Ding L, Coile RV, Botte W, Caspeepe R. Quantification of model uncertainties of the energy-based
487 method for dynamic column removal scenarios. Engineering Structures 2021; 237: 112057.
- 488 [36] Brunesi E, Parisi F. Progressive collapse fragility models of European reinforced concrete framed
489 buildings based on pushdown analysis. Engineering Structures 2017; 152: 579–596.

- 490 [37] Qian K, Weng YH, Fu F, Deng XF. Numerical evaluation of the reliability of using single-story
491 substructures to study progressive collapse behaviour of multi-story RC frames. Journal of
492 Building Engineering 2021; 33: 101636.
- 493 [38] Qian K, Liang SL, Fu F, Li Y. Progressive collapse resistance of emulative precast concrete frames
494 with various reinforcing details. Journal of Structural Engineering 2021; 147(8): 04021107.
- 495 [39] Deng XF, Liang SL, Fu F, Qian K. Effects of high-strength concrete on progressive collapse
496 resistance of reinforced concrete frame. ASCE Journal of Structural Engineering 2020; 146(6):
497 04020078.
- 498 [40] Qian K, Li B. Investigation into resilience of precast concrete floors against progressive collapse.
499 ACI Structural Journal 2019; 116(2):171-182.
- 500 [41] Chadwell CA, Imbsen R. Xtract-Cross Section Analysis software for Structural and Earthquake
501 Engineering.

Table 1-Specimen properties

Test ID	Beam clear span (mm)	Beam longitudinal reinforcement				Loading regime
		A-A section		B-B section		
		Top	Bottom	Top	Bottom	
CL-13	3250	3T12	2T12	2T12	2T12	Concentrated loading
SL-13	3250	3T12	2T12	2T12	2T12	Sequential loading
CL-11	2750	3T12	2T12	2T12	2T12	Concentrated loading
SL-11	2750	3T12	2T12	2T12	2T12	Sequential loading
CL-8	2000	3T12	2T12	2T12	2T12	Concentrated loading
SL-8	2000	3T12	2T12	2T12	2T12	Sequential loading

Table 2-Material properties of reinforcements

Items	Nominal diameter (mm)	Yield strength (MPa)	Ultimate strength (MPa)	Elongation (%)
Longitudinal rebar	T12	438	577	16.6
Transverse links	R6	348	486	25.4

Note: R6 represents plain bar with diameter of 6 mm; T12 represents deformed rebar with diameter of 12 mm.

Table 3-Test results

Test ID	Critical displacements (mm)			Critical loads (kN)			MHCF (kN)	MHTF (kN)	UR (rad)	Lateral stiffness (kN/m)
	YS	FPS	US	YS	FPS	US				
CL-13	45	108	731	33	43	81+	-153	148	0.23	1.0×10^5
SL-13-Shift	43	100	550	31	39	63	-154	111	0.17	
CL-11	36	90	712	37	52	94	-178	154	0.26	
SL-11-Shift	35	90	593	36	49	85	-167	167	0.22	
CL-8	25	79	551	53	77	88	-202	147	0.28	
SL-8-Shift	23	80	357	54	74	63	-224	110	0.18	

Note: YS means yield strength; FPS represents first peak strength; US represents ultimate strength; MHCF means maximum horizontal compressive force; MHTF means maximum horizontal tensile force; and UR indicates ultimate rotation.

List of Figures

Fig. 1. Loading regimes for disproportionate collapse studies: (a) dynamic loading regime; (b) concentrated loading regime; (c) sequential loading regime

Fig. 2. Dimension and reinforcement details of Specimens: (a) CL-13/SL-13; (b) CL-11/SL-11; (c) CL-8/SL-8; (d) cross-section (Note: Unit in mm)

Fig. 3. Test setup for the concentrated loading regime: (a) picture; (b) schematic diagram

Fig. 4. Test setup for the sequential loading regime: (a) picture; (b) schematic diagram

Fig. 5. Comparison of load-displacement curves: (a) CL-13&SL-13; (b) CL-11&SL-11; (c) CL-8&SL-8

Fig. 6. Crack pattern development: (a) CL-13; (b) SL-13; (c) CL-11; (d) SL-11; (e) CL-8; (f) SL-8

Fig. 7. Failure mode and crack pattern of Specimen CL-13

Fig. 8. Failure mode and crack pattern of Specimen SL-13

Fig. 9. Failure mode and crack pattern of Specimen CL-11

Fig. 10. Failure mode and crack pattern of Specimen SL-11

Fig. 11. Failure mode and crack pattern of Specimen CL-8

Fig. 12. Failure mode and crack pattern of Specimen SL-8

Fig. 13. Comparison of horizontal reaction force-displacement curves: (a) CL-13&SL-13; (b) CL-11&SL-11; (c) CL-8&SL-8

Fig. 14. Deflection shape of the beams at various stages: (a) CL-13; (b) SL-13; (c) CL-11; (d) SL-11; (e) CL-8; (f) SL-8

Fig. 15. Strain gauge results of CL-13: (a) close to side column; (b) close to middle column

Fig. 16. Strain gauge results of SL-13: (a) close to side column; (b) close to middle column

Fig. 17. Strain gauge results of CL-11: (a) close to side column; (b) close to middle column

Fig. 18. Strain gauge results of SL-11: (a) close to side column; (b) close to middle column

Fig. 19. Strain gauge results of CL-8: (a) close to side column; (b) close to middle column

Fig. 20. Strain gauge results of SL-8: (a) close to side column; (b) close to middle column

Fig. 21. Effect of early rebar fracture on catenary action: (a) before rebar fracture; (b) fracture of beam bottom rebar at BENM; (c) fracture of beam top rebar at BENS

Fig. 22. Determination of load transfer mechanism at selected beam section: (a) CL-series; (b) SL-series

Fig. 23. Load transfer mechanisms at different beam sections of CL-13: (a) BENM; (b) BENS

Fig. 24. Load transfer mechanisms at different beam sections of SL-13: (a) BENM; (b) BENS

Fig. 25. Load transfer mechanisms at different beam sections of CL-11: (a) BENM; (b) BENS

Fig. 26. Load transfer mechanisms at different beam sections of SL-11: (a) BENM; (b) BENS

Fig. 27. Load transfer mechanisms at different beam sections of CL-8: (a) BENM; (b) BENS

Fig. 28. Load transfer mechanisms at different beam sections of SL-8: (a) BENM; (b) BENS

Fig. 29. Relationship of bending moment v.s. deflection at different cross-sections: (a) CL-13; (b) SL-13; (c) CL-11; (d) SL-11; (e) CL-8; (f) SL-8

Fig. 30. M-N diagram at BENM: (a) CL-13; (b) SL-13; (c) CL-11; (d) SL-11; (e) CL-8; (f) SL-8

Fig. 31. Definition of the rotation of φ and α for SL-series and CL-series specimens: (a) φ for SL-series; (b) α for CL-series

1
2
3
4
5
6
7
8
9
10
11
12
13
14
15
16
17
18
19
20
21
22
23
24
25
26
27
28
29
30
31
32
33
34
35
36
37
38
39
40
41
42
43
44
45
46
47
48
49
50
51
52
53
54
55
56
57
58
59
60
61
62
63
64
65

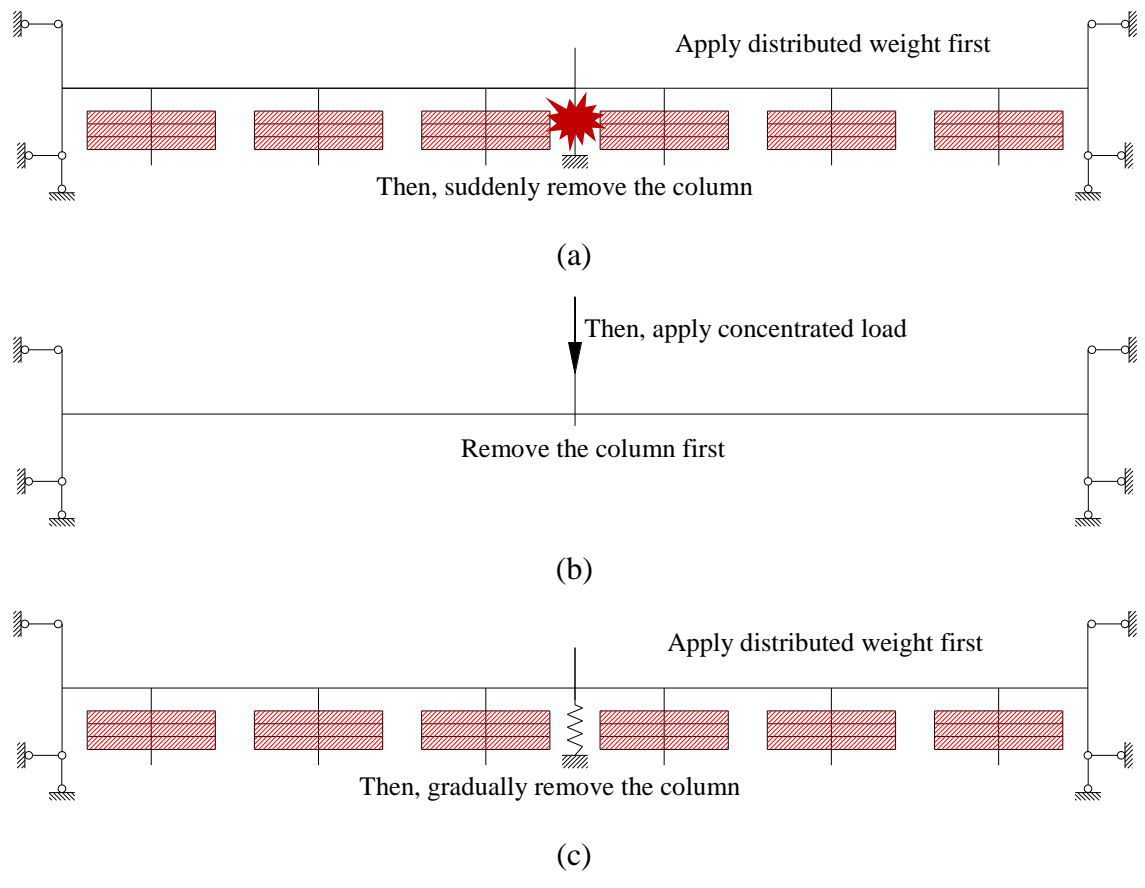
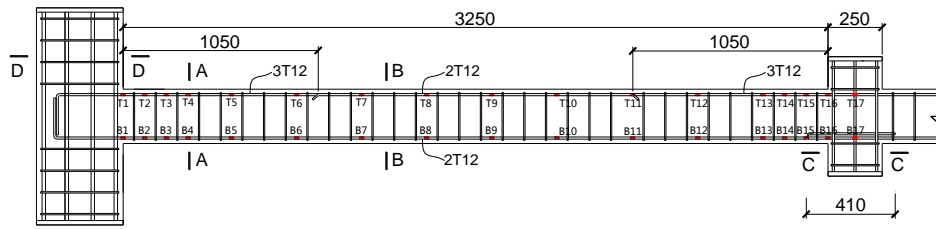
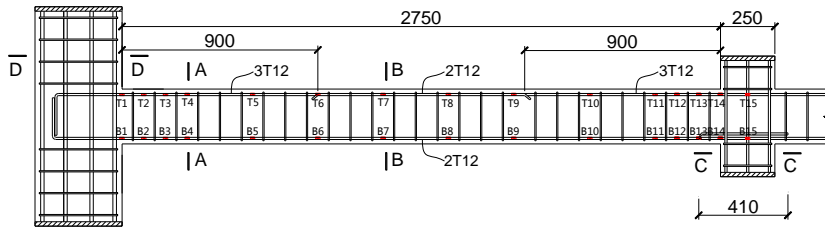


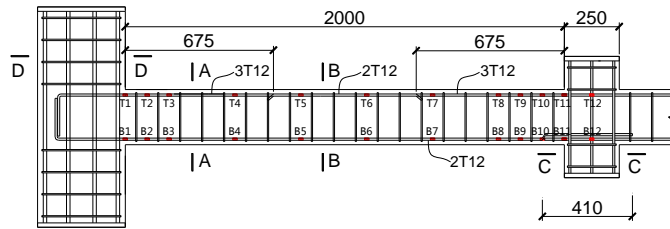
Fig. 1. Loading regimes for disproportionate collapse studies: (a) dynamic loading regime; (b) concentrated loading regime; (c) sequential loading regime



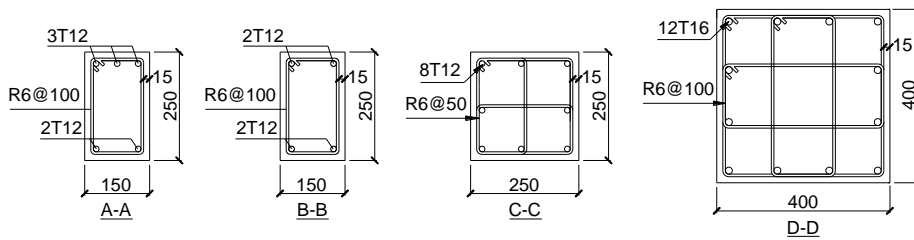
(a)



(b)

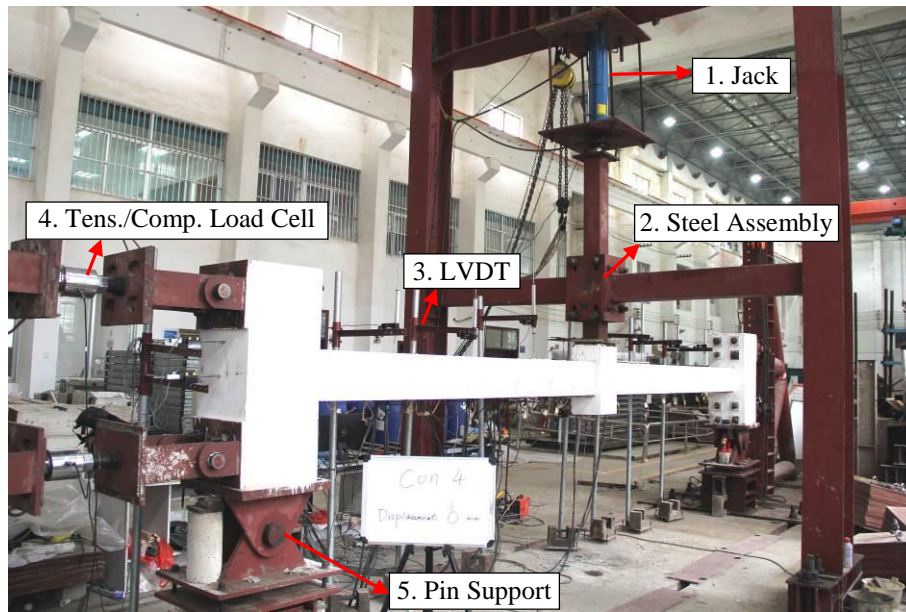


(c)

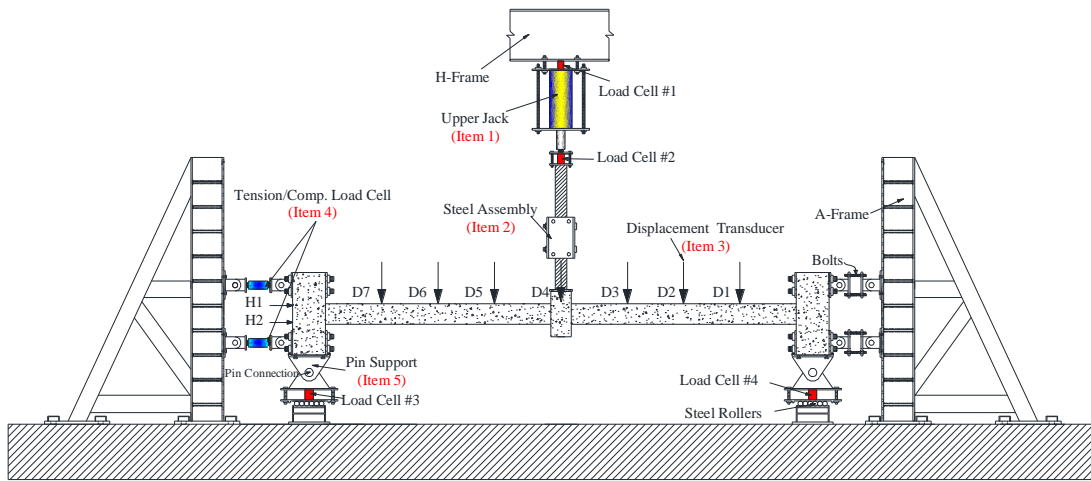


(d)

Fig. 2. Dimension and reinforcement detailing of specimens: (a) CL/SL-13-13; (b) CL/SL-11; (c) CL/SL-8; (d) cross-section (Unit: mm)

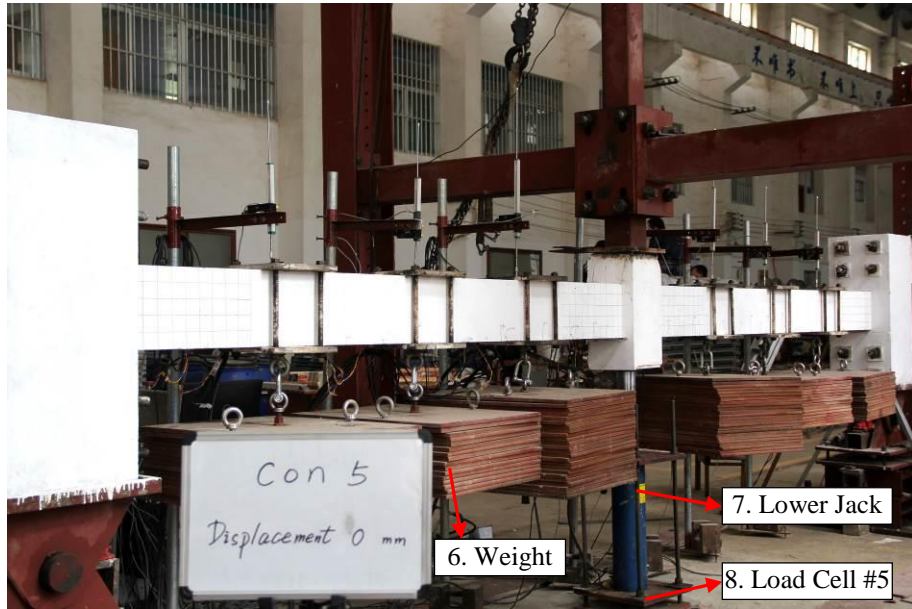


(a)

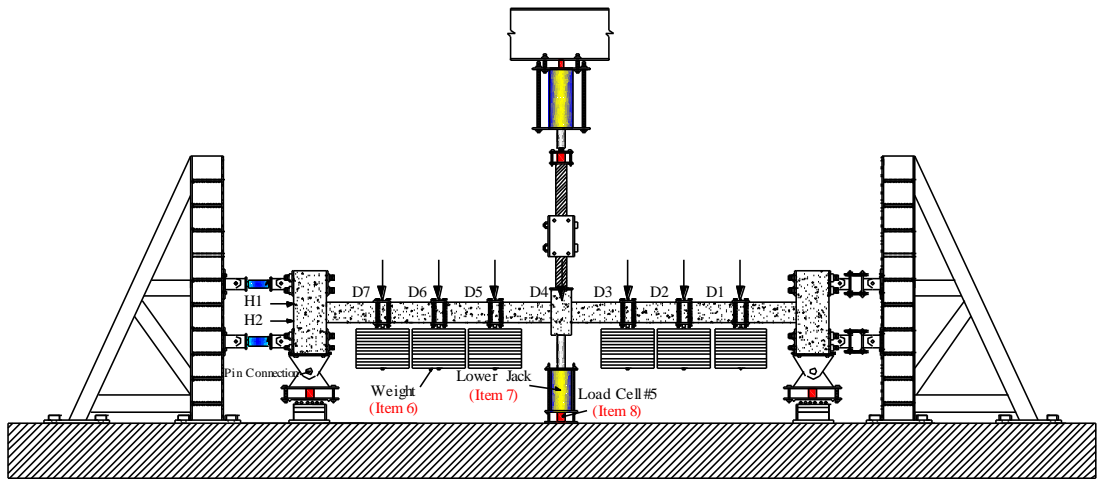


(b)

Fig. 3. Test setup for the concentrated loading regime: (a) picture; (b) schematic diagram



(a)



(b)

Fig. 4. Test setup for the sequential loading regime: (a) picture; (b) schematic diagram

1
2
3
4
5
6
7
8
9
10
11
12
13
14
15
16
17
18
19
20
21
22
23
24
25
26
27
28
29
30
31
32
33
34
35
36
37
38
39
40
41
42
43
44
45
46
47
48
49
50
51
52
53
54
55
56
57
58
59
60
61
62
63
64
65

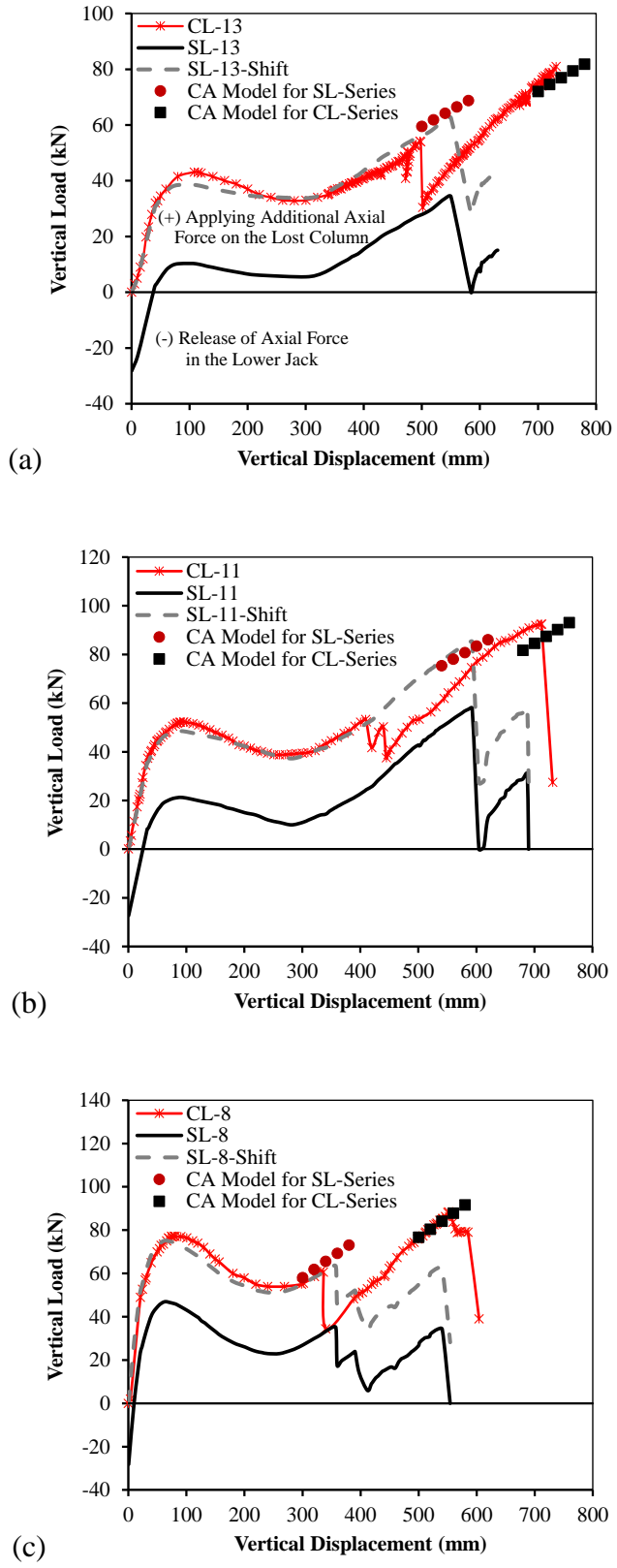
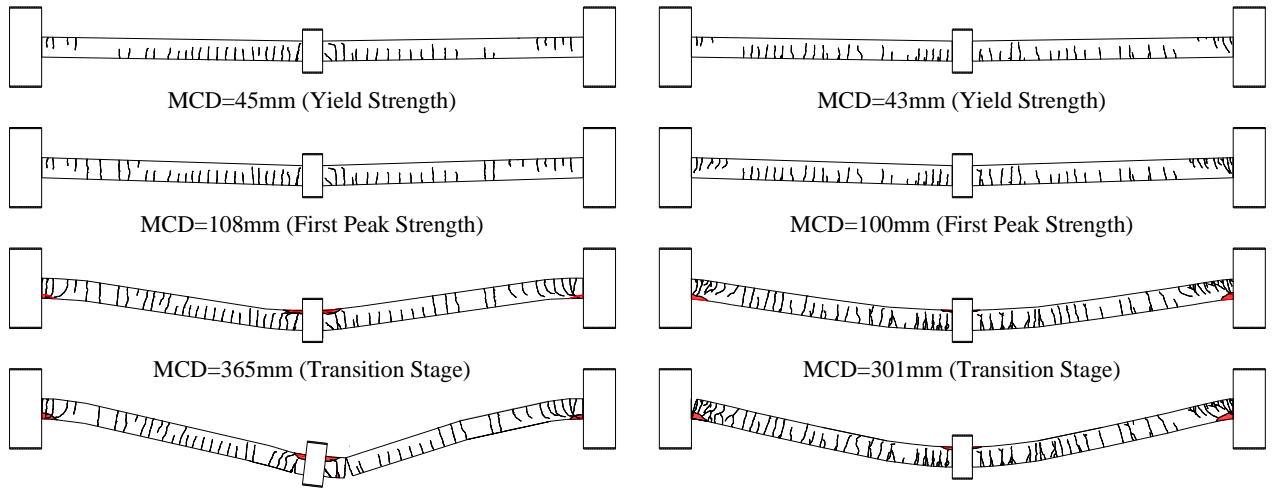
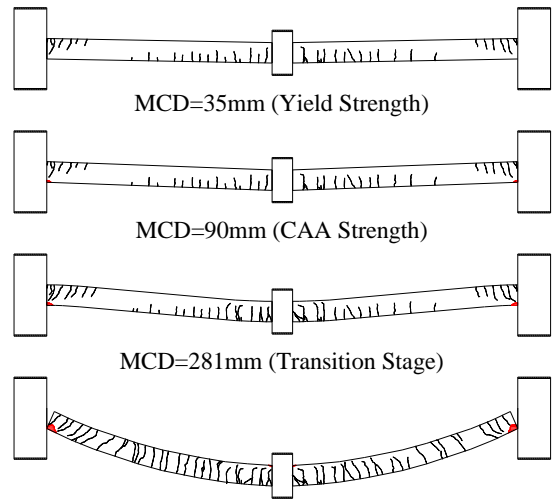
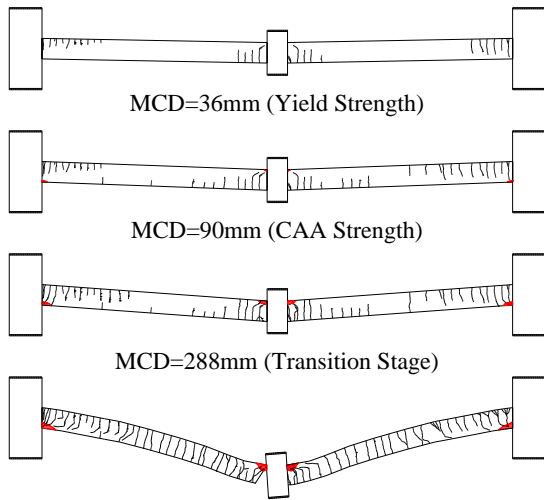


Fig. 5. Comparison of load-displacement curves: (a) CL-13&SL-13; (b) CL-11&SL-11; (c) CL-8&SL-8



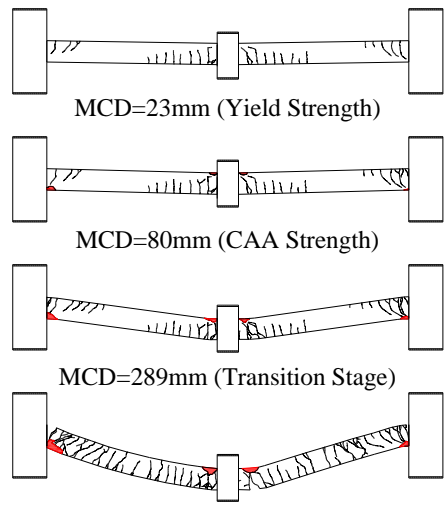
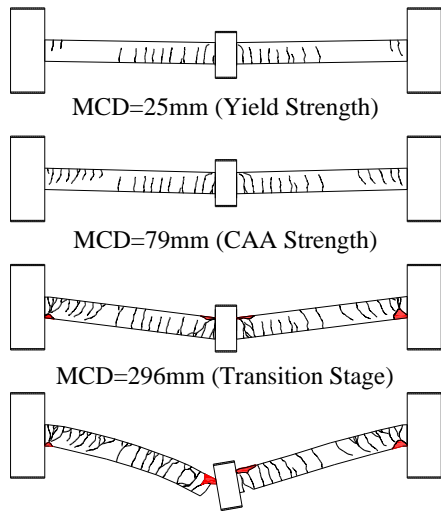
(a)

(b)



(c)

(d)



(e)

(f)

Fig. 6. Crack pattern development: (a) CL-13; (b) SL-13; (c) CL-11; (d) SL-11; (e) CL-8; (f)

SL-8

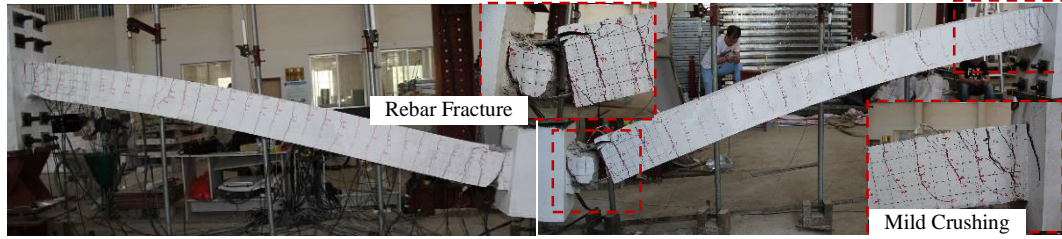


Fig. 7. Failure mode of specimen CL-13



Fig. 8. Failure mode and crack pattern of specimen SL-13



Fig. 9. Failure mode and crack pattern of specimen CL-11

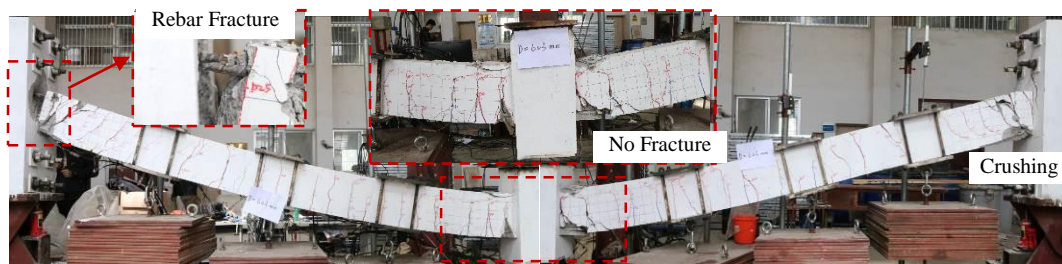


Fig. 10. Failure mode and crack pattern of specimen SL-11

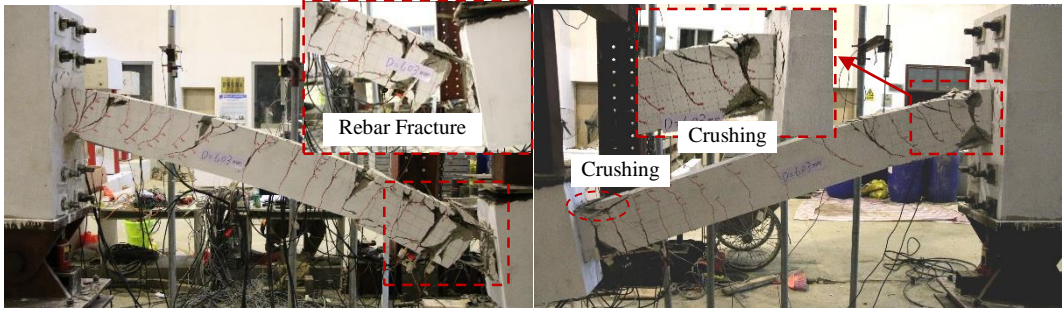


Fig. 11. Failure mode and crack pattern of specimen CL-8

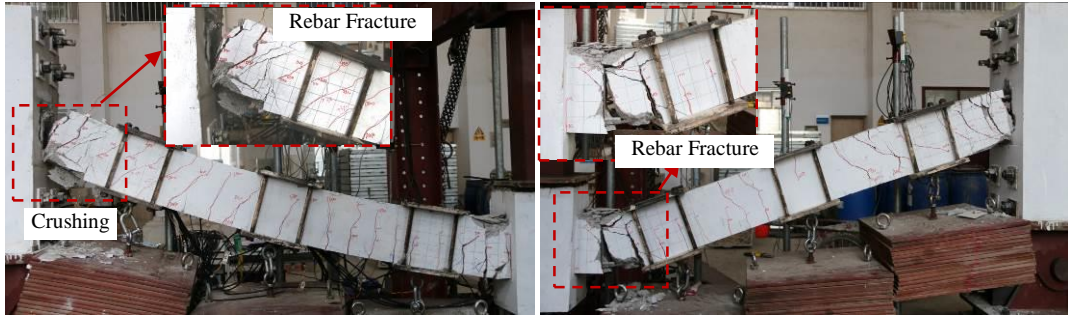


Fig. 12. Failure mode and crack pattern of specimen SL-8

1
2
3
4
5
6
7
8
9
10
11
12
13
14
15
16
17
18
19
20
21
22
23
24
25
26
27
28
29
30
31
32
33
34
35
36
37
38
39
40
41
42
43
44
45
46
47
48
49
50
51
52
53
54
55
56
57
58
59
60
61
62
63
64
65

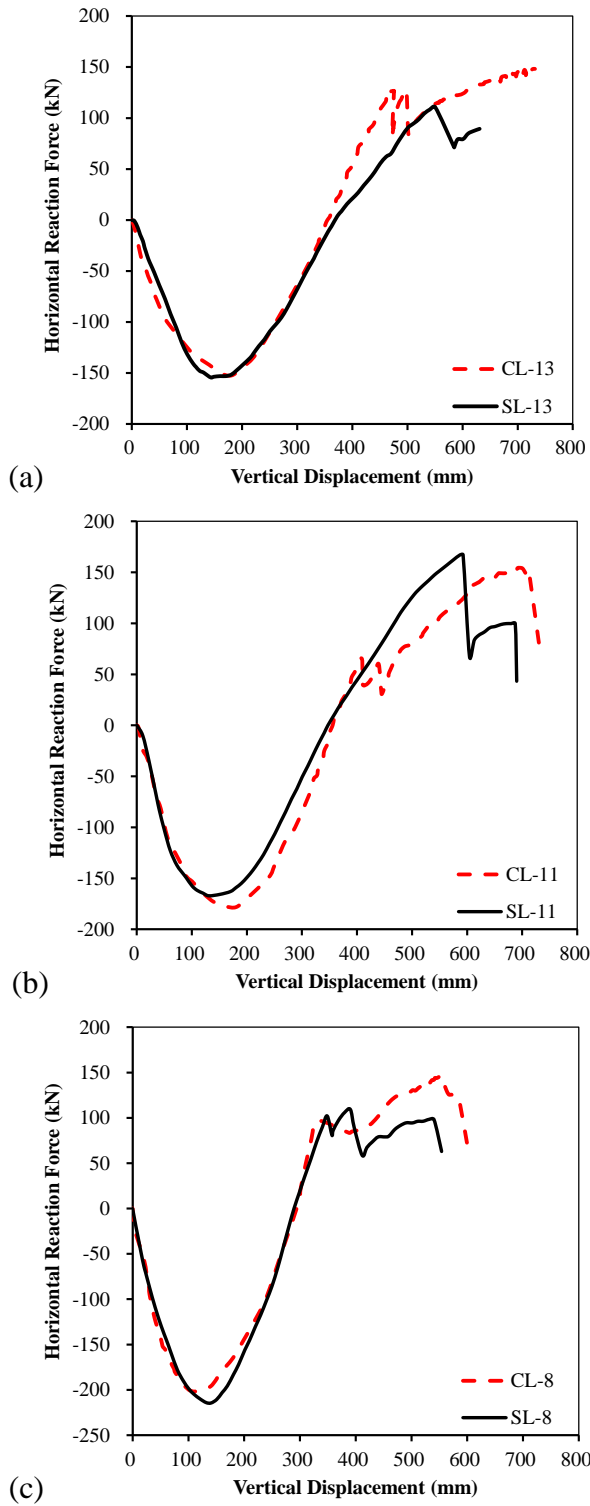


Fig. 13. Comparison of horizontal reaction force-displacement curves: (a) CL-13&SL-13; (b) CL-11&SL-11; (c) CL-8&SL-8

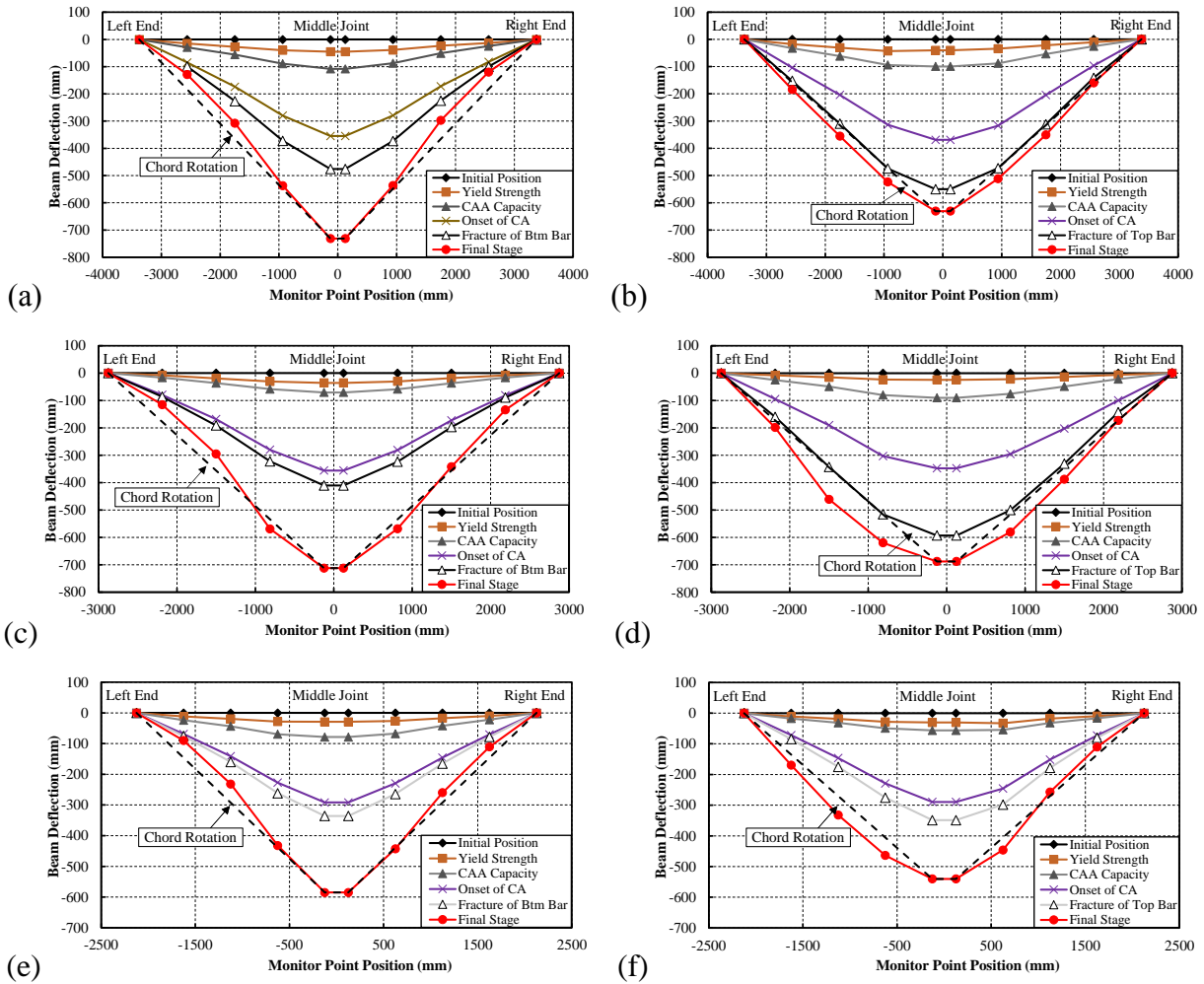


Fig. 14. Deflection shape of the beams at various stages: (a) CL-13; (b) SL-13; (c) CL-11; (d) SL-11; (e) CL-8; (f) SL-8

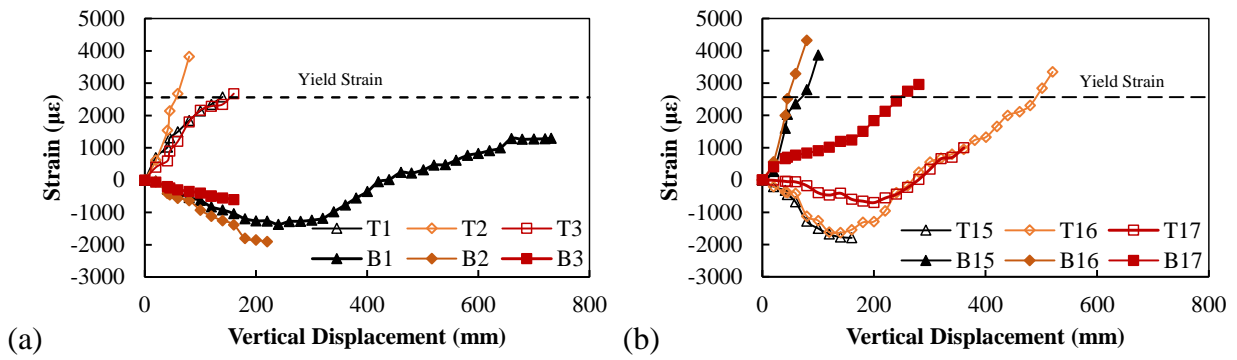


Fig. 15. Strain gauge results of CL-13: (a) close to side column; (b) close to middle column

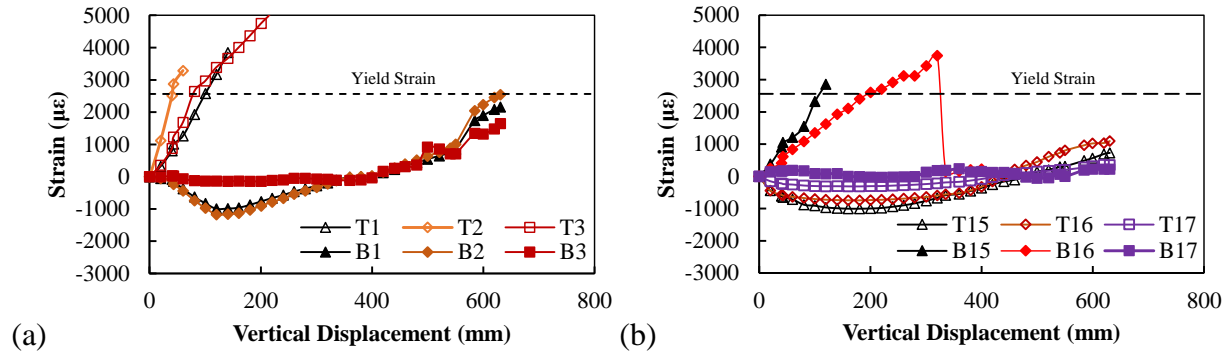


Fig. 16. Strain gauge results of SL-13: (a) close to side column; (b) close to middle column

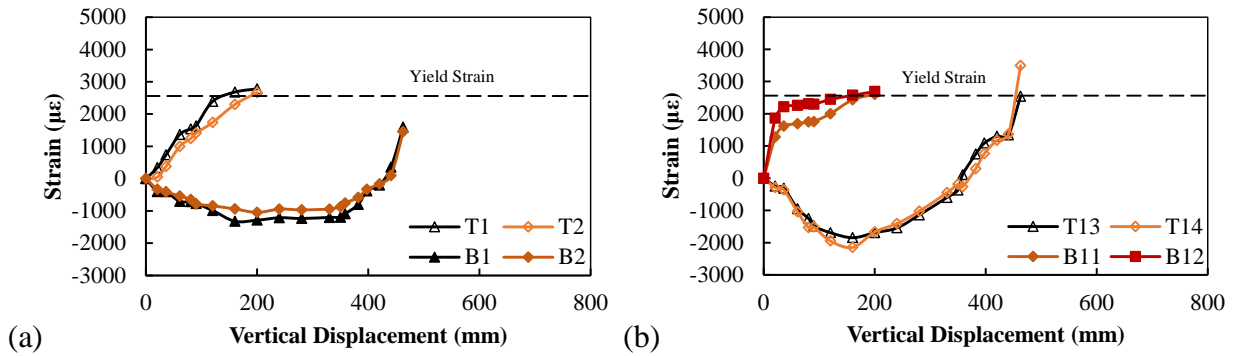


Fig. 17. Strain gauge results of CL-11: (a) close to side column; (b) close to middle column

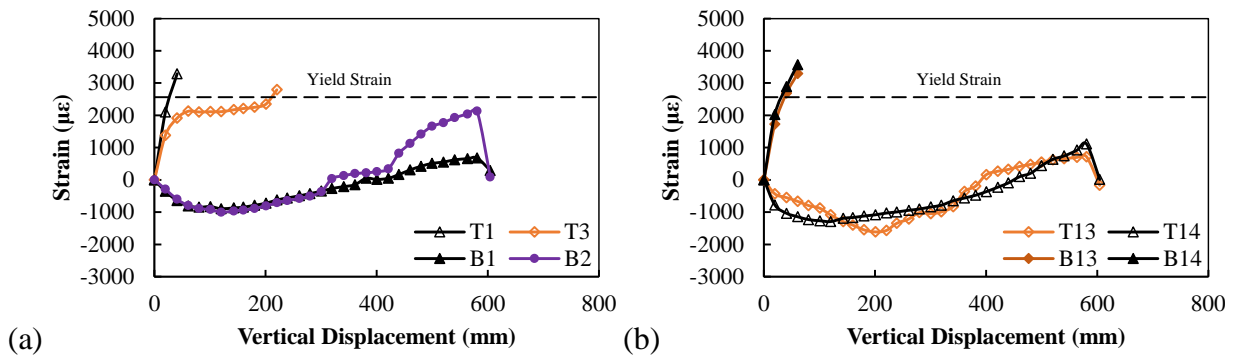


Fig. 18. Strain gauge results of SL-11: (a) close to side column; (b) close to middle column

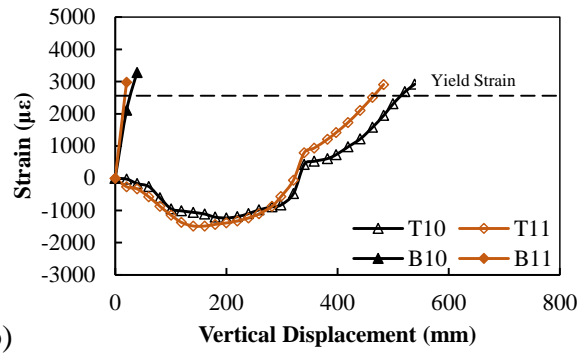
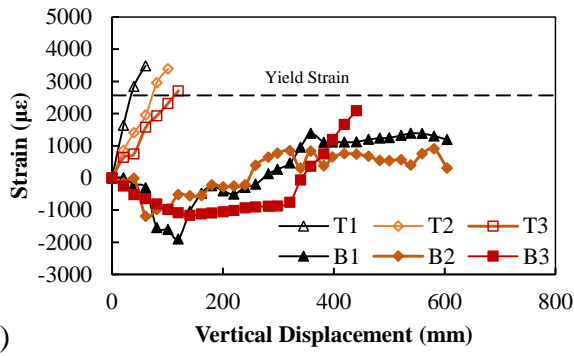


Fig. 19. Strain gauge results of CL-8: (a) close to side column; (b) close to middle column

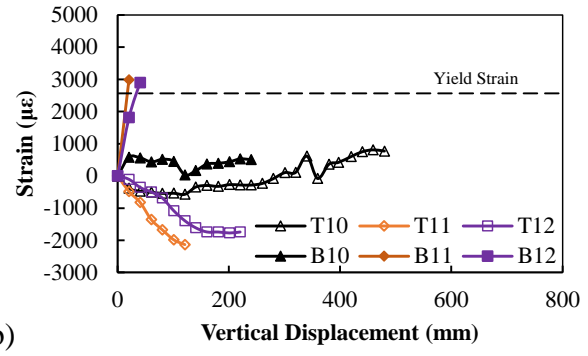
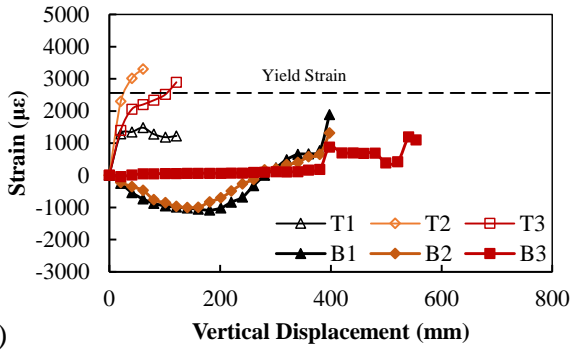


Fig. 20. Strain gauge results of SL-8: (a) close to side column; (b) close to middle column

1
2
3
4
5
6
7
8
9
10
11
12
13
14
15
16
17
18
19
20
21
22
23
24
25
26
27
28
29
30
31
32
33
34
35
36
37
38
39
40
41
42
43
44
45
46
47
48
49
50
51
52
53
54
55
56
57
58
59
60
61
62
63
64
65

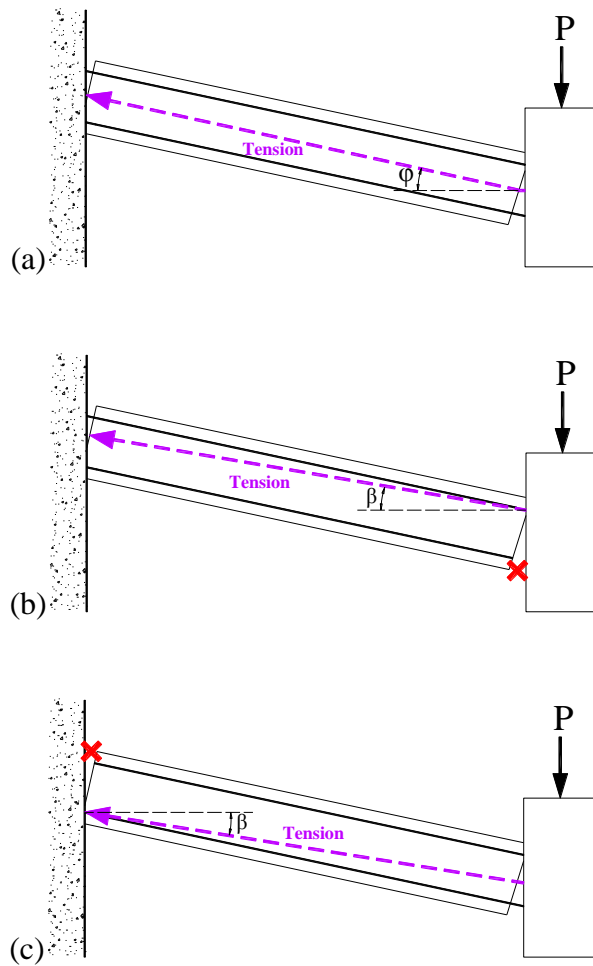


Fig. 21. Effect of early rebar fracture on catenary action: (a) before rebar fracture; (b) fracture of beam bottom rebar at BENM; (c) fracture of beam top rebar at BENS

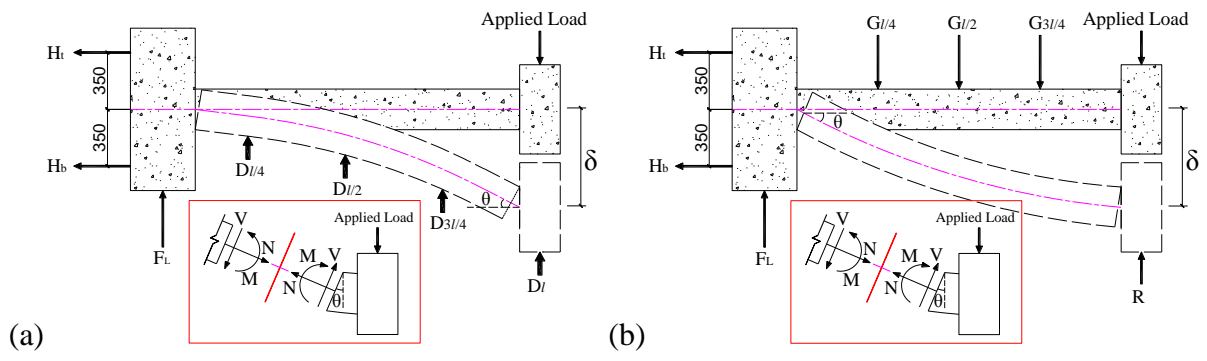


Fig. 22. Determination of load transfer mechanisms at selected beam section: (a) CL-series; (b) SL-series

1
2
3
4
5
6
7
8
9
10
11
12
13
14
15
16
17
18
19
20
21
22
23
24
25
26
27
28
29
30
31
32
33
34
35
36
37
38
39
40
41
42
43
44
45
46
47
48
49
50
51
52
53
54
55
56
57
58
59
60
61
62
63
64
65

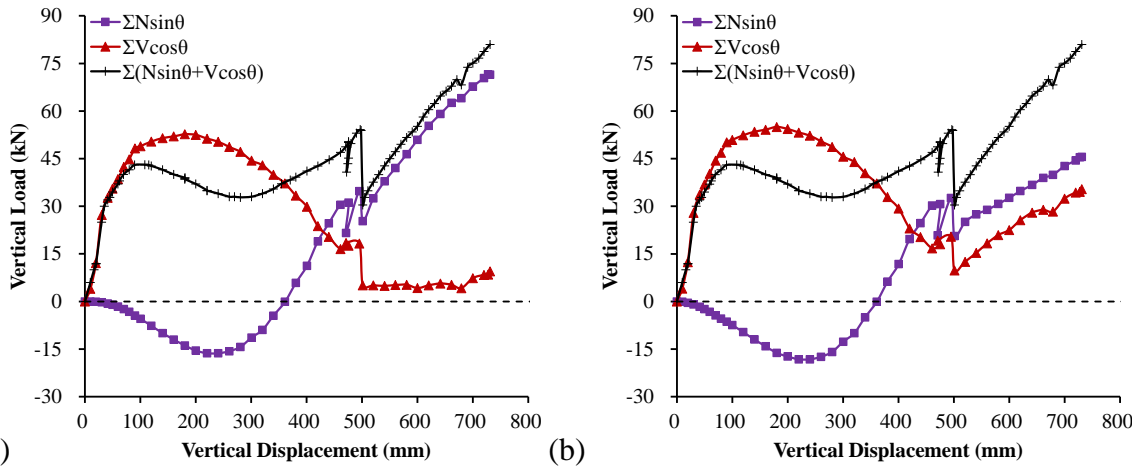


Fig. 23. Load transfer mechanisms at different beam sections of CL-13: (a) BENM; (b) BENS

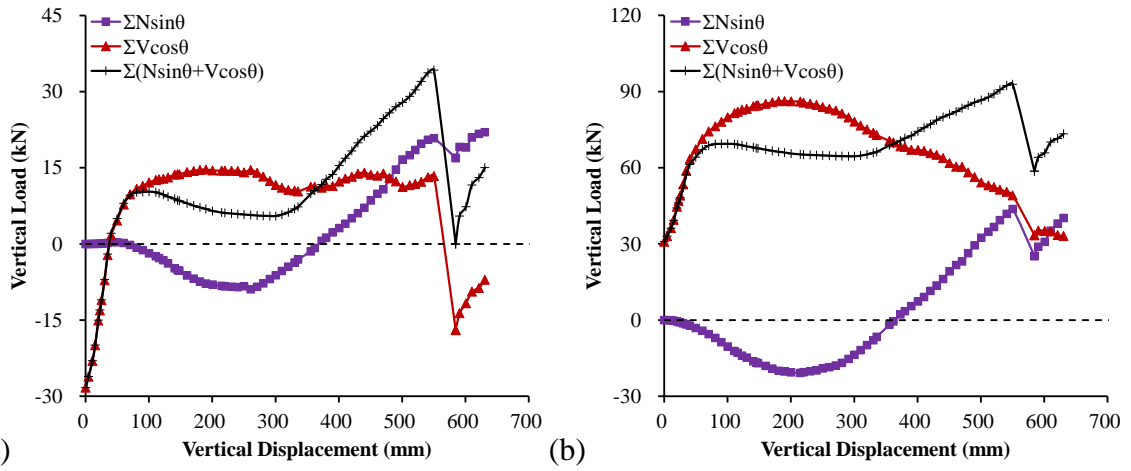


Fig. 24. Load transfer mechanisms at different beam sections of SL-13: (a) BENM; (b) BENS

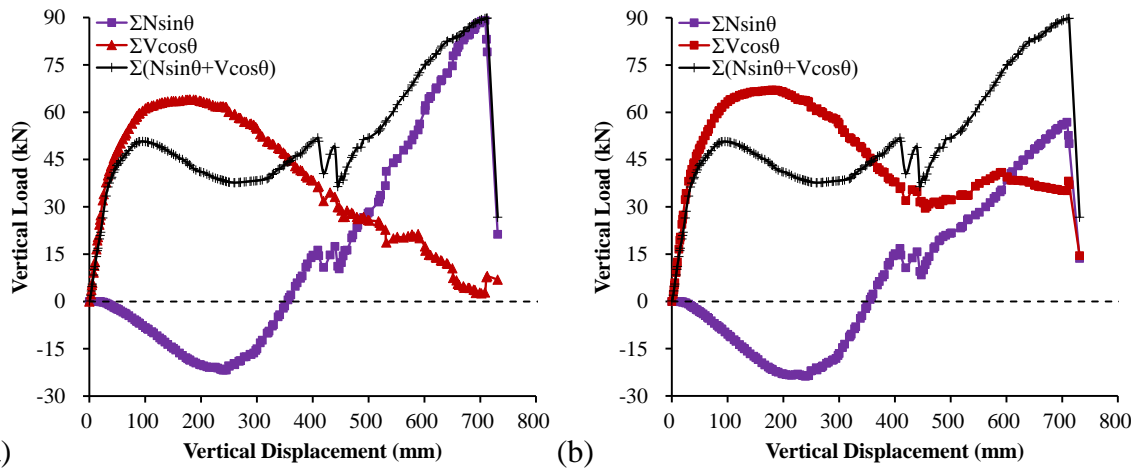


Fig. 25. Load transfer mechanisms at different beam sections of CL-11: (a) BENM; (b) BENS

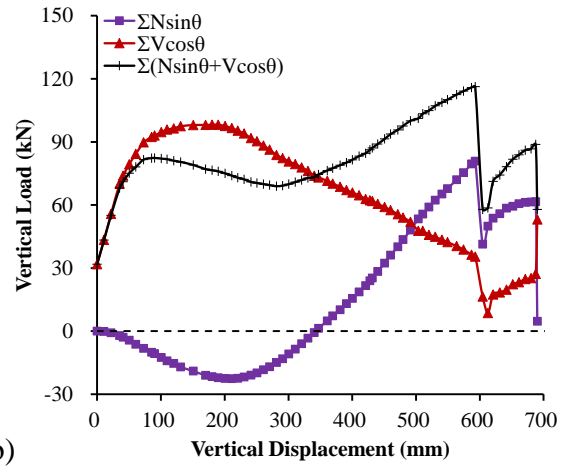
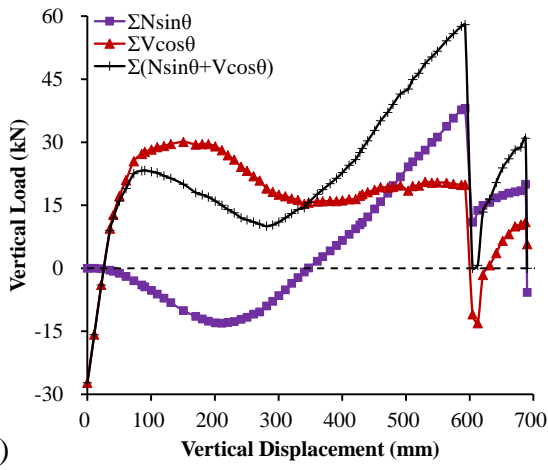


Fig. 26. Load transfer mechanisms at different beam sections of SL-11: (a) BENM; (b) BENS

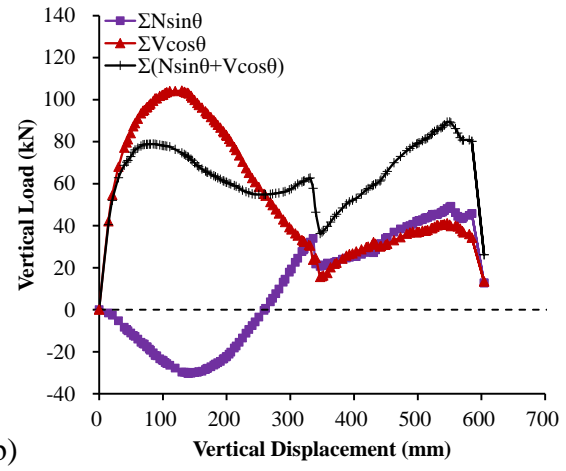
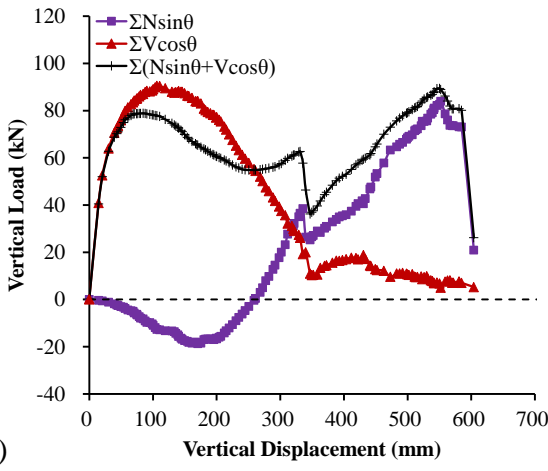


Fig. 27. Load transfer mechanisms at different beam sections of CL-8: (a) BENM; (b) BENS

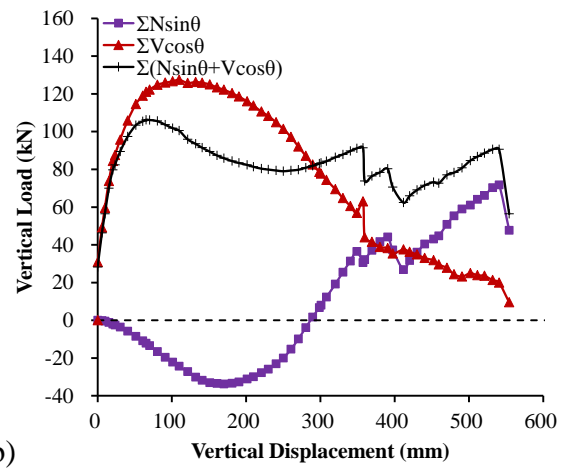
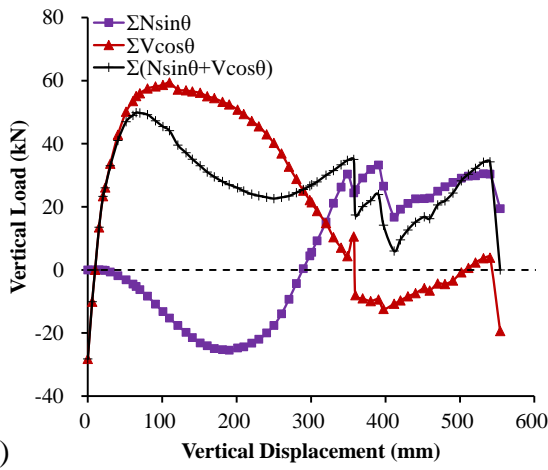


Fig. 28. Load transfer mechanisms at different beam sections of SL-8: (a) BENM; (b) BENS

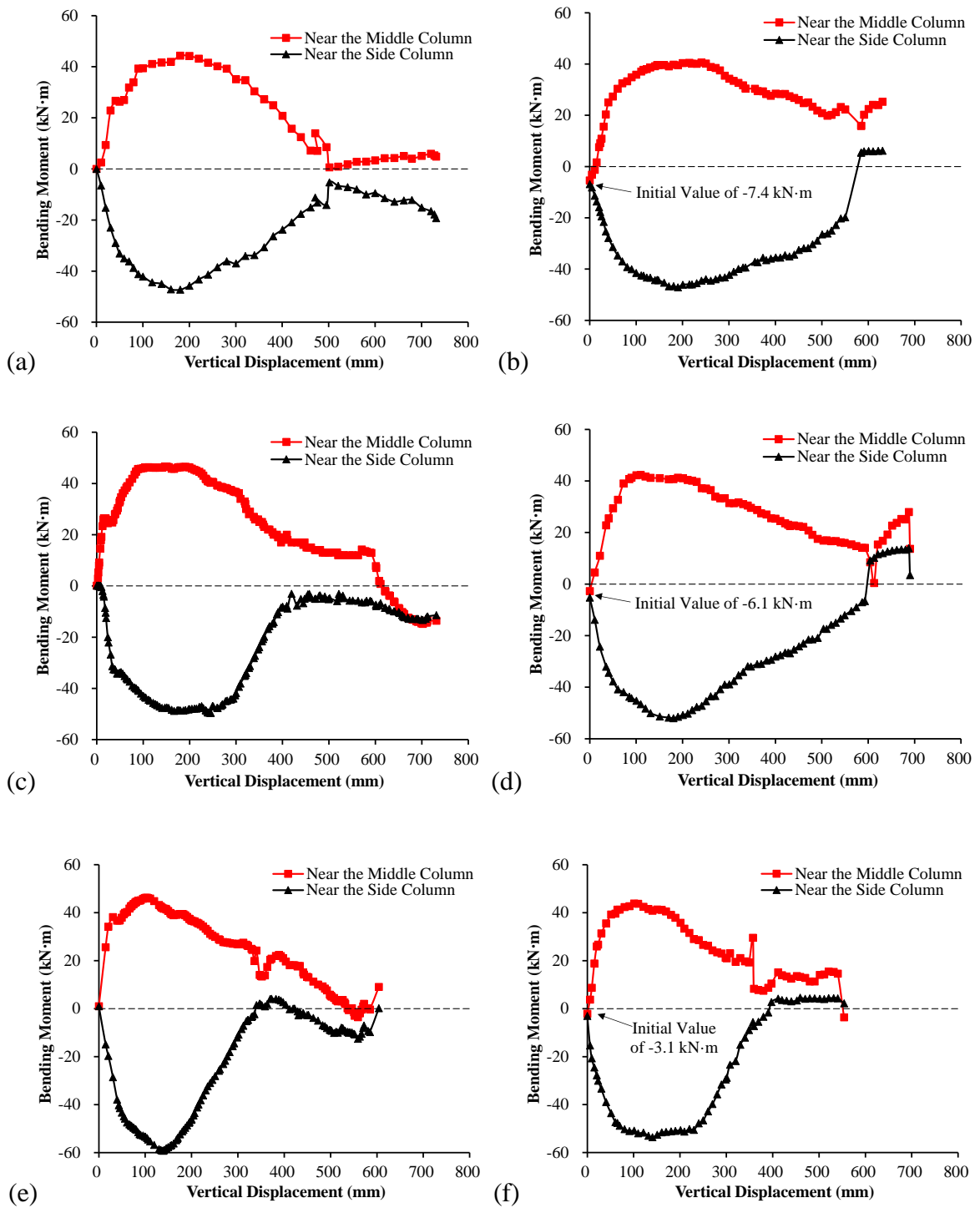


Fig. 29. Relationship of bending moment vs. deflection at different cross-sections: (a) CL-13; (b) SL-13; (c) CL-11; (d) SL-11; (e) CL-8; (f) SL-8

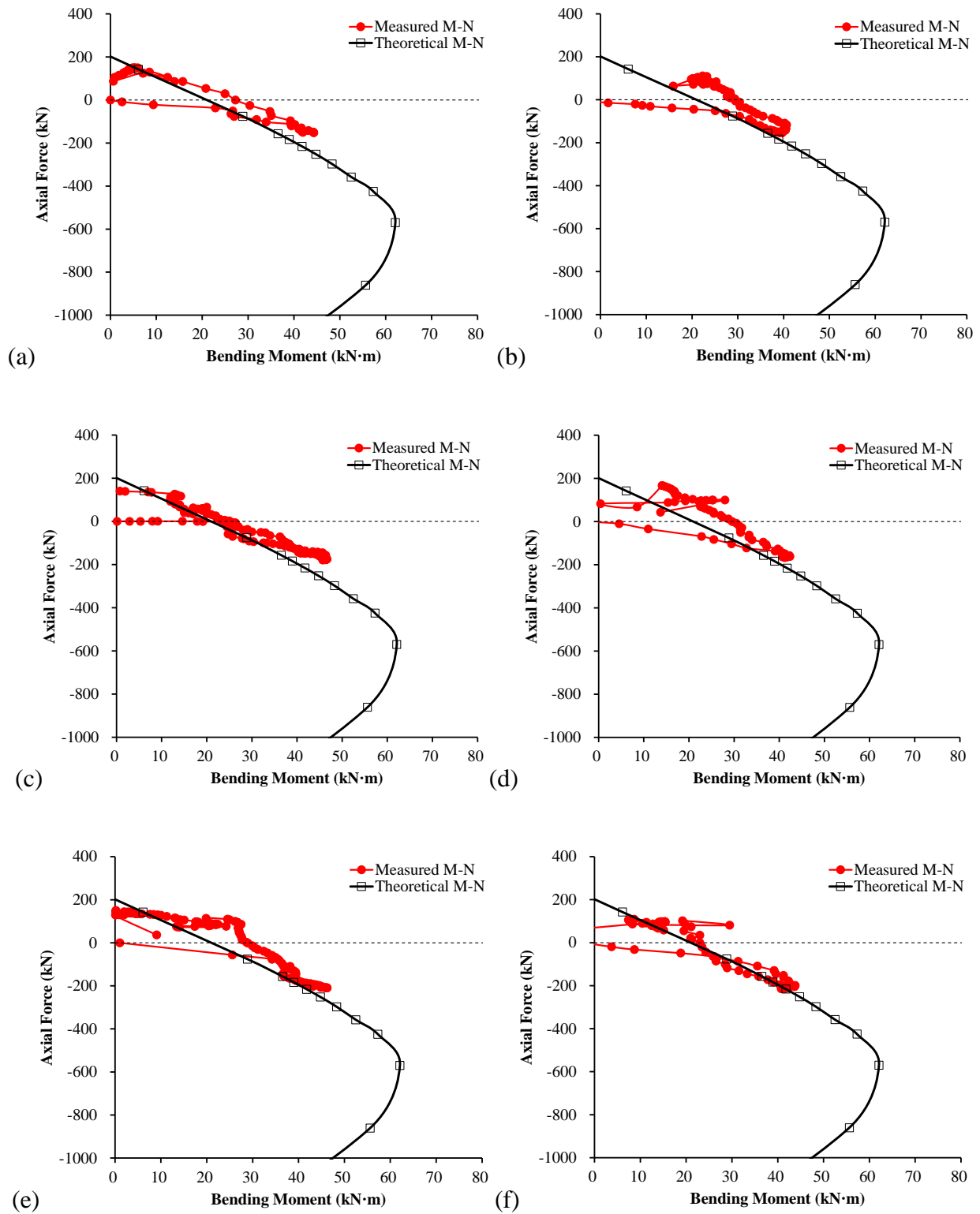


Fig. 30. *M-N* diagram at BENM: (a) CL-13; (b) SL-13; (c) CL-11; (d) SL-11; (e) CL-8; (f) SL-8

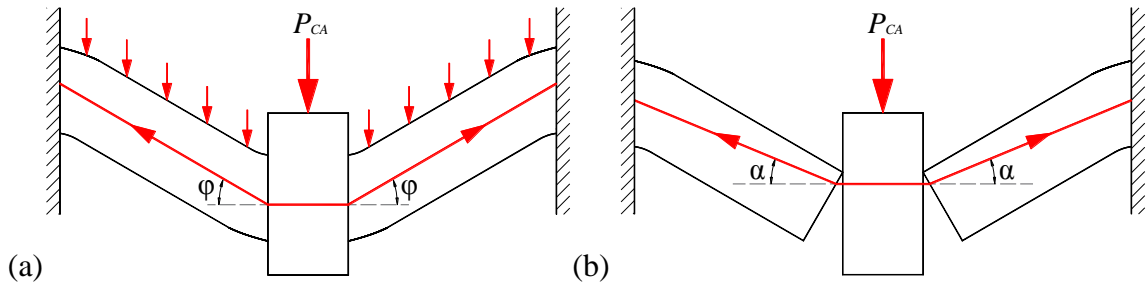


Fig. 31. Definition of the rotation of φ and α for SL-series and CL-series specimens: (a) φ for SL-

1
2
3
4
5
6
7
8
9
10
11
12
13
14
15
16
17
18
19
20
21
22
23
24
25
26
27
28
29
30
31
32
33
34
35
36
37
38
39
40
41
42
43
44
45
46
47
48
49
50
51
52
53
54
55
56
57
58
59
60
61
62
63
64
65